

# Pulsating hydrogen-deficient white dwarfs and pre-white dwarfs observed with *TESS*

## I. Asteroseismology of the GW Vir stars RX J2117+3412, HS 2324+3944, NGC 6905, NGC 1501, NGC 2371, and K 1–16

Alejandro H. Córscico<sup>1,2</sup>, Murat Uzundag<sup>3,4</sup>, S. O. Kepler<sup>5</sup>, Leandro G. Althaus<sup>1,2</sup>, Roberto Silvotti<sup>6</sup>, Andrzej S. Baran<sup>7,8,9</sup>, Maja Vučković<sup>3</sup>, Klaus Werner<sup>10</sup>, Keaton J. Bell<sup>11,12</sup>, and Michael Higgins<sup>13</sup>

<sup>1</sup> Grupo de Evolución Estelar y Pulsaciones. Facultad de Ciencias Astronómicas y Geofísicas, Universidad Nacional de La Plata, Paseo del Bosque s/n, 1900 La Plata, Argentina

<sup>2</sup> IALP - CONICET

<sup>3</sup> Instituto de Física y Astronomía, Universidad de Valparaíso, Gran Bretaña 1111, Playa Ancha, Valparaíso 2360102, Chile

<sup>4</sup> European Southern Observatory, Alonso de Cordova 3107, Santiago, Chile

<sup>5</sup> Instituto de Física, Universidade Federal do Rio Grande do Sul, 91501-970, Porto-Alegre, RS, Brazil

<sup>6</sup> INAF-Osservatorio Astrofisico di Torino, strada dell'Osservatorio 20, 10025 Pino Torinese, Italy

<sup>7</sup> Uniwersytet Pedagogiczny, Obserwatorium na Suhorze, ul. Podchorążych 2, 30-084 Kraków, Polska

<sup>8</sup> Embry-Riddle Aeronautical University, Department of Physical Science, Daytona Beach, FL 32114, USA

<sup>9</sup> Department of Physics, Astronomy, and Materials Science, Missouri State University, Springfield, MO 5897, USA

<sup>10</sup> Institute for Astronomy and Astrophysics, Kepler Center for Astro and Particle Physics, Eberhard Karls University, Sand 1,72076 Tübingen, Germany

<sup>11</sup> DIRAC Institute, Department of Astronomy, University of Washington, Seattle, WA-98195, USA

<sup>12</sup> NSF Astronomy and Astrophysics Postdoctoral Fellow

<sup>13</sup> Department of Physics, Duke University, Durham, NC-27708, USA

e-mail: acorsico@fcaglp.unlp.edu.ar

Received ; accepted

### ABSTRACT

**Context.** The recent arrival of continuous photometric observations of unprecedented quality from space missions has largely fueled the study of pulsating stars, bringing the area to an unprecedented interest in stellar astrophysics. In the particular case of pulsating white dwarfs, the *TESS* mission is taking asteroseismology of these compact stars to a higher level, emulating or even surpassing the performance of its predecessor, the *Kepler* mission.

**Aims.** In this paper, we present a detailed asteroseismological analysis of six GW Vir stars including the observations collected by the *TESS* mission.

**Methods.** We processed and analyzed *TESS* observations of RX J2117+3412 (TIC 117070953), HS 2324+3944 (TIC 352444061), NGC 6905 (TIC 402913811), NGC 1501 (TIC 084306468), NGC 2371 (TIC 446005482), and K 1–16 (TIC 233689607). We carried out a detailed asteroseismological analysis of these stars on the basis of PG 1159 evolutionary models that take into account the complete evolution of the progenitor stars. We constrained the stellar mass of these stars by comparing the observed period spacing with the average of the computed period spacings, and, when possible, we employed the individual observed periods to search for a representative seismological model.

**Results.** In total, we extracted 58 periodicities from the *TESS* light curves of these GW Vir stars using a standard pre-whitening procedure to derive the potential pulsation frequencies. All the oscillation frequencies that we found are associated with *g*-mode pulsations with periods spanning from  $\sim 817$  s to  $\sim 2682$  s. We find constant period spacings for all but one star (K 1–16), which allowed us to infer their stellar masses and constrain the harmonic degree  $\ell$  of the modes. Based on rotational frequency splittings, we derive the rotation period of RX J2117+3412, obtaining a value in agreement with previous determinations. We performed period-to-period fit analyses on five of the six analyzed stars. For four stars (RX J2117+3412, HS 2324+3944, NGC 1501, and NGC 2371), we were able to find an asteroseismological model with masses in agreement with the stellar-mass values inferred from the period spacings, and generally compatible with the spectroscopic masses. Obtaining seismological models allowed us to estimate the seismological distance and compare it with the precise astrometric distance measured with *GAIA*. Finally, we find that the period spectrum of K 1–16 exhibits dramatic changes in frequency and amplitude which, together with the scarcity of modes, prevented us from making a meaningful seismological modeling.

**Conclusions.** The high-quality data collected by the *TESS* space mission, considered simultaneously with ground-based observations, are able to provide a very valuable input to the asteroseismology of GW Vir stars, similar to the case of other classes of pulsating white-dwarf stars. The *TESS* mission, in conjunction with future space missions and upcoming surveys, will make impressive progress in white-dwarf asteroseismology.

**Key words.** asteroseismology — stars: oscillations (including pulsations) — stars: interiors — stars: evolution — stars: white dwarfs



## 1. Introduction

Pulsating white dwarfs (WD) and pre-WDs constitute a well established class of variable stars that exhibit pulsation periods in the range 100 – 7000 s, associated to low-order ( $\ell \leq 3$ ) nonradial  $g$  (gravity) modes. At present, there are about 350 known pulsating WDs, spread among several subclasses such as ZZ Ceti stars or DAVs (pulsating hydrogen-rich WDs), V777 Her stars or DBVs (pulsating helium-rich WDs), and GW Vir stars or pulsating PG 1159 stars, among others (see the reviews by Winget & Kepler 2008; Fontaine & Brassard 2008; Althaus et al. 2010; Córscico et al. 2019). White-dwarf asteroseismology has undergone substantial progress, thanks to ground-based observations, mainly with the time-series photometric observations of the “Whole Earth Telescope” (WET; Nather et al. 1990), followed by the spectral observations of the Sloan Digital Sky Survey (SDSS, York et al. 2000), and in recent years by the availability of space missions that provide unprecedented high-quality data. Indeed, the *Kepler* satellite, both the main mission (Borucki et al. 2010) and the *K2* mode (Howell et al. 2014), allowed the study of 32 ZZ Ceti stars and two V777 Her stars (Østensen et al. 2011; Hermes et al. 2017a,b; Bell et al. 2017; Bell 2017; Córscico 2020), until it was out of operation by October 2018. The successor of *Kepler* is the Transiting Exoplanet Survey Satellite (*TESS*, Ricker et al. 2015). *TESS* has provided extensive photometric observations of the 200 000 brightest stars in 85 % of the sky in the first part of the mission, each observation with a time base of about 27 days per sector observed.

GW Vir stars are pulsating PG 1159 stars —hot hydrogen (H)-deficient, carbon (C)-, oxygen (O)-, helium (He)-rich pre-WD stars— that include PNNV stars — still surrounded by a nebula — and DOV stars — that lack a nebula (Winget et al. 1991). The classification of GW Vir stars includes also the pulsating Wolf-Rayet central stars of planetary nebula ([WC]) and Early-[WC] = [WCE] stars, because they share the same pulsation properties of pulsating PG 1159 stars (Quirion et al. 2007). GW Vir stars exhibit multiperiodic luminosity variations with periods in the range 300–6000 sec, induced by nonradial gravity ( $g$ )-mode pulsations driven by the  $\kappa$ -mechanism due to partial ionization of C and O in the outer layers (Starrfield et al. 1983, 1984; Stanghellini et al. 1991; Gautschy et al. 2005; Córscico et al. 2006; Quirion et al. 2007). PG 1159 stars represent the evolutionary connection between post-AGB stars and most of the H-deficient WDs, including DO and DB WDs (Werner & Herwig 2006). These stars likely have their origin in a born-again episode induced by a post-AGB He thermal pulse (see Herwig 2001; Blöcker 2001; Althaus et al. 2005; Miller Bertolami et al. 2006, for references).

In this work, we determine the internal structure and evolutionary status of the pulsating pre-WD stars RX J2117.1+3412, HS 2324+3944, NGC 6905, NGC 1501, NGC 2371, and K 1–16 on the basis of the full PG 1159 evolutionary models of Althaus et al. (2005) and Miller Bertolami & Althaus (2006). These models were derived from the complete evolution of progenitor stars through the thermally pulsing AGB phase and born-again episode. We compute adiabatic  $g$ -mode pulsation periods on PG 1159 evolutionary models with stellar masses ranging from 0.530 to 0.741  $M_{\odot}$ .

The paper is organized as follows. In Sect. 2 we provide an account of the main characteristics of the studied GW Vir stars. Sect. 3 is focused on describing the methods we apply to obtain the pulsation periods of each target star. Sect. 4 is devoted to search for a constant period spacing in the list of periods of each

star by applying three significance tests. A brief summary of the stellar models of PG 1159 stars employed for the asteroseismological analysis of these stars is provided in Sect. 5. In Section 6 we derive the spectroscopic masses of the target stars on the basis of their published values of  $T_{\text{eff}}$  and  $\log g$ . In Sect. 7 we carry out a detailed asteroseismological analysis for each star, by assessing the stellar mass of each object through the use of the period spacing when possible, and by performing period-to-period fits with the aim of finding an asteroseismological model for each pulsating PG 1159 star. Finally, in Sect. 8, we summarize our main results and make some concluding remarks.

## 2. The targets

Unlike the *Kepler* space telescope, characterized by a restricted sky coverage, the *TESS* mission is providing unprecedented photometric observations of GW Vir stars, given its expansive sky coverage. In this work, we report on new *TESS* observations of the already known pulsating pre-WD stars RX J2117.1+3412, HS 2324+3944, NGC 6905, NGC 1501, NGC 2371, and K 1–16. Note that NGC 6905 and NGC 1501 are not formally spectroscopic PG 1159 stars, but instead [WCE] stars, and NGC 2371 is classified as a [WC]-PG 1159 transition object. The essential difference between the PG 1159, [WC] and [WCE] spectroscopic classes is the presence of much stronger winds and mass losses in the [WC] and [WCE] objects, leading to emission line spectra (Werner & Herwig 2006). Following Quirion et al. (2007), we include in this paper the stars NGC 6905, NGC 1501, and NGC 2371 in the category of GW Vir variable stars. The location of the six stars in the  $\log T_{\text{eff}}$  vs.  $\log g$  diagram is displayed in Fig. 1. Note that, according to the surface gravity of each star and the evolutionary tracks of Miller Bertolami & Althaus (2006), all the stars to be analyzed in this study are evolving at stages prior to their maximum possible temperatures, before entering the cooling branch of WDs. It is expected, then, that all these stars are heating and contracting, with the consequent secular shortening of the periods of pulsation of their  $g$  modes (see Sect. 7).

We describe the basic characteristics of these stars below:

- RX J2117.1+3412 (hereafter RX J2117 and TIC 117070953): a PNNV star characterized by an effective temperature of  $T_{\text{eff}} = 170\,000 \pm 10\,000$  K, a surface gravity of  $\log g = 6.00 \pm 0.3$ , and a surface composition of  $(X_{\text{He}}, X_{\text{C}}, X_{\text{O}}) = (0.39, 0.55, 0.06)$  (Werner & Herwig 2006). This is one of the PG 1159 stars in which iron has been detected (Werner et al. 2010). At this effective temperature, the star is the hottest known GW Vir star. The location of this star in the  $\log T_{\text{eff}} - \log g$  diagram is displayed in Fig. 1. The *Gaia* DR2 parallax and corresponding distance for this star are  $\pi = 1.991 \pm 0.050$  mas and  $d = 502 \pm 12$  pc. The variability of this star was independently discovered by Watson & Werner (1992) and Vauclair et al. (1993). Vauclair et al. (2002) analyzed the star in depth and published a large amount of results from a multisite photometric campaign with the WET (Nather et al. 1990). A search for  $p$  (pressure) modes in this star was carried out by Chang et al. (2013), with null results. RX J2117 has been the focus of a detailed asteroseismological modelling by Córscico et al. (2007a), yielding a variety of constraints; among them, a value of the asteroseismic stellar mass that is considerably lower than suggested by spectroscopy coupled to evolutionary tracks.

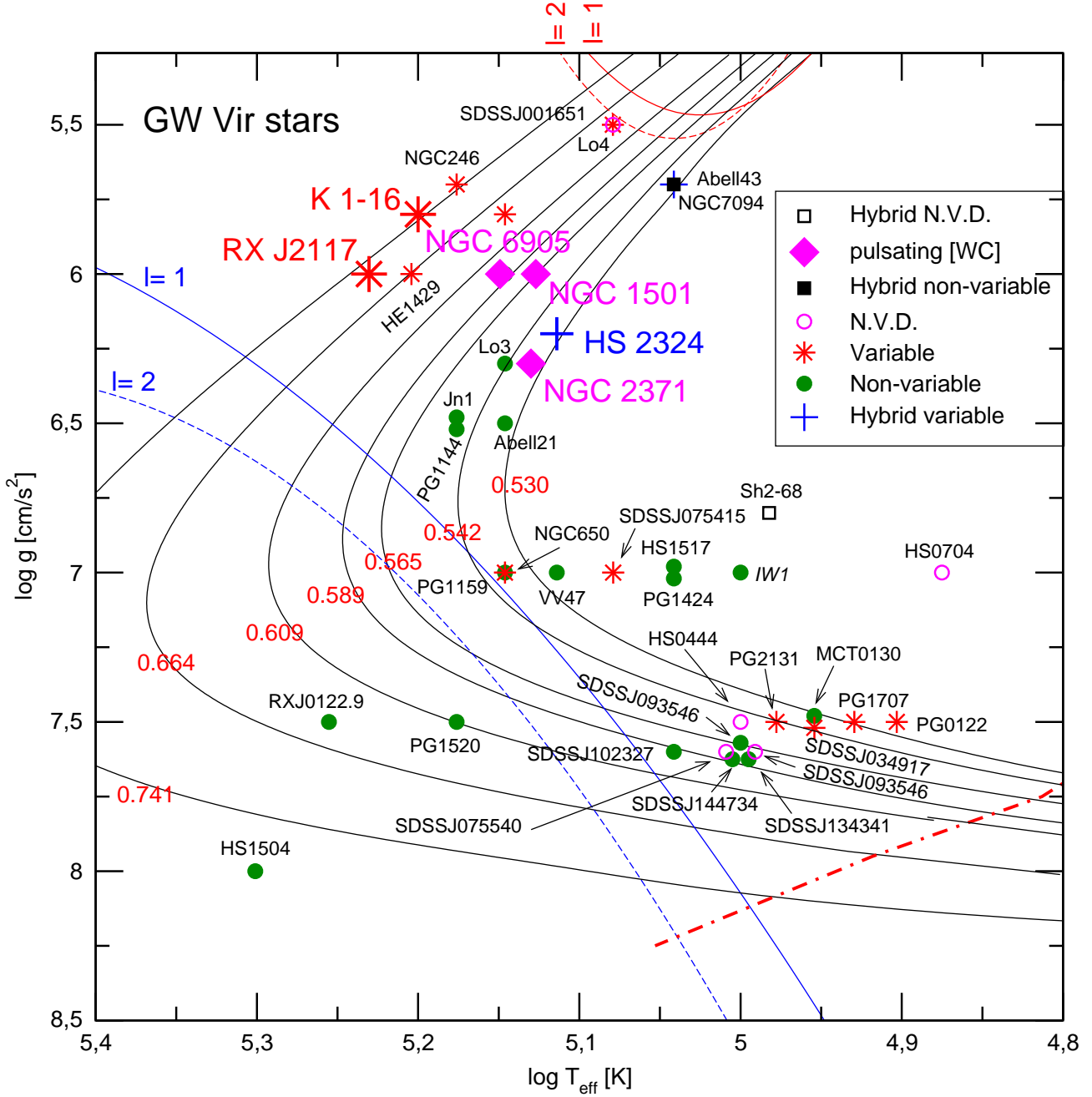


**Fig. 1.** Location of the spectroscopically calibrated variable and non-variable PG 1159 stars and variable [WCE] stars in the  $\log T_{\text{eff}} - \log g$  plane. PG 1159 stars with no variability data (N.V.D.) are depicted with hollow circles. Thin solid curves show the evolutionary tracks from Miller Bertolami & Althaus (2006) for stellar masses: 0.530, 0.542, 0.565, 0.589, 0.609, 0.664, and  $0.741 M_{\odot}$ . Parameterizations of the theoretical pulsational dipole (solid curves) and quadrupole (dashed curves) red and blue edges of the instability domain according to Córscico et al. (2006) are also displayed. The location of the GW Vir stars RX J2117 (red star), K 1–16 (red star), HS 2324 (blue plus), NGC 6905, NGC 1501, and NGC 2371 (magenta diamonds) are emphasized with large symbols.

– HS 2324+3944 (hereafter HS 2324 and TIC 352444061): one out of four peculiar members of the PG 1159 spectral class that exhibit H at the surface, called “hybrid PG 1159 stars” (Napiwotzki & Schoenberner 1991). The star exhibits a surface chemical composition of  $(X_{\text{H}}, X_{\text{He}}, X_{\text{C}}, X_{\text{O}}) = (0.17, 0.35, 0.42, 0.06)$  (Werner & Herwig 2006). This object is characterized by an effective temperature  $T_{\text{eff}} = 130\,000 \pm 10\,000$  K and a surface gravity  $\log g = 6.2 \pm 0.2$  (see Fig. 1). The *Gaia* DR2 parallax and corresponding distance for this star are  $\pi = 0.691 \pm 0.0502$  mas and  $d = 1448 \pm 105$  pc.

HS 2324 was discovered to be pulsating by Silvotti (1996) (see, also, Handler et al. 1997a), and it was the target of a multisite photometric campaign carried out by Silvotti et al. (1999). This object has not been the subject of a published asteroseismological modeling.

– NGC 6905 (also TIC 402913811): a [WCE]-type star discovered by Ciardullo & Bond (1996), characterized by  $T_{\text{eff}} = 141\,000$  K and  $\log g = 6$  (see Fig. 1), and pulsation periods in the range 710 – 912 s. Ciardullo & Bond (1996) found that, while the principal pulsation modes lie within a

**Table 1.** The list of six pulsating pre-white dwarf stars studied in this work. Columns 1, 2, 3, 4, 5, 6, 7 and 8 correspond to the *TESS* input catalog number, name of the object, effective temperature, surface gravity, GW Vir class, spectral classification, parallax, and distance, respectively. For details, see the text.

TIC	Name	$T_{\text{eff}}$ [K]	$\log g$ [cgs]	GW Vir class	Spectral type	$\pi$ [mas]	$d$ [pc]
117070953	RX J2117.1+3412	$170\,000 \pm 10\,000$	$6.00 \pm 0.03$	PNNV	PG 1159	$1.991 \pm 0.050$	$502 \pm 12$
352444061	HS 2324+3944	$130\,000 \pm 10\,000$	$6.20 \pm 0.20$	DOV	PG 1159 (hybrid)	$0.691 \pm 0.050$	$1448 \pm 105$
402913811	NGC 6905	$141\,000 \pm 10\,000$	$6.00 \pm 0.20$	PNNV	[WCE]	$0.612 \pm 0.059$	$1634 \pm 158$
084306468	NGC 1501/[WO4]	$134\,000 \pm 10\,000$	$6.00 \pm 0.20$	PNNV	[WCE]	$0.567 \pm 0.025$	$1763 \pm 79$
446005482	NGC 2371	$135\,000 \pm 10\,000$	$6.30 \pm 0.20$	PNNV	[WC]-PG 1159	$0.532 \pm 0.066$	$1879 \pm 232$
233689607	K 1–16	$160\,000 \pm 16\,000$	$5.80 \pm 0.30$	PNNV	PG 1159	$0.466 \pm 0.053$	$2146 \pm 244$

fairly restricted range of frequencies, the individual modes that are actually observed change completely on a timescale of a few months (or less). The surface chemical composition of NGC 6905 is  $(X_{\text{He}}, X_{\text{C}}, X_{\text{O}}) = (0.60, 0.25, 0.15)$  (Koesterke 2001). The *Gaia* DR2 parallax and corresponding distance for this object are  $\pi = 0.612 \pm 0.059$  mas and  $d = 1634 \pm 158$  pc. This star has not been asteroseismologically modelled before.

- NGC 1501 (also TIC 084306468): classified as a [WCE]-type star. The effective temperature and gravity of this star are  $T_{\text{eff}} = 134\,000$  K and  $\log g = 6.0$  (Fig. 1), and its surface chemical composition is  $(X_{\text{He}}, X_{\text{C}}, X_{\text{O}}) = (0.50, 0.35, 0.15)$  (Koesterke & Hamann 1997; Werner & Herwig 2006). The parallax and corresponding distance for this star extracted from *Gaia* DR2 are  $\pi = 0.567 \pm 0.025$  mas and  $d = 1763 \pm 79$  pc. The variability of NGC 1501 was detected by Ciardullo & Bond (1996), who measured ten periodicities ranging from 5200 s down to 1154 s, with the largest-amplitude pulsations occurring between 1154 s and 2000 s. As for NGC 6905, in the case of NGC 1501 the observed pulsation spectrum varies on timescales of months Ciardullo & Bond (1996). Based on period-spacing data, Bond et al. (1996) inferred a stellar mass of  $0.53 \pm 0.03 M_{\odot}$  for NGC 1501. The star was a target of a detailed asteroseismological analysis by Córscico et al. (2009a), who derived a stellar mass of  $\sim 0.57 M_{\odot}$  based on the period-spacing data. However, they were unable to find an unambiguous best-fit model with a period-fit procedure.
- NGC 2371 (also TIC 446005482): a GW Vir variable classified as a [WC]-PG 1159 transition object. It was discovered to be pulsating by Ciardullo & Bond (1996). The star shows periodicities in the range 923 – 1825 s, and has atmospheric parameters  $T_{\text{eff}} = 135\,000$  K and  $\log g = 6.3$  (see Fig. 1), and  $(X_{\text{He}}, X_{\text{C}}, X_{\text{O}}) = (0.54, 0.37, 0.08)$  (Herald & Bianchi 2004). Like NGC 6905 and NGC 1501, NGC 2371 exhibits variations of the characteristics of the frequency spectrum on timescales of months or shorter (Ciardullo & Bond 1996). From *Gaia* DR2, we know that the parallax and distance of this object are  $\pi = 0.532 \pm 0.066$  mas and  $d = 1879 \pm 232$  pc, respectively. This star has not been the focus of any detailed asteroseismological analysis.
- K 1–16 (also Kohoutek 1–16 and TIC 233689607): a PNNV star characterized by an effective temperature of  $T_{\text{eff}} = 140\,000 \pm 10\,000$  K, a surface gravity of  $\log g = 6.40 \pm 0.3$ , and a surface composition of  $(X_{\text{He}}, X_{\text{C}}, X_{\text{O}}) = (0.33, 0.50, 0.17)$  (Werner & Herwig 2006). Werner et al. (2007) and Werner et al. (2010) discovered

high-ionization lines of neon (Ne VIII) and iron (Fe X) in K 1–16, and re-determined its effective temperature and gravity as  $T_{\text{eff}} = 160\,000 \pm 16\,000$  K and  $\log g = 5.8 \pm 0.3$  (see Fig. 1). Also, the chemical composition was re-determined:  $(X_{\text{He}}, X_{\text{C}}, X_{\text{O}}) = (0.58, 0.34, 0.06)$  (Werner et al. 2010). K 1–16 was the first PNNV star to be discovered (Grauer & Bond 1984). These authors detected periodicities with a dominant period of  $\sim 1700$  s and a semi-amplitude of about 0.01 mag. Grauer & Bond (1984) found that several additional periods sometimes appear in power spectra derived from light curves, and on two occasions a rapid drop into —or emergence from— a state in which no detectable variations were present. Feibelman et al. (1995) claimed spectral variability and speculated about a connection of this phenomenon to the changes in the pulsating nature of this star. From *Gaia* DR2, the parallax and distance of K 1–16 are  $\pi = 0.466 \pm 0.053$  mas and  $d = 2146 \pm 244$  pc, respectively. The asteroseismological potential of this interesting object has not been thoroughly studied yet.

We summarize the stellar properties of the six target stars in Table 1.

### 3. Observations and data reduction

The primary mission of *TESS* is to search for exoplanets around bright target stars. It was launched successfully on 18 April 2018 (Ricker et al. 2014). The mission-data products of *TESS* also allow us to study stellar variability, including pulsations. Thanks to nearly continuous, stable photometry, as well as its expansive sky coverage, *TESS* has made a significant contribution to the study of stellar pulsations in evolved compact objects (Bell et al. 2019; Wang et al. 2020; Althaus et al. 2020; Bognár et al. 2020).

In this work, we study six known pulsating pre-white dwarf stars by investigating their pulsational characteristics with the high-precision photometry of *TESS* (see Table 2). The transformations between the photometric systems, from the visual magnitude ( $V_{\text{mag}}$ ) to *TESS*  $T_{\text{mag}}$  magnitudes, are calculated using publicly available code of `ticgen`<sup>1</sup>. The stars were observed in 2-min short-cadence mode of *TESS*, corresponding to a Nyquist frequency of 4200  $\mu\text{Hz}$ . We downloaded the light curves from The Mikulski Archive for Space Telescopes, which is hosted by the Space Telescope Science Institute (STScI)<sup>2</sup> as FITS format. The data contained in the FITS files are processed based on the Pre-Search Data Conditioning Pipeline (Jenkins et al. 2016). We extracted times and fluxes (PDCSAP FLUX) from the FITS

<sup>1</sup> <https://github.com/tessgi/ticgen>

<sup>2</sup> <http://archive.stsci.edu/>

**Table 2.** The list of six GW Vir stars reported from *TESS* observations, including the name of the targets, *TESS* magnitude, observed sectors, date, *CROWDSAP* keyword, and length of the runs (columns 1, 2, 3, 4, 5 and 6, respectively). From the Fourier Transform of the original and shuffled data, three different set of parameters: resolution, average noise level of amplitude spectra, and detection threshold which we define as the amplitude at 0.1% false alarm probability, FAP, are presented in columns 7, 8 and 9, respectively. The *CROWDSAP* keyword shows the ratio of the target flux to the total flux in the optimal *TESS* light curve aperture.

Name	$T_{\text{mag}}$	Obs. Sector	Start Time (BJD-2 457 000)	CROWDSAP	Length [d]	Resolution $\mu\text{Hz}$	Average Noise Level [ppt]	0.1% FAP [ppt]
RX J2117.1+3412	11.73	15	1711.3688	0.519	22.76	0.76	0.26	1.18
HS 2324+3944	14.81	16-17	1738.6566	0.571	49.14	0.35	0.44	2.07
NGC 6905	13.90	14	1683.3582	0.087	26.85	0.43	0.73	3.35
NGC 1501/[WO4]	12.40	19	1816.0888	0.556	25.06	0.46	0.11	0.53
NGC 2371	12.90	20	1842.5093	0.356	26.31	0.44	0.20	0.90
K 1-16	14.36	14-17 19-20 22-26	1683.3542	0.570	298.93	0.038	0.21	0.86

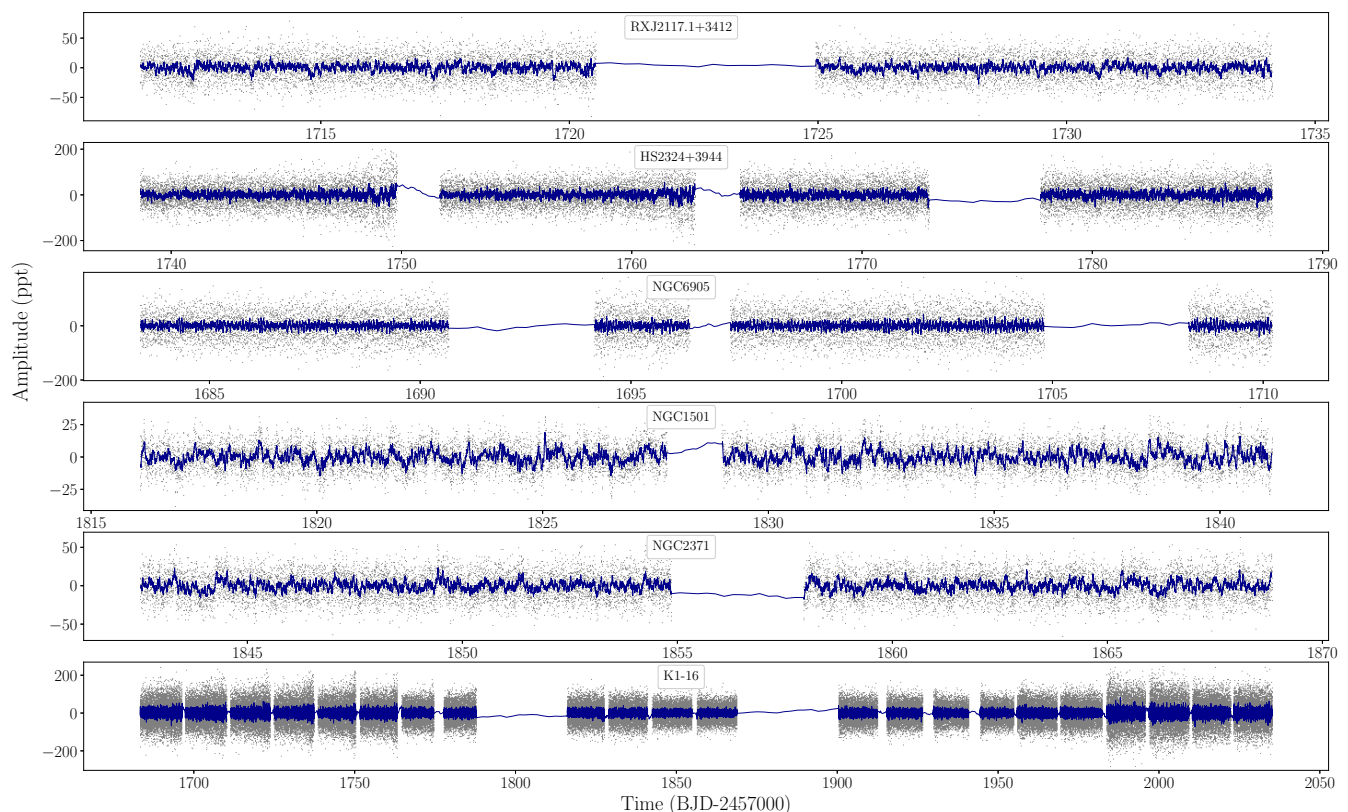


**Fig. 2.** Reduced *TESS* light curves of the pulsating pre white-dwarf stars studied in this work. The black dots are the *TESS* data sampled every two minutes. The blue lines are binned light curves which are calculated by running mean every 20 points (corresponding to 38 minutes). K 1-16 was observed during nine sectors (14, 15, 16, 17, 19, 20, 22, 23, 24, 25 and 26), HS 2324 was observed during two consecutive sectors (16 and 17), and the other stars were observed during a single sector each.

files. The times are given in barycentric corrected dynamical Julian days (BJD - 2457000, corrected for leap seconds, see Eastman et al. 2010). The fluxes are converted to fractional variations from the mean, i.e. differential intensity  $\Delta I/I$ , and transformed to amplitudes in parts-per-thousand (ppt). The ppt unit corresponds to the milli-modulation amplitude (mma) unit<sup>3</sup> used in the past. We sigma-clipped the data at  $5\sigma$  to remove the out-

<sup>3</sup> 1 mma =  $1/1.086$  mmag = 0.1 % = 1 ppt; see, e.g., Bognar & Sodor (2016).

liers which appear above 5 times the median of intensities — i.e. departed from the (local) mean by  $5\sigma$ .

The final light curves of the target stars are shown in Fig. 2. After detrending the light curves, we calculated their Fourier transforms (FTs) and examined them for pulsations and binary signatures. For pre-whitening, we employed our customized tool in which, using a nonlinear least square (NLLS) method, we simultaneously fitted each pulsation frequency in a waveform  $A_i \sin(\omega_i t + \phi_i)$ , with  $\omega = 2\pi/P$ , and  $P$  the period. This iterative process has been done starting with the highest peak, until there is no peak that appears above 0.1% FAP significance threshold.

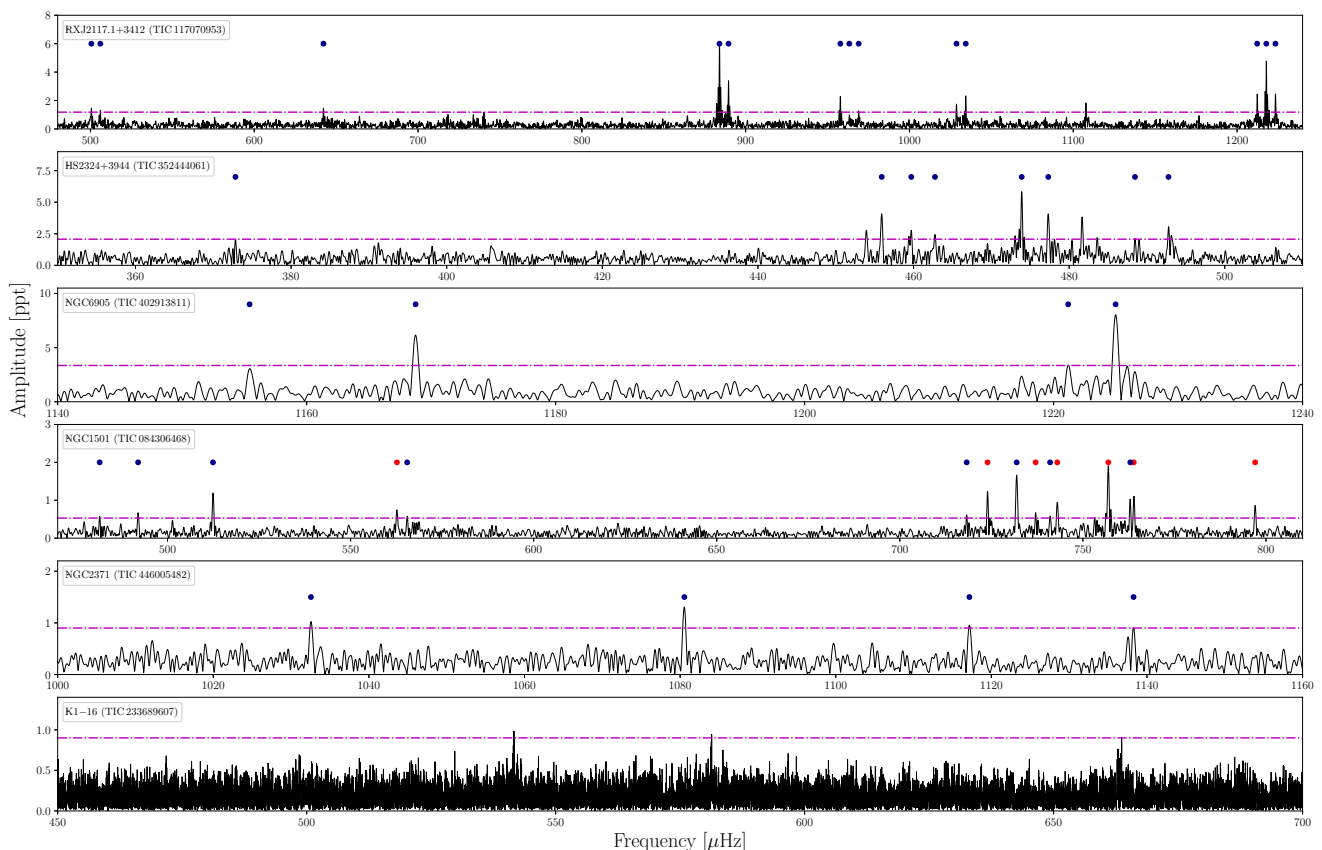


**Fig. 3.** The FTs of the GW Vir stars studied in this work, showing identified dipole ( $\ell = 1$ , blue dots) and quadrupole ( $\ell = 2$ , red dots) modes. The horizontal magenta dashed line shows the detection threshold, which is defined as 0.1% FAP.

We analyzed the concatenated light curve from different sectors, if observed. The false alarm probability was calculated randomizing the timings, i.e., shuffling the observations one thousand times and recalculating the FTs. We calculated the amplitude at which there is a 0.1% = 1/1000 probability of any peak being due to noise (e.g., Kepler 1993).

Before describing the observations of each individual target star, we would like to emphasize that most pulsating WDs and pre-WDs, including GW Vir stars, show amplitude and frequency variations. A similar phenomenon is observed in pulsating sdB stars. An example of this phenomenon is documented in this paper for K 1–16 (see Sect. 3.6 below). In general terms, some modulations could be probably due to simple photon-count noise caused by contamination of the background light in the aperture. Other modulations could come from the rotation-to-pulsation energy interchange, as the amplitude of the components of the multiplets changing with time have been detected over the years. In the case of GW Vir stars, however, considering that the theoretical  $e$ -folding times are much longer than the observations, we do not expect real mode energy interchanges, as we do observe for the DBV star GD 358, for example (Provencal et al. 2009).

### 3.1. RX J2117

RX J2117 (TIC 117070953,  $T_{\text{mag}} = 11.73$ ,  $m_V = 12.33$ ) was observed by *TESS* on Sector 15 between 2019 Aug 15 and 2019 Sep 11. The temporal resolution is  $1.5/T = 0.76 \mu\text{Hz}$  ( $T$  is data span of 22.8 days). The average noise level of the amplitude spectra

is of 0.29 ppt. The upper panel of Fig. 2 depicts the light curve, and the upper panel of Fig. 3 shows the FT corresponding to RX J2117. In Table 3 we show the list of periods of RX J2117 detected with *TESS*. The period at 1038 s corresponds to a peak with S/N lower than 4. However, we have included it because it corresponds to the central component of a triplet and has been observed in ground-based data (Vauclair et al. 2002).

The frequencies emphasized with boldface in Table 3 can be interpreted as components of rotational triplets ( $\ell = 1$ ), with an average frequency separation of  $\delta\nu \sim 5.57 \mu\text{Hz}$ . This frequency separation is in agreement with the value found by Vauclair et al. (2002). The rotational multiplets are depicted in Fig. 4. Let us briefly describe the effect of rotation on the pulsation frequencies of a star. In the presence of stellar rotation, non-radial modes of degree  $\ell$  split into  $2\ell + 1$  components differing in azimuthal ( $m$ ) number. In the case of slow and solid rotation, the frequency splitting can be obtained as:  $\delta\nu_{\ell,k,m} = m(1 - C_{\ell,k})\Omega_R$ ,  $\Omega_R$  being the angular rotational frequency of the pulsating star, and  $m = 0, \pm 1, \pm 2, \dots, \pm\ell$ . The condition of slow rotation translates in  $\Omega_R \ll \nu_{\ell,k}$ . The coefficients  $C_{\ell,k}$ , called Ledoux coefficients (Ledoux & Walraven 1958), adopt a simple form in the asymptotic limit of high radial-order  $g$  modes ( $k \gg \ell$ ):  $C_{\ell,k} \sim [\ell(\ell + 1)]^{-1}$ . For dipole ( $\ell = 1$ ) and quadrupole ( $\ell = 2$ ) modes, we have  $C_{1,k} \sim 0.5$  and  $C_{2,k} \sim 0.17$ , respectively. The presence of multiplets in the frequency spectrum of a pulsating WD can be very useful to identify the harmonic degree of the pulsations. This method to infer the rotation period has been successfully applied to several pulsating WD stars (see Hermes et al. 2017a, for the case of ZZ Ceti stars observed during the *Kepler* and

**Table 3.** Independent frequencies, periods, and amplitudes, their uncertainties, and the signal-to-noise ratio in the data of RX J2117. Frequencies in boldface correspond to components of rotational triplets (see Fig. 4). Errors are given in parenthesis to 2 significant digits.

Peak	$\nu$ ( $\mu\text{Hz}$ )	$\Pi$ (s)	$A$ (ppt)	S/N
$f_1$	<b>500.559(39)</b>	1997.760(16)	1.45(23)	5.5
$f_2$	<b>506.057(43)</b>	1976.060(17)	1.33(23)	5.1
$f_3$	642.255(40)	1557.010(10)	1.44(23)	5.5
$f_4$	740.266(49)	1350.870(9)	1.17(23)	4.5
$f_5$	<b>884.017(9)</b>	1131.200(12)	6.15(23)	23.6
$f_6$	<b>889.556(17)</b>	1124.156(21)	3.37(23)	12.9
$f_7$	<b>957.817(25)</b>	1044.041(27)	2.30(23)	8.8
$f_8$	<b>963.28(6)</b>	1038.120(6)	1.03(23)	3.9
$f_9$	<b>969.013(44)</b>	1031.978(47)	1.29(23)	4.9
$f_{10}$	<b>1028.729(33)</b>	972.073(31)	1.72(23)	6.6
$f_{11}$	<b>1034.356(25)</b>	966.785(23)	2.31(23)	8.8
$f_{12}$	1107.713(31)	902.761(25)	1.84(23)	7.0
$f_{13}$	<b>1212.297(23)</b>	824.880(16)	2.48(23)	9.5
$f_{14}$	<b>1217.872(12)</b>	821.105(8)	4.78(23)	18.3
$f_{15}$	<b>1223.429(24)</b>	817.375(16)	2.41(23)	9.2

$K2$  missions). In the case of RX J2117, since the multiplets exhibited by the star are triplets (two complete triplets and three triplets with one undetected component each), this means that  $\ell = 1$ , and so,  $C_{\ell,k} \sim 0.5$ . We assume that the central peak of the

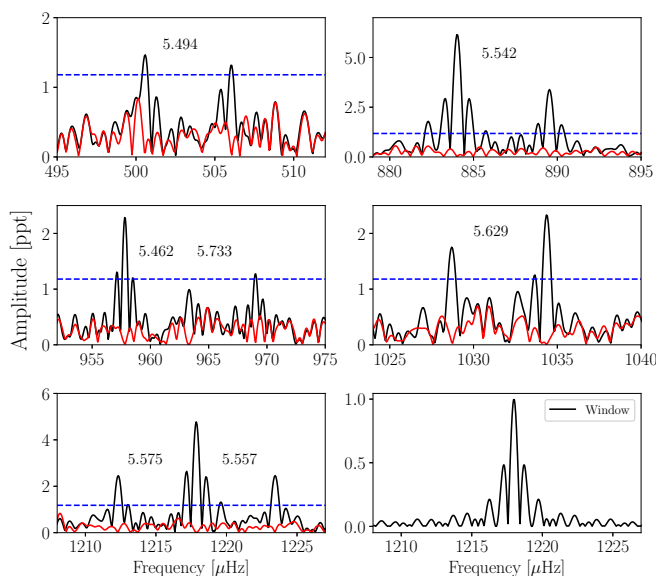


**Fig. 4.** The amplitude spectra of RX J2117 showing rotational multiplets. The subfigures present rotational splittings in different region in the amplitude spectra with an average of splitting  $\delta\nu = 5.570 \mu\text{Hz}$ . The last subfigure (bottom right) presents the window function of RX J2117 for the frequency  $1217.872 \mu\text{Hz}$ . The horizontal blue dashed line shows the confidence level of 0.1% FAP. The red lines are residuals after extraction of the signals.

multiplets ( $m = 0$  components) are  $1997.75$ ,  $1124.15$ ,  $1038.12$ ,  $972.07$  and  $889.557 \mu\text{Hz}$ . Therefore, we can obtain an estimate of the rotational period of RX J2117 of  $P_{\text{rot}} = 1/\Omega_{\text{R}} \sim 1.04$  days.

An interesting feature of the FT of RX J2117 is a series of at least seven low-frequency harmonics of a  $9.509 \pm 0.004 \mu\text{Hz}$  signal. These are suggestive of variability from a photometric binary with an orbital period of  $1.2172 \pm 0.0005$  days. Extracting and analyzing light curves from every individual pixel in the TESS target pixel file for TIC 117070953 reveals a clear binary eclipse signature. This is strongest outside the aperture used by the TESS pipeline to extract the light curve for RX J2117, but near enough to contribute some light to the aperture. We conclude that the eclipses do not originate from the PNNV target. A public software tool to aid the identification of contaminating variable stars in the large  $21''$  TESS pixels is under development (Higgins & Bell, in prep.).

### 3.2. HS 2324

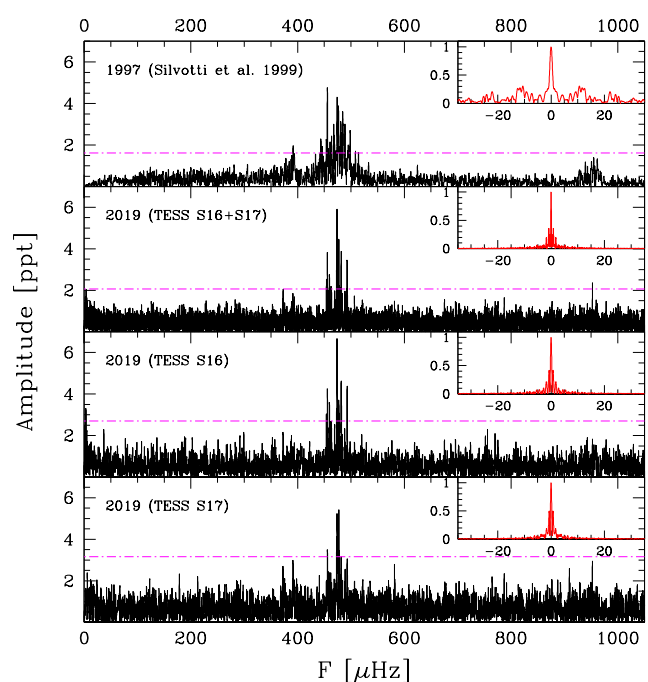


**Fig. 5.** Comparison between the amplitude spectrum of HS 2324 in 1997 (Silvotti et al. 1999) and 2019 (*TESS* data). The detection threshold (magenta dash-dotted line) in 2019 is slightly higher (2.07 ppt with sector 16 and 17 together vs 1.62 ppt in 1997), but the spectral window (red, upper-right panels) is much cleaner. This partially explains the higher density of peaks in 1997. The low level of noise below  $\sim 100 \mu\text{Hz}$  in 1997 is due to artificial filtering.

HS 2324 (TIC 352444061,  $T_{\text{mag}} = 14.81$ ,  $m_V = 15.41$ ), was observed for 49.15 days on Sectors 16 and 17 with a duty cycle of 91.02%. The light curve is shown in Figure 2. In Fig. 3 we show the FT. In Table 4 we list the periods above 0.1% FAP level of 2.07 ppt (corresponding to a S/N of 3.23) detected in the *TESS* light curve. While 11 frequencies are populating a small region of the power spectrum between  $\sim 450 \mu\text{Hz}$  and  $\sim 500 \mu\text{Hz}$ , one frequency is located in the low frequency region ( $\sim 372.8 \mu\text{Hz}$ ) and a peak is found in the high frequency region ( $\sim 952.5 \mu\text{Hz}$ ). The signal with  $952.5 \mu\text{Hz}$  is close to twice the main frequency group and thus we can not exclude that it is a linear combination of the main peaks. However, it does not



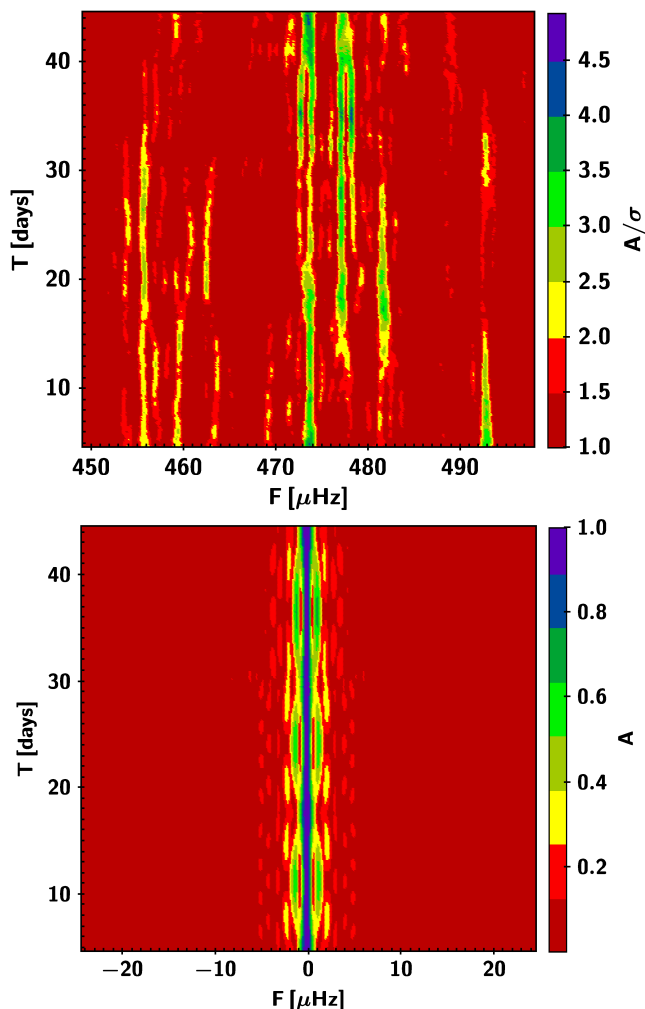


**Fig. 6.** Top: sliding Fourier Transform (sFT) of HS 2324 in the region between 449 and 498  $\mu\text{Hz}$ . The color-coded amplitude is given in  $\sigma$  units, i.e. amplitude divided by the mean noise of each FT. Since each FT is computed on a short subrun of 9.3 days, the FT mean noise is high and this is why the color-coded S/N appears much lower than in Table 4. Bottom: sliding Window Function (sWF) obtained using a single sinusoid of constant frequency and constant amplitude of one, without any noise. The frequency scale is the same in both panels. See text for more details on sFT/sWF computations.

correspond exactly to any combination, the closest combination being at 951.2 ( $= 473.9 + 477.3$ )  $\mu\text{Hz}$ . A direct comparison between the amplitude spectrum in 1997 (Silvotti et al. 1999) and the *TESS* amplitude spectrum of 2019 is shown in Fig. 5.

Silvotti et al. (1999), with a frequency resolution of 1.4  $\mu\text{Hz}$ , suggested a possible rotation period of  $\sim 2.3$  days for HS 2324. They also proposed that the detected peaks were part of dipole and quadrupole asymptotic sequences, elaborating on period spacings of 18.8 s and 10.4 s for  $\ell = 1$  and  $\ell = 2$ , respectively. Here, we find that all the periodicities detected in *TESS* data can be associated to dipole sequences (see Fig. 3 and Sect. 4.2). With a frequency resolution of 0.35  $\mu\text{Hz}$ , we find no clear indications of rotational multiplets, suggesting that the star may have a rotation period longer than  $\sim 49$  days (the duration of the run) and/or that the star is seen pole-on, or also that the modes with  $m = \pm 1$  are not excited during the observations (see, e.g., Baran et al. 2015; Winget et al. 1991).

Notwithstanding the above, we have also examined the possibility that the two pairs of frequencies at (481.67 –

**Table 4.** Independent frequencies, periods, and amplitudes (and their uncertainties) and the signal-to-noise ratio in the data of HS 2324.

Peak	$\nu$ ( $\mu\text{Hz}$ )	$\Pi$ (s)	A (ppt)	S/N
$f_1$	372.849(23)	2682.05(17)	2.04(38)	4.6
$f_2$	453.928(19)	2202.99(9)	2.52(38)	5.7
$f_3$	455.909(12)	2193.42(6)	4.00(38)	9.0
$f_4$	459.709(16)	2175.29(8)	2.96(38)	6.7
$f_5$	462.755(19)	2160.97(9)	2.50(38)	5.6
$f_6$	473.900(8)	2110.152(35)	6.01(38)	13.6
$f_7$	477.316(11)	2095.046(49)	4.26(38)	9.6
$f_8$	481.670(13)	2076.11(5)	3.73(38)	8.4
$f_9$	488.458(22)*	2047.26(9)	2.10(38)	4.7
$f_{10}$	492.769(16)	2029.35(7)	3.12(39)	7.0
$f_{11}$	493.215(22)	2027.52(9)	2.32(39)	5.2
$f_{12}$	952.492(22)	1049.877(24)	2.16(38)	4.9

\* Alternatively, it could be 488.984  $\mu\text{Hz}$ . The two close peaks have similar amplitude and when one of the two is selected, the other one gets down below the detection threshold.

**Table 5.** Independent frequencies, periods, and amplitudes (and their uncertainties) and the signal-to-noise ratio in the data of NGC 6905.

Peak	$\nu$ ( $\mu\text{Hz}$ )	$\Pi$ (s)	A (ppt)	S/N
$f_1$	1155.415(43)	865.490(32)	3.1(6)	4.2
$f_2$	1168.752(22)	855.613(16)	6.1(6)	8.4
$f_3$	1221.170(38)	818.887(26)	3.5(6)	4.8
$f_4$	1224.984(17)	816.337(11)	8.0(6)	11.1

477.316)  $\mu\text{Hz}$  and (492.769 – 488.458)  $\mu\text{Hz}$  are two ( $\ell = 1$ ) incomplete rotational triplets with frequency separations of 4.354  $\mu\text{Hz}$  and 4.310  $\mu\text{Hz}$ , respectively. As a matter of fact, a rotational splitting of  $\sim 4.3$   $\mu\text{Hz}$  can not be totally excluded, and it is very close to the  $\sim 4.2$   $\mu\text{Hz}$  splitting found by Silvotti et al. (1999). If these two pairs of frequencies were actually part of two rotational triplets, then only one component of each pair should be used in the assessment of the dipole period spacing in Sect. 4.2. As we shall see in that Section, the assessment of the period-spacing of HS 2324 remains almost unaltered even if we remove two frequencies from the analysis.

In Fig. 6 we show the sliding FT (sFT) of HS 2324 in the main region of the spectrum (top panel), that can be compared with the sliding Window Function (sWF, bottom panel). We see that most frequencies are relatively stable, with some variations in amplitude. This figure clearly exclude the damping oscillator hypothesis that was considered by Silvotti et al. (1999). Some additional details on sFT/sWF computations are given at the end of Section 3.6. For HS 2324 each data subset includes 6715 data points (corresponding to  $\sim 9.3$  days for continuous data) and the step between one subset and the next corresponds to 51 data points (0.07 days for continuous data).

To continue a photometric monitoring of this star would be useful in order to detect new pulsation frequencies, verify the presence of rotational multiplets, and confirm the identification of some  $\ell = 2$  pulsation modes (see Sect. 7.2 and Table 16).

### 3.3. NGC 6905

NGC 6905 (TIC 402913811,  $T_{\text{mag}} = 13.90$ ,  $G = 14.5545 \pm 0.0027$ ), was observed for 26.85 days on Sector 14. *TESS* observations of NGC 6905 started on 18 July 2019 and lasted on 15 August 2019. These observations yield 13 615 data points after we removed the outliers. The final light curve after detrending is shown in Figure 2. NGC 6905 is a good illustration of cross contamination in *TESS* photometry. Each *TESS* pixel comprises 21 arcsec. NGC 6905's planetary nebula extends to 32 arcsec, and there is an additional target (*Gaia* magnitude of 14.5) a mere 10 arcsec from NGC 6905. This contamination reflects itself as additional noise in the FT of NGC 6905. Indeed, NGC 6905 has the highest average noise level (0.73 ppt) of our sample. All the oscillation amplitudes that are extracted from the light curve are reduced due to this contamination from the nearby stars and nebula. The FT of NGC 6905 showed a few signals within S/N of 4.6. We calculated the threshold at 0.1% false alarm probability as 3.35 ppt corresponding to S/N of 4.6. The average noise level for NGC6905 is 0.73 ppt. The peaks that are extracted from the light curve appear at 4.14, 8.14, 4.67 and 10.68  $\sigma$  ( $\sigma$  is the median of noise level of amplitude). We included the peak of 1155.415  $\mu\text{Hz}$  as a possible oscillation. Additionally, we extracted three more periodicities from the light curve. These three frequencies, 1168.752, 1221.170 and 1224.984  $\mu\text{Hz}$ , are robust detections with S/N of 8.4, 4.8 and 11.1, respectively. After the extraction of these three peaks from the light curve, we calculated the average noise level of amplitude spectra and defined the new detection threshold. The average noise level of the FT excluding these three modes is remained almost the same as 0.73 ppt (the difference is negligible with 0.001 ppt). The 0.1% FAP was also not affected drastically and found as 3.34 ppt (including all the peaks 0.1% FAP = 3.35). If we consider the detection threshold 4  $\sigma$  of 3 ppt, then 1155.415  $\mu\text{Hz}$  ( $f_1$ ) can conveniently be evaluated as true pulsational peak. These four extracted peaks are shown in Fig. 3 and listed in Table 5.

### 3.4. NGC 1501

NGC 1501 (TIC 084306468,  $T_{\text{mag}} = 12.40$ ,  $m_V = 13.0$ ) was observed on sector 19, which spanned about 25 days from 27 November 2019 to 24 December 2019. We have performed the FT from the light curve shown in Fig. 2, consisting of 16893 measurements with a duty cycle of 92.8%. The frequency spectra shows a rich content of peaks with 16 pulsational signals above the detection limit of 0.1% FAP= 0.53 ppt. In Table 6 we show the list of periods of NGC 1501. The period spectrum detected with *TESS* is markedly different from that found by Bond et al. (1996). Indeed, the 11 periods derived by Bond et al. (1996) are more evenly distributed over a wider range of periods. A graphic comparison between the ground- and space-based period spectra of NGC 1501 is made in Sect. 4.4.

In Fig. 3 we display the FT of NGC 1501 from *TESS*. The pulsation power concentrates on a frequency (period) interval from 481  $\mu\text{Hz}$  (2077 s) to 797  $\mu\text{Hz}$  (1254.6 s). The highest-amplitude ( $A = 1.938$  ppt) peak is located at a frequency of 756.954  $\mu\text{Hz}$  in the high-frequency region of the spectrum. The other bunch of peaks are in the high-frequency region between 718  $\mu\text{Hz}$  and 797  $\mu\text{Hz}$ . Concerning the peak at  $\sim 68$   $\mu\text{Hz}$ , this is probably due to contamination, since it is not the result of a difference of other frequencies. Also, the corresponding period at  $\sim 14800$  s is too long for GW Vir stars, so that it cannot represent an eigenmode of the star. Since this mode is not included

**Table 6.** Independent frequencies, periods and amplitudes (and their uncertainties) and the signal-to-noise ratio in the data of NGC 1501.

Peak	$\nu$ ( $\mu\text{Hz}$ )	$\Pi$ (s)	A (ppt)	S/N
$f_1$	67.617(13)	14789.2(2.9)	1.77(9)	15.4
$f_2$	481.465(43)	2077.00(19)	0.55(9)	4.7
$f_3$	491.971(34)	2032.64(14)	0.69(9)	6.0
$f_4$	512.428(20)	1951.49(8)	1.18(9)	10.2
$f_5$	562.655(31)	1777.29(10)	0.77(9)	6.7
$f_6$	565.448(39)	1768.51(12)	0.60(9)	5.2
$f_7$	718.266(35)	1392.24(7)	0.67(9)	5.8
$f_8$	723.958(19)	1381.295(36)	1.23(9)	10.7
$f_9$	731.915(14)	1366.279(27)	1.65(9)	14.3
$f_{10}$	737.094(34)	1356.68(6)	0.69(9)	6.0
$f_{11}$	741.039(42)	1349.46(8)	0.57(9)	4.9
$f_{12}$	743.012(25)	1345.872(44)	0.96(9)	8.3
$f_{13}$	756.948(13)	1321.095(23)	1.93(9)	16.8
$f_{14}$	762.954(23)	1310.696(40)	1.07(10)	9.3
$f_{15}$	763.892(22)	1309.086(37)	1.14(10)	9.9
$f_{16}$	797.047(27)	1254.632(43)	0.87(9)	7.5

**Table 7.** Independent frequencies, periods, and amplitudes (and their uncertainties) and the signal-to-noise ratio in the data of NGC 2371.

Peak	$\nu$ ( $\mu\text{Hz}$ )	$\Pi$ (s)	A (ppt)	S/N
$f_1$	105.657(25)	9464.6(2.2)	1.60(17)	8.0
$f_2$	1032.553(38)	968.474(36)	1.03(17)	5.1
$f_3$	1080.538(30)	925.465(26)	1.31(17)	6.5
$f_4$	1117.180(42)	895.111(34)	0.93(17)	4.6
$f_5$	1138.274(43)	878.523(33)	0.91(17)	4.5

in the seismic analysis of this study, we have not considered it further in the paper.

### 3.5. NGC 2371

NGC 2371 (TIC 446005482,  $T_{\text{mag}} = 12.90$ ,  $m_V = 13.5$ ) was observed in sector 20 of *TESS* (Table 2, Fig. 2). We extracted 4 frequencies above the detection threshold of 0.9 ppt, corresponding to a 0.1 % FAP (Table 7). The periodicities that we extracted from the light curve populate a small region of the power spectrum with periods (frequencies) between 878.524 s (1138.272  $\mu\text{Hz}$ ) and 1032.558 s (968.467  $\mu\text{Hz}$ ). In Fig. 3 we show the FT of NGC 2371. The peak at  $\sim 106$   $\mu\text{Hz}$  is probably due to contamination. This mode is not included in the seismic analysis and it is not considered further in the paper.

Given the frequency resolution of 0.44  $\mu\text{Hz}$  and the average noise level of 0.22 ppt, we did not detect any rotational multiplets in the frequency spectra. However, there is a hint regarding a possible constant period-spacing pattern (see Sect. 3).

### 3.6. K 1–16

K 1–16 (TIC 233689607,  $T_{\text{mag}} = 14.36$ ,  $m_V = 14.96$ ) was observed on sectors 14 – 17, 19 – 20, and 22 – 26 of *TESS*, between 18 July 2019 and 4 July 2020. The light curve of K 1–16 is presented in Fig. 2. If we look at individual sectors, the pulsations come and go, which means that the amplitudes and frequencies change significantly. When combining all data

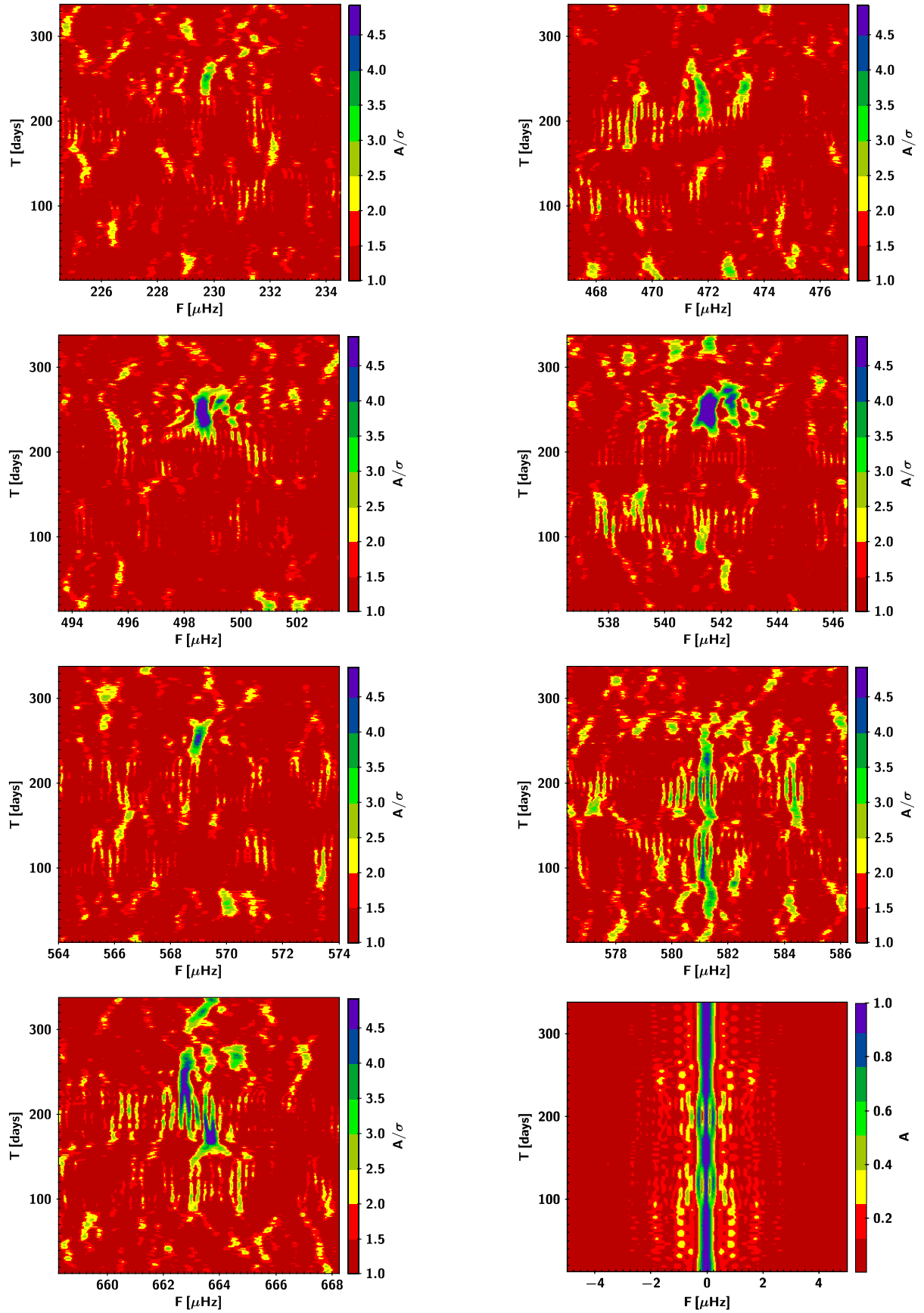


**Fig. 7.** Panels 1-7: sliding Fourier Transform (sFT) of K 1–16 centered on the peaks at  $\sim 229.7$ ,  $\sim 471.7$ ,  $\sim 498.7$ ,  $\sim 541.6$ ,  $\sim 569.0$ ,  $\sim 581.3$  and  $\sim 663.0$   $\mu\text{Hz}$ . The color-coded amplitudes are given in  $\sigma$  units, i.e. amplitude divided by the mean noise of each FT. The oscillations are not stable over the course of the *TESS* observations and in the first  $\approx 200$  days (up to sector 22) some of the modes are absent. Panel 8: sliding Window Function (SWF) obtained using a single sinusoid of constant frequency and constant amplitude of one, without any noise. The frequency scale is the same in all panels. See text for more details on sFT/sWF computations.

**Table 8.** Independent frequencies, periods, and amplitudes and the signal-to-noise ratio in the data of K 1–16.

Peak	$\nu$ ( $\mu\text{Hz}$ )	$\Pi$ (s)	$A$ (ppt)	S/N	$A_{max}$ (ppt)	S/N
( $f_1$ )	229.75	4352.6	1.70 <sup>1</sup>	4.2	2.43 <sup>3</sup>	4.2)
$f_2$	471.74	2119.8	1.78 <sup>1</sup>	4.4	2.30 <sup>4</sup>	4.0
$f_3$	498.73	2005.1	0.69 <sup>2</sup>	3.3	4.09 <sup>3</sup>	7.1
$f_4$	541.63 <sup>6</sup>	1846.3	1.08 <sup>2</sup>	5.1	5.50 <sup>3</sup>	9.5
$f_5$	568.97	1757.6	2.00 <sup>1</sup>	4.9	2.93 <sup>3</sup>	5.1
$f_4$	581.33 <sup>6</sup>	1720.2	0.90 <sup>2</sup>	4.3	3.00 <sup>5</sup>	4.6
$f_6$	663.04 <sup>7</sup>	1508.2	0.80 <sup>2</sup>	3.8	3.27 <sup>3</sup>	5.7

<sup>1</sup> Frequency and amplitude from sectors 22+23.

<sup>2</sup> Frequency and amplitude from all sectors.

<sup>3</sup> Maximum amplitude in sector 23.

<sup>4</sup> Maximum amplitude in sector 22.

<sup>5</sup> Maximum amplitude in sector 17.

<sup>6</sup> Could be aliases of super-Nyquist counterparts at 7791.7 and 7752.0  $\mu\text{Hz}$  respectively (cf. text).

<sup>7</sup> A close peak at 663.67  $\mu\text{Hz}$  could be either an independent frequency or the product of frequency variations (cf. Fig. 7).

together, we obtain a threshold of 0.93 ppt, which implies that only two peaks should be considered real. However, given that amplitudes (and frequencies) vary significantly on timescales of weeks/months like in other PG 1159 stars, a few more peaks have amplitudes well above the threshold in single sectors. Adding also these peaks, we obtain a list of five frequencies at S/N higher than 4.5 (Table 8). Two more frequencies at 229.75 and 471.74  $\mu\text{Hz}$  are included in Table 8 as they reach a S/N of 4.4 and 4.5 respectively, when we consider only a section of the light curve in which they reach the maximum amplitude, from BJD 2458904.35 to 2458954.87 and from 2458900.38 to 2458940.35, respectively (or days 221–271.5 and 217–257 in Fig. 7). Moreover, we investigated the possibility that some of the frequencies in Table 8 may be aliases of super-Nyquist peaks. The possibility of detecting super-Nyquist pulsation frequencies is well described by Murphy (2015), who showed that introducing a time-offset between one sector and the next may greatly help. Even though (unfortunately) this suggestion was not applied to the *TESS* observing strategy, however it happens that by chance a small offset of  $\sim 24$  seconds, i.e. 20% of the 2-min sampling time, exists between sector 17 and 19. In another two cases, between sector 19–20 and 20–22, time is off by  $\sim 4\%$  of the sampling time. This allows us to compare the amplitude of each peak with its super-Nyquist counterpart. Without offsets, e.g. using only sectors 22+23 in which the star shows the highest number of significant peaks, these amplitudes are almost identical. But when we add the sectors with the time offsets, the amplitudes differ and we see a larger amplitude for the peak at 7752.0  $\mu\text{Hz}$  (or 129.0 s) respect to its sub-Nyquist counterpart at 581.3  $\mu\text{Hz}$ . We see a similar behavior also for the peak at 541.6  $\mu\text{Hz}$  and its super-Nyquist counterpart at 7791.7  $\mu\text{Hz}$  (or 128.3 s), although in this case the effect is less pronounced. Therefore we can not totally exclude that the peak at 581.3  $\mu\text{Hz}$  is actually the alias of a super-Nyquist counterpart at 7752.0  $\mu\text{Hz}$  (and to less extent the same might be true for the sub/super-Nyquist pair at 541.63/7791.7  $\mu\text{Hz}$ ). However, we decided to favor the sub-Nyquist solution based on findings of Grauer & Bond (1984). Despite their poor frequency resolution that could not really resolve the region between  $\approx 530$  and  $\approx 620$   $\mu\text{Hz}$  (cf. their Fig.2b), the main peak they found was

at  $\sim 590$   $\mu\text{Hz}$ , quite close to the 581.3  $\mu\text{Hz}$  frequency detected by *TESS*. Moreover, their 50 s binned integration (and sampling) time, with original integrations of 5 s, should have allowed them to detect periods near 130 s. And finally we note that the peak at 7752.0  $\mu\text{Hz}$ , if true, would have a much larger amplitude due to smearing (see e.g. Bell et al. 2017), an order of magnitude larger than the amplitude detected in the *TESS* light curve of 1.35 ppt (and up to 2.54 ppt in sector 22).

Since the profiles of the peaks associated to unstable modes in the amplitude spectrum may be complex and a pre-whitening process gives only rough results, we do not report frequency and amplitude uncertainties in Table 8. Frequencies and amplitudes are those obtained from the complete data set or from individual sectors if the peak is detected only in some sectors. Moreover, we report in Table 8 also the maximum amplitude registered in a single sector. The long photometric measurements of K 1–16 allow us to construct sFTs to examine the temporal evolution of the pulsation modes over the course of the *TESS* observations and highlight the dramatic changes in frequency and amplitude of this star. First we divide the *TESS* light curve into 500 subsets of 17943 data each (corresponding to  $\sim 24.9$  days for continuous data) and step them by 324 data (0.45 d for continuous data). Afterward, we calculate the FT of each subset and stack them on top of each other. The sFTs of the seven detected frequencies are shown in Fig. 7 and can be compared with the sliding Window Function (sWF) in the last panel of Fig. 7. The color-coded amplitudes of the sFTs are given in  $\sigma$  units, i.e. amplitude divided by the mean noise of each FT. In most cases the frequencies are totally absent (no pulsation) in the first *TESS* observation sectors, and acquire measurable amplitudes only in sectors 22 and 23. This is particularly evident for the peaks near 498.7, 541.6 and 569.0  $\mu\text{Hz}$ .

#### 4. Period spacing

The  $g$  modes responsible for the brightness variations of WDs and pre-WDs can be excited in a sequence of consecutive radial orders,  $k$ , for each value of  $\ell$ . In the asymptotic limit ( $k \gg \ell$ ),  $g$  modes of consecutive radial overtone are approximately uniformly spaced in period (Tassoul et al. 1990). The period spacing is given by

$$\Delta\Pi_\ell^a = \frac{\Pi_0}{\sqrt{\ell(\ell+1)}}, \quad (1)$$

where  $\Delta\Pi_\ell^a$  is the asymptotic period spacing, and  $\Pi_0$  is a constant defined as:

$$\Pi_0 = \frac{2\pi^2}{\left[ \int_{r_1}^{r_2} \frac{N}{r} dr \right]}, \quad (2)$$

where  $N$  is the Brunt-Väisälä frequency.

While for chemically homogeneous stellar models the asymptotic formula (1) constitutes a very precise description of their pulsational properties, the  $g$ -mode period spacings in chemically stratified PG 1159 stars show appreciable departures from uniformity caused by the mechanical resonance called "mode trapping". The presence of one or more narrow regions in which the abundances of nuclear species vary rapidly strongly modifies the character of the resonant cavity in which modes should propagate as standing waves. Specifically, chemical interfaces act like reflecting walls that partially trap certain modes, forcing them to oscillate with larger amplitudes in specific regions

— bounded either by two interfaces or by one interface and the stellar center or surface — and with smaller amplitudes outside of those regions. The requirement for a mode to be trapped is that the wavelength of its radial eigenfunction matches the spatial separation between two interfaces or between one interface and the stellar center or surface. Mode trapping has been the subject of intense study in the context of stratified DA and DB WD pulsations (see, e.g., Brassard et al. 1992; Bradley et al. 1993; Córscico et al. 2002). In the case of PG 1159 stars, mode trapping has been extensively explored by Kawaler & Bradley (1994) and Córscico & Althaus (2006); we refer the reader to those works for details.

#### 4.1. Period spectrum of RX J2117

When we compare the pulsation spectrum of RX J2117 detected by *TESS* and that observed through the ground-based monitoring by Vauclair et al. (2002), we realize that the pulsation spectra are quite different. To begin with, the number of pulsation periods detected by *TESS* and reported here (15 periods; see Table 3) is substantially smaller than the number of periods measured by Vauclair et al. (2002), who identified 37 ones (see their Table 9). But the differences are not limited only to the number of periods detected, which can be mainly attributed to the small size of the *TESS* telescope, but also the *distribution* of the periods is completely different. In order to envisage this, in Fig. 8 we have schematically plotted the periods detected with *TESS* (upper panel), and the periods detected by Vauclair et al. (2002) (lower panel), with arbitrary amplitudes set to one to facilitate visualization. Clearly, the periods of the star detected by *TESS* are distributed over a much wider range of periods, compared to the periods measured by Vauclair et al. (2002). Only six periods, around 821, 825, 903, 1038, 1044 and 1124 s are almost identical between both sets of data. The reason for the discrepancy between ground-based and space observations is that the *TESS* mission can only detect large-amplitude modes, both because of its small telescope (15 cm diameter), and because it only observes redder than 6000 Å, where the pulsation amplitudes are small. The WET ground-based telescopes on which the data of Vauclair et al. (2002) are based are much larger.

In order to extract as much information as possible with the tools of asteroseismology, it is crucial to exploit all the pulsation data available — which should represent eigenvalues for the star. Therefore, to identify the pulsation modes and determine the period spacing of RX J2117, which is essential to estimate the stellar mass (see Sect. 7.1), we decided to expand the list of periods by adding the 20 dipole  $m = 0$  periods found by Vauclair et al. (2002) to the list of periods collected by *TESS* (Table 3). Note that only half of these 20  $m = 0$  periods were directly detected, the others were deduced through a detailed analysis from the presence of the  $m = -1$  and/or  $m = +1$  components of each  $\ell = 1$  triplet. For the periods close to 821 s, 972 s, 1038 s, and 1124 s, detected (or inferred) in both data sets, we adopted the periods measured by *TESS* because they are in general more accurate, due to the continuous long dataset. The extended list of periods to be used in our analysis contains 31 periods and is shown in Table 9.

We searched for a constant period spacing in the data of RX J2117 using the Kolmogorov-Smirnov (K-S; Kawaler 1988), the inverse variance (I-V; O’Donoghue 1994) and the Fourier Transform (F-T; Handler et al. 1997b) significance tests. In the K-S test, the quantity  $Q$  is defined as the probability that the observed periods are randomly distributed. Thus, any uniform or

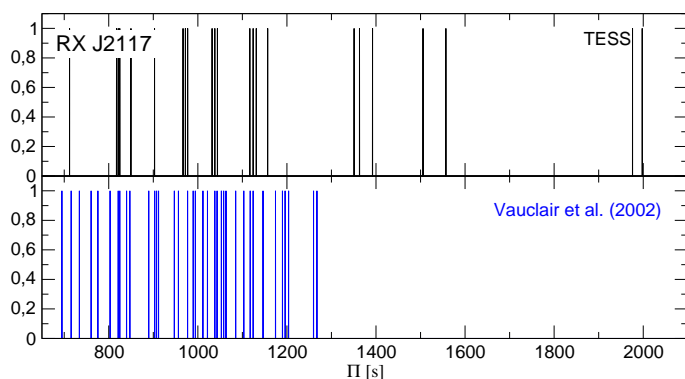
**Table 9.** Enlarged list of periods of RX J2117. Column 1 corresponds to 20  $\ell = 1$   $m = 0$  periods measured by Vauclair et al. (2002) (VEA02), and column 2 corresponds to the 15 periods detected by *TESS* (Table 3). The periods with an asterisk are the ones used in the linear least square fit (Fig. 10).

$\Pi_i^O$ (s) VEA02	$\Pi_i^O$ (s) <i>TESS</i>	$\Pi_{\text{fit}}$ (s)	$\delta\Pi$ (s)	$\ell^O$
692.267*		691.298	0.969	1
712.975*		712.967	0.008	1
733.948*		734.636	-0.688	1
757.354*		756.305	1.049	1
778.921*		777.974	0.947	1
799.495*		799.643	-0.148	1
	817.375			1
821.145	821.105*	821.312	-0.207	1
	824.880			1
843.692*		842.981	0.711	1
885.736*		886.319	-0.583	1
	902.761			?
907.489*		907.988	-0.499	1
951.750*		951.326	0.424	1
	966.785			1
972.247	972.073*	972.995	-0.922	1
994.387*		994.664	-0.277	1
1016.467*		1016.333	0.134	1
	1031.978			1
1038.118	1038.120*	1038.002	0.118	1
	1044.041			1
1058.026*		1059.671	-1.645	1
1103.292*		1103.009	0.283	1
1124.117	1124.156*	1124.678	-0.522	1
	1131.200			1
1146.346*		1146.347	-0.001	1
1189.956*		1189.685	0.271	1
	1350.870			?
	1557.010	1558.058	-1.048	1
	1976.060			?
	1997.760			?

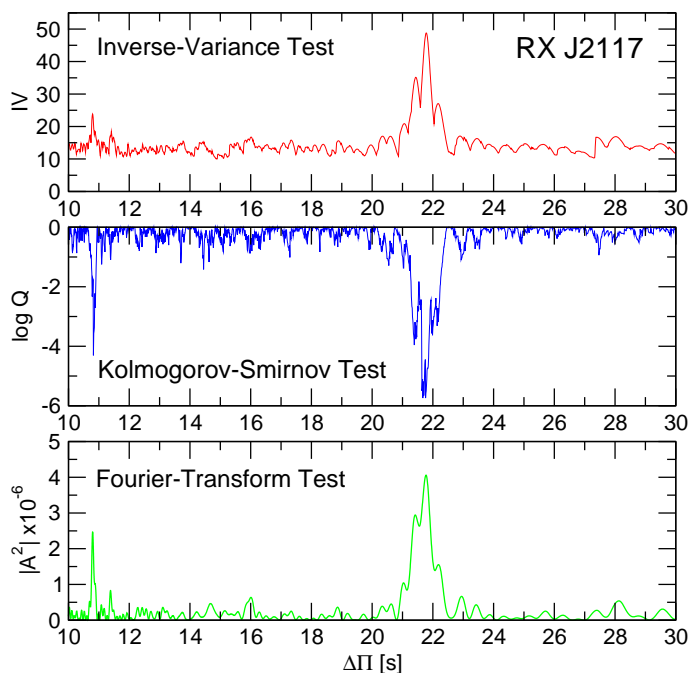
at least systematically non-random period spacing in the period spectrum of the star will appear as a minimum in  $Q$ . In the I-V test, a maximum of the inverse variance will indicate a constant period spacing. Finally, in the F-T test, we calculate the FT of a Dirac comb function (created from a set of observed periods), and then we plot the square of the amplitude of the resulting function in terms of the inverse of the frequency. A maximum in the square of the amplitude will indicate a constant period spacing.

Fig. 9 displays the results of applying the K-S, I-V, and F-T significance tests to the set of 31 periods of Table 9. The three tests point to the existence of a pattern of  $\ell = 1$  constant period spacing of  $\Delta\Pi \sim 22$  s<sup>4</sup>. To derive a refined value of the period spacing, we have carried out a linear least-squares fit to the 20 periods marked with an asterisk in Table 9, excluding those with  $m \neq 0$  and those for which mode identification is uncertain. We obtain a period spacing of  $\Delta\Pi = 21.669 \pm 0.030$  s (see upper panel of Fig. 10). This value is very close to the period spacing derived by Vauclair et al. (2002) on the basis of ground-based observations alone ( $\Delta\Pi = 21.618 \pm 0.008$  s). With the derived

<sup>4</sup> Note also the presence of a peak at  $\sim 11$  s, that is simply the sub-harmonic of this  $\ell = 1$  period spacing ( $\Delta\Pi/2$ ).



**Fig. 8.** Schematic distribution of the pulsation periods of RX J2117 according to *TESS* (15 periods, black lines, upper panel), and according to Vauclair et al. (2002) (37 periods, blue lines, lower panel). The amplitudes have been arbitrarily set to one for clarity.



**Fig. 9.** I-V (upper panel), K-S (middle panel), and F-T (bottom panel) significance tests to search for a constant period spacing in RX J2117. The tests are applied to the set of 31 pulsation periods of Table 9. A clear signal of a constant period spacing at  $\sim 21.8$  s is evident. See text for details.

value of the mean period spacing we determine one more period compatible with the  $\ell = 1$  string, at about 1557 s. The remaining periods can be associated with  $\ell = 1$  modes (which, due to mode trapping effects, deviate from the derived sequence of almost equally-spaced periods) or with modes with  $\ell = 2$  (or possibly higher). The relevance of finding a constant period spacing is twofold: on the one hand it allows the identification of the harmonic degree of the modes (that is, the assignment of the harmonic degree  $\ell$ ; see Table 9), and on the other hand, it enables us to estimate the stellar mass. This will be addressed for RX J2117 in Sect. 7.1.

In the lower panel of Fig. 10 we show the residuals ( $\delta\Pi$ ) between the observed periods ( $\Pi_i^O$ ) and the periods derived from the mean period spacing ( $\Pi_{fit}$ ). The presence of several minima in the distribution of residuals strongly suggests the mode-

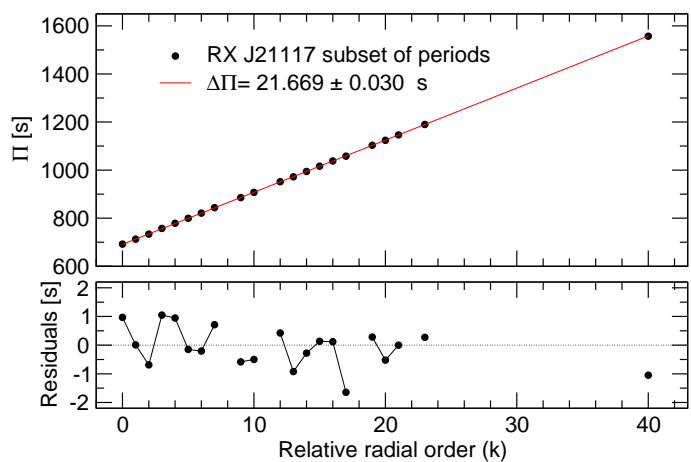


**Fig. 10.** Upper panel: linear least-squares fit to the 20 periods of RX J2117 marked with asterisks in Table 9. The derived period spacing from this fit is  $\Delta\Pi = 21.669 \pm 0.030$  s. Lower panel: the residuals of the period distribution relative to the mean period spacing, revealing signals of mode trapping in the period spectrum of RX J2117. Modes with consecutive radial order are connected with a thin black line.

trapping effects inflicted by the presence of internal chemical transition regions.

Since six periods of RXJ 2117 that are common to both Vauclair et al. (2002) and *TESS* data sets were measured at different epochs spanning 26 or 27 years, it is interesting to test their stability in time. However, with only a few measurements and a  $\sim 25$ -years gap, we can not know if the periods that seem relatively stable in the upper panel of Fig. 11 are *really* stable. On the other hand, we see at least two periods, those near 902 and 1043 s, that show significant period variations. In particular, the period at  $\sim 1043$  s show strong variations that are clearly anticorrelated with amplitude variations (lower panel of Fig. 11), and we know that correlated or anticorrelated variations of period and amplitude are typical of nonlinear interactions between different pulsation modes (see, e.g., Zong et al. 2018). The lower panel of Fig. 11 shows that, except for the period at  $\sim 1037$  s, all the others vary in amplitude. In addition to the period at  $\sim 1043$  s, which we have already mentioned, another period at 821.1 s, rather stable over the period, shows strong variations in amplitude, up to a factor  $\sim 4$  in about one year.

#### 4.2. Period spectrum of HS 2324

At variance with the case of RX J2117, for HS 2324 we find a *TESS* pulsation spectrum quite similar to that resulting from the ground-based observations. In Fig. 12 we schematically show the 12 periods detected with *TESS* (upper panel), and the 19 periods detected by Silvotti et al. (1999) (lower panel). Only two periods, around 2110 s and 2194 s, are nearly identical between both sets of data. In order to find a period spacing in HS 2324, we enlarged the list of periods by adding some of the 19 periods observed by Silvotti et al. (1999).

In that article, the authors note that the solution reported in their Table 2 was not univocal, probably because of insufficient frequency resolution and/or amplitude variations with time. We re-analyzed those data with different criteria for the pre-whitening procedure, in order to verify which frequencies are found in different solutions, and we selected 11 periods that were added to the list of periods collected by *TESS* (Table 4). The periods are slightly different from those in Table 2 of Silvotti et al. (1999) because we use the mean values of the different solu-

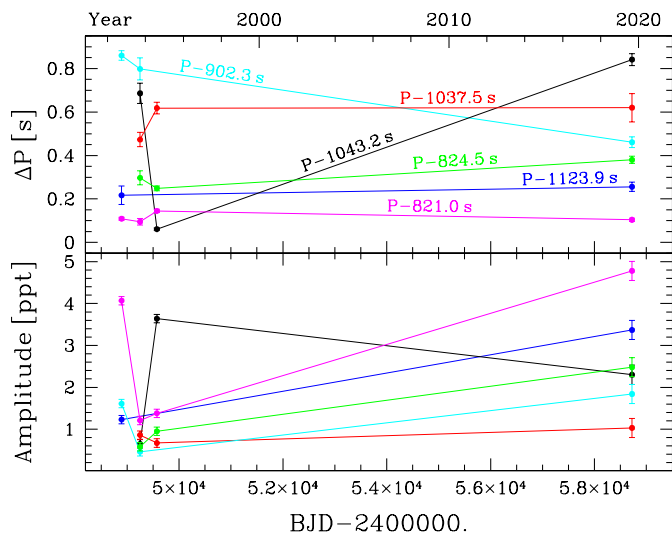


**Fig. 11.** Period variations (upper panels) and amplitudes (lower panels) of the six periods of RX J2117 that are common to the Vauclair et al. (2002) and *TESS* data sets. In the upper panel we have subtracted to each period a constant value in order to fit all periods within a narrow range.

**Table 10.** Enlarged list of periods of HS 2324. Column 1 corresponds to a subset of 11 periods estimated by Silvotti et al. (1999) (SEA99) with small differences (see text), and column 2 corresponds to the 12 periods detected with *TESS* (Table 4). The periods with an asterisk are the ones used in the linear least square fit (Fig. 14).

$\Pi_i^O$ (s) SEA99	$\Pi_i^O$ (s) <i>TESS</i>	$\Pi_{\text{fit}}$ (s)	$\delta\Pi$ (s)	$\ell^O$
1039.02				?
1047.10		1044.930	2.170	1
	1049.877			?
2005.78				?
	2027.520			?
	2029.350*	2029.350	0.000	1
	2047.260*	2045.757	1.503	1
2059.97*		2062.164	-2.194	1
	2076.110			?
2078.59*		2078.571	0.019	1
	2095.046*	2094.978	0.068	1
2098.67				?
2109.53	2110.152*	2111.385	-1.233	1
	2160.970*	2160.606	0.364	1
2170.49				?
	2175.290*	2177.013	-1.723	1
2194.12	2193.420*	2193.420	0.000	1
	2202.990			?
2553.23		2554.374	-1.144	1
2568.86		2570.781	-1.921	1
	2682.050	2685.630	-3.580	1

tions. For the two periods found in both data sets at  $\sim 2110$  s and  $\sim 2194$  s, we adopt the periods measured by *TESS* because they have smaller uncertainties. The extended list of periods to be used in our analysis contains 21 periods and is presented in Table 10.

In Fig. 13 we show the results of applying the statistical tests to the set of 21 periods of Table 10. The three tests support the existence of a mean period spacing of about 16 s, which corre-

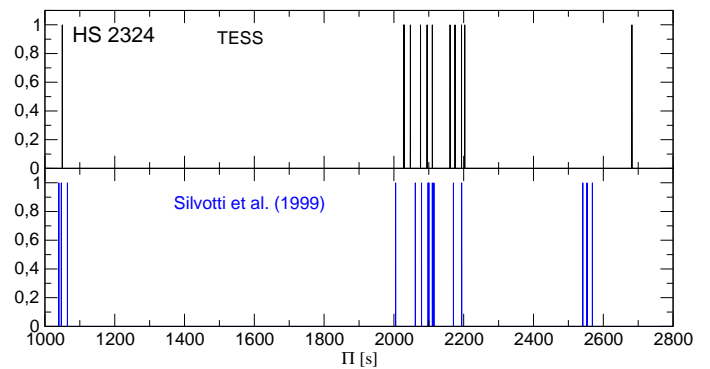


**Fig. 12.** Schematic distribution of the pulsation periods of HS 2324 according to *TESS* data (12 periods, black lines, upper panel), and according to Silvotti et al. (1999) (19 periods, blue lines, lower panel). The amplitudes have been arbitrarily set to one for clarity.

sponds to our expectations for a dipole ( $\ell = 1$ ) sequence<sup>5</sup>. Assuming that the peak at  $\sim 16$  s is associated to  $\ell = 1$  modes, then if a series of quadrupole ( $\ell = 2$ ) modes were present, one should find a spacing of periods of  $\sim 9$  s. This is not observed in our analysis (see Fig. 13). To determine precisely the period spacing, we did a linear least-squares fit (plotted in the upper panel of Fig. 14) using only nine periods, those marked with an asterisk in Table 10. The reason is that the other potential  $\ell = 1$  periods are much shorter or much longer and not well constrained, and we risk to assign them a wrong identification. We obtain a period spacing  $\Delta\Pi = 16.407 \pm 0.062$  s and with this value we determine four more periods compatible with the  $\ell = 1$  sequence, at about 1047, 2553, 2569 and 2682 s. If we include in the linear least-squares fit also these four periods, we obtain  $\Delta\Pi = 16.371$  s. We can conclude that Table 10 contains an incomplete sequence of 13 modes  $\ell = 1$ . The remainder periods, on the other hand, can be associated with modes with  $\ell = 1$  or modes with  $\ell = 2$  as well. In Sect. 7.2 we obtain an estimate of the stellar mass of HS 2324 on the basis of the period spacing. The lower panel of Fig. 14 displays the residuals between the observed periods and the periods derived from the mean period spacing. We note the presence of several minima in the distribution of residuals, similar to the case of RX J2117, which suggests the presence of mode trapping caused by chemical-composition gradients.

Note that, as discussed in Sect. 3.2, a rotational splitting of  $\sim 4.3$   $\mu\text{Hz}$  cannot be completely discarded in the frequency spectrum of HS 2324. In such case, we should have to consider only one component of the two possible incomplete triplets constituted by the pairs (481.67, 477.316)  $\mu\text{Hz}$  and (492.769, 488.458)  $\mu\text{Hz}$  when looking for a constant period spacing. On the one hand, from the pair (481.67, 477.316)  $\mu\text{Hz}$  we can adopt the frequency 477.316  $\mu\text{Hz}$ , that corresponds to the period 2095.046 s, and discard the period 2076.11 s from the analysis. This is precisely what we have done in the analysis above. In relation to the other pair of frequencies, based on the arguments discussed in the Section 3.2, we can adopt the frequency 492.769  $\mu\text{Hz}$  that corresponds to the period 2029.35 s<sup>6</sup>. Repeating the calculation of the period spacing, but this time ne-

<sup>5</sup> We can safely rule out that this peak corresponds to  $\ell = 2$  modes because in that case, we should find a peak at  $16 \text{ s} \times \sqrt{3} \sim 28$  s associated to  $\ell = 1$  modes, according to Eq. (1), which is not observed.

<sup>6</sup> This implies discarding the period 2047.26 s (frequency 488.458  $\mu\text{Hz}$ ) from our analysis, which makes sense since it has much lower amplitude than the period 2029.35 s (492.769  $\mu\text{Hz}$ ) (see Table 4 and Fig. 6).

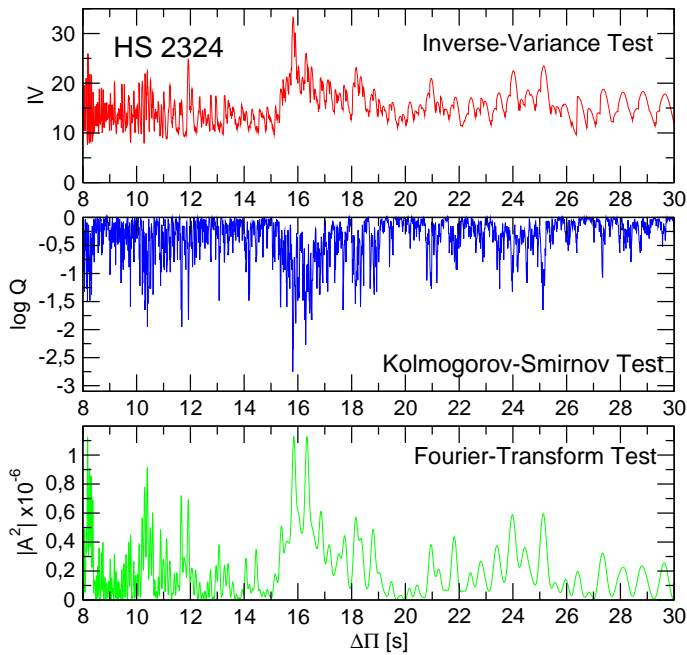


**Fig. 13.** I-V (upper panel), K-S (middle panel), and F-T (bottom panel) significance tests to search for a constant period spacing in HS 2324. The tests are applied to the 21 pulsation periods in Table 10. A clear signal of a constant period spacing at  $\sim 16$  s is evident. See text for details.

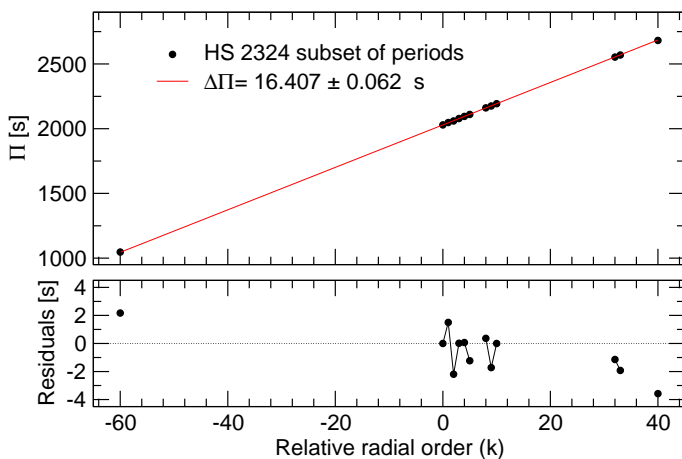


**Fig. 14.** Upper panel: linear least-squares fit to the 9 periods of HS 2324 marked with asterisk in Table 4. The derived dipole ( $\ell = 1$ ) mean period spacing from this fit is  $\Delta\Pi = 16.407 \pm 0.062$  s. Lower panel: the residuals of the period distribution relative to the mean period spacing, showing observational evidence of mode trapping in the pulsation spectrum of HS 2324. Modes with consecutive radial order are connected with a thin black line.

glecting the period of 2047.26 s from the analysis (that is, adopting a list of 8 periods), we obtain  $\Delta\Pi = 16.421 \pm 0.120$  s, virtually the same period spacing obtained above ( $\Delta\Pi = 16.407 \pm 0.062$  s). In summary, if we consider the possible existence of two incomplete rotational triplets, it does not alter the results in relation to the period spacing of HS 2324.

Since the epochs of the two data sets of HS 2324 differ by 22 years, by comparing the values of the two periods found in both data sets we can test their temporal stability. However, we know that the formal uncertainties given in Table 2 of Silvotti et al. (1999) are underestimated as the periods change slightly depend-

ing on which solution is adopted. By testing different solutions, from the 1997 data we obtain  $2109.53 \pm 0.66$  and  $2194.12 \pm 0.15$  with more realistic uncertainties. The much larger uncertainty on the first period is due to the presence of close-by peaks, not visible in the *TESS* run, which are probably the cause of the varying amplitude ( $\sim 3.3$  ppt in 1997, 6.0 ppt in 2019). In 2019 the periods are  $2110.15 \pm 0.04$  s and  $2193.42 \pm 0.06$  s (adopting the formal uncertainties of the fit). Only for the second one near 2193 s, which has a fairly stable amplitude (4.3 ppt in 1997 and 4.0 ppt in 2019, considering also the much redder sensitivity of *TESS*), the period change in time is significant ( $4.7\sigma$ ), corresponding to  $\dot{\Pi} = (-1.0 \pm 0.3) \times 10^{-9}$  s/s. Even though this value is close to theoretical predictions (see Sect. 7.2), the fact that we have only two measurements and that we know that the periods may have irregular variations on different time scales (as we have seen for RX J2117) suggests caution.

#### 4.3. Period spectrum of NGC 6905

As in the cases of RX J2117 and HS 2324, we find a pulsation spectra of NGC 6905 quite different as compared with the results of ground-based observations. In Fig. 15 we schematically show the 4 periods detected with *TESS* (upper panel, black lines), and the 7 periods detected by Ciardullo & Bond (1996) (lower panel, blue lines), with arbitrary amplitudes set to one to facilitate visualization. In order to search for a period spacing in NGC 6905 we enlarged the list of periods by adding the 7 periods measured by Ciardullo & Bond (1996) to the list of periods collected by *TESS*. The extended list of periods to be used in our analysis, that contains 11 periods, is presented in Table 11.

We applied the three statistical tests adopting the complete list of 11 periods of Table 11, and we did obtain a clear indication of a constant period spacing of  $\sim 12$  s, as can be seen in Fig. 16. A priori, we cannot know what harmonic degree this apparent constant period spacing corresponds to. Being so short, one is tempted to assume that it is a period spacing of  $\ell = 2$  modes, but in this case, we should find a period spacing of about 21 s corresponding to  $\ell = 1$  modes, which is absent. The absence of a period spacing at  $\sim 21$  s, is not, however, a strong reason to discard the possibility that the period spacing of  $\sim 12$  s is associated to a sequence of  $\ell = 2$  modes. Indeed, it could be possible that the  $\ell = 1$  modes (and the associated period spacing) are inhibited for some reason. For example, it could be that  $\ell = 1$  modes are not excited at the effective temperature and gravity of NGC 6905, but  $\ell = 2$  modes are unstable. In Sect. 7.3, we will consider the possibilities that  $\Delta\Pi \sim 12$  s is associated to  $\ell = 1$  or  $\ell = 2$  modes when estimating the stellar mass of NGC 6905.

In order to refine this period-spacing value, we first performed a linear least-squares fit to the periods marked with asterisk in Table 11, except the period at 710.37 s, because it is far from the remainder ones and this could affect the assignment of its relative radial order. We obtain a period spacing  $\Delta\Pi = 11.7769 \pm 0.2247$  s. The average value of the residuals resulting from the difference between the periods observed and those calculated from the period spacing obtained is 1.395 s. We repeated the linear least-squares fit but this time including the period at 710.37 s, and we obtained  $\Delta\Pi = 11.9693 \pm 0.0988$  s. Note that this period spacing is slightly longer than that derived neglecting the period at 710.37 s in the linear least-squares fit, but the uncertainty is more than two times smaller. In addition, the average of the residuals in this case is 1.023 s, so the fitted periods match the observed periods much better than before. For this reason, we adopt  $\Delta\Pi = 11.9693 \pm 0.0988$  s as the period spacing for NGC 6905. We show the periods derived with the fit



**Table 11.** Enlarged list of periods of NGC 6905. Column 1 corresponds to the 7 periods measured by Ciardullo & Bond (1996) (CB96), and column 2 corresponds to the 4 periods detected by *TESS*. Columns 3 to 5 have the same meaning as in Table 9. The periods with an asterisk are the ones used in the linear least square fit (Fig. 17).

$\Pi_i^O$ (s) CB96	$\Pi_i^O$ (s) <i>TESS</i>	$\Pi_{\text{fit}}$ (s)	$\delta\Pi$ (s)	$\ell^O$
710.37*		710.908	-0.538	1
	816.337			1
	818.887*	818.632	0.255	1
851.38				?
	855.613*	854.540	1.074	1
	865.490*	866.509	-1.109	1
874.80				?
879.79*		878.479	1.311	1
884.00				?
891.39*		890.448	0.942	1
912.36*		914.386	-2.026	1

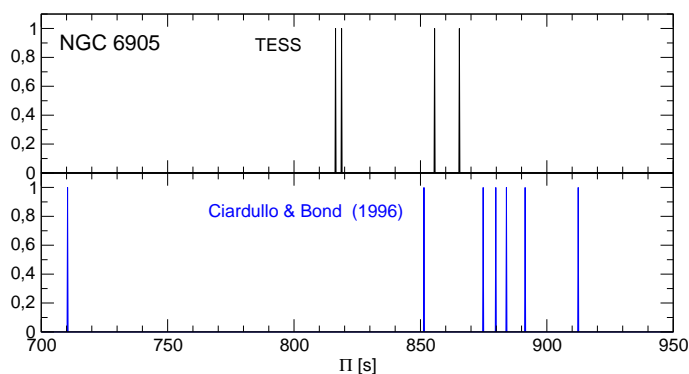


**Fig. 15.** Schematic distribution of the pulsation periods of NGC 6905 according to *TESS* (black lines, upper panel), and according to Ciardullo & Bond (1996) (blue lines, lower panel). The amplitudes have been arbitrarily set to one for clarity.

( $\Pi_{\text{fit}}$ ) and the residuals ( $\delta\Pi$ ) in columns 3 and 4, respectively, of Table 11. In the last column we show the possible identification of the fitted periods with  $\ell = 1$  modes, although, as stated above, they could be all associated to  $\ell = 2$  modes. In the upper panel of Fig. 17 we show the fit, whereas in the lower panel we depict the residuals.

#### 4.4. Period spectrum of NGC1501

As for the targets analyzed before, a comparison of the pulsation spectrum of NGC 1501 detected by *TESS* with that obtained through the ground-based monitoring by Bond et al. (1996) reveals that the pulsation spectra are markedly different. In Fig. 18 we schematically show the periods detected with *TESS* (upper panel, black lines), and the 11 periods detected by Bond et al. (1996) (lower panel, blue lines)—specifically, those of their Table 4—with arbitrary amplitudes set to one to facilitate visualization. As before, we consider here the composed pulsation spectrum of NGC 1501, that is, the list of periods measured by *TESS* along with the periods determined by Bond et al. (1996). The extended list of periods to be used in our analysis is presented in columns 1 and 2 of Table 12.

In Fig. 19 we show the results of applying the statistical tests to the complete set of 26 periods of Table 12. The three tests support the existence of two period spacings of about 11.9 s and

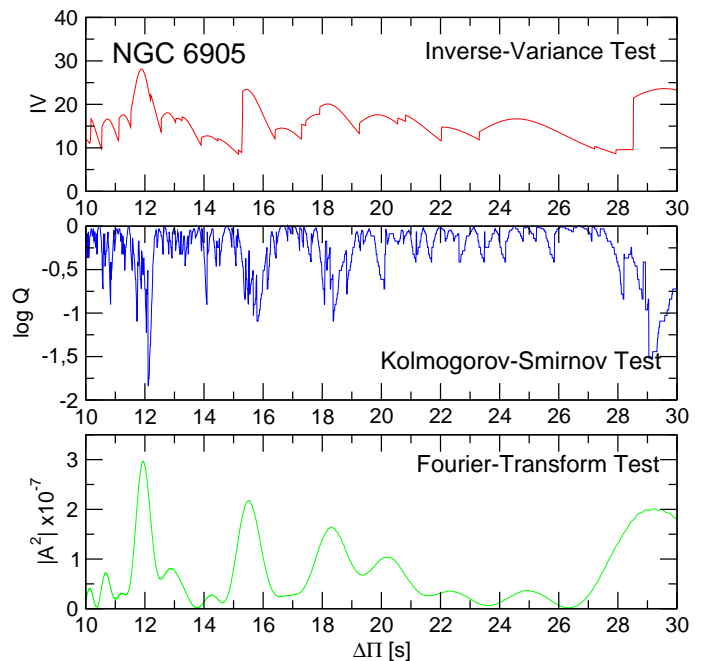


**Fig. 16.** I-V (upper panel), K-S (middle panel), and F-T (bottom panel) significance tests to search for a constant period spacing in NGC 6905. The tests are applied to the 11 pulsation periods of Table 11. A clear signal of a constant period spacing at  $\sim 12$  s is evident. See text for details.

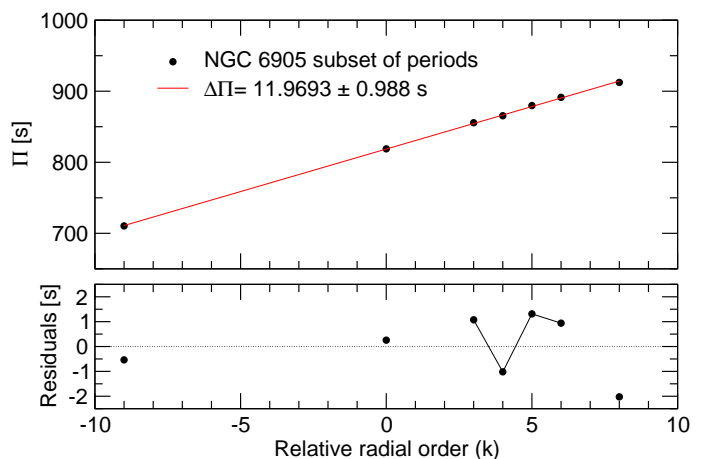


**Fig. 17.** Upper panel: linear least-squares fit to the 7 periods of NGC 6905 marked with asterisk in Table 11. The derived period spacing from this fit is  $\Delta\Pi = 11.9693 \pm 0.988$  s. Lower panel: residuals of the period distribution relative to the dipole mean period spacing. Modes with consecutive radial order are connected with a thin black line.

20.1 s. The ratio between the two values is  $20.1/11.9 = 1.689$ , close to the expected value of  $\sqrt{3} = 1.732$  if we assume that these are period spacings associated to  $\ell = 1$  ( $\Delta\Pi_{\ell=1} \sim 20.1$  s) and  $\ell = 2$  ( $\Delta\Pi_{\ell=2} \sim 11.9$  s), according to Eq. (1). Period spacings due to  $\ell = 1$  and  $\ell = 2$  modes in the same object are not common to find in the context of GW Vir stars, the only known case so far being the prototypical variable star PG 1159-035 (see, e.g., Winget et al. 1991; Costa et al. 2008).

We have alternatively considered in our analysis the 9 ( $m = 0$ ) periods of the Table 7 of Bond et al. (1996), which consist of a composition of the data from that work plus archival period data on NGC 1501. However, by putting together those periods with the periods measured with *TESS* in this paper, we do not obtain

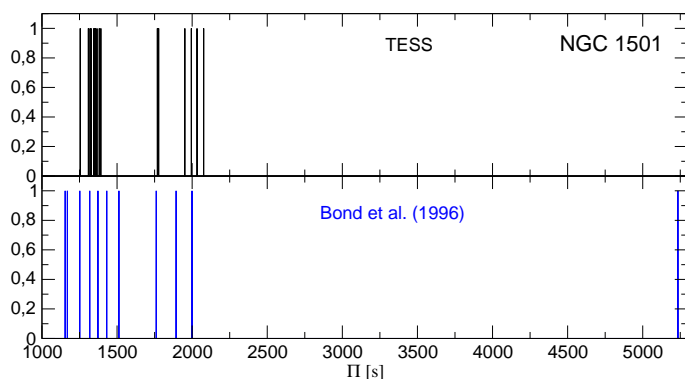


**Fig. 18.** Schematic distribution of the pulsation periods of NGC 1501 according to *TESS* (black lines, upper panel), and according to Table 4 of Bond et al. (1996) (blue lines, lower panel). The amplitudes have been arbitrarily set to one for clarity.

any clear pattern of constant period spacing, and therefore, we do not consider them here.

We perform a linear least-squares fit using the 14 periods marked with an asterisk in Table 12, which gives a period spacing  $\Delta\Pi_{\ell=1} = 20.1262 \pm 0.0123$  s associated with  $\ell = 1$  modes. We perform a second least-squares fit employing the 9 periods marked with two asterisks in the same table, which gives a period spacing  $\Delta\Pi_{\ell=2} = 11.9593 \pm 0.0520$  s that is probably associated with  $\ell = 2$  modes. With  $\Delta\Pi_{\ell=2}$ , we compute an additional period compatible with the  $\ell = 2$  sequence, at about 1760.7 s. The ratio between the two period spacings is  $20.1262/11.9593 = 1.683$ . The fits are plotted in the upper panel of Fig. 20, and the residuals are depicted in the middle panel ( $\ell = 1$ ) and in the lower panel ( $\ell = 2$ ).

Note that there are two periods (1318.46 s and 1999.16 s) that do not fit neither the  $\ell = 1$  nor the  $\ell = 2$  series of periods with constant period spacing. For these two periods, we cannot determine the harmonic degree. These periods either correspond both to  $\ell = 1$  or  $\ell = 2$  modes that are departed from the sequences of equally spaced periods due to mode trapping effects, or they can be alternatively interpreted as  $m \neq 0$  components of incomplete rotational multiplets—but we have no indication of the presence of rotational multiplets in this star. Alternatively, these two periods could correspond to  $\ell = 3$  modes, although this is unlikely due to the low chance of being detected by the geometric cancellation effects (Dziembowski 1977).

In closing this Section, we call the attention about a possible alternative interpretation of the period spacing derived for NGC 1501. Specifically, by examining Fig. 19, we see the presence of a strong peak for  $\Delta\Pi \sim 8 - 9$  s. This peak could be associated to the  $\ell = 2$  period spacing of the star. If this were the case, then we should expect to find a peak corresponding to the  $\ell = 1$  period spacing at  $\Delta\Pi \sim 16$  s. However, that peak is not visible in any of the tests. For this reason, we rule out this possibility.

In Sect. 7.4 we obtain an estimate of the stellar mass of NGC 1501 on the basis of the period-spacing values derived in this section,  $\Delta\Pi_{\ell=1} = 20.1262 \pm 0.0123$  s and  $\Delta\Pi_{\ell=2} = 11.9593 \pm 0.0520$  s.

#### 4.5. Period spectrum of NGC 2371

NGC 2371 was observed from the ground by Ciardullo & Bond (1996). An illustrative comparison between periods detected from ground-based observations and those detected by *TESS*

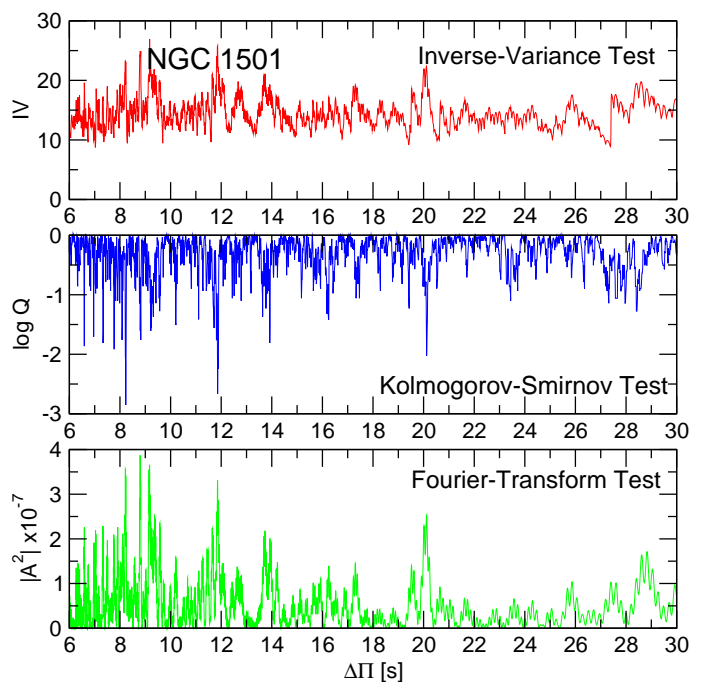


**Fig. 19.** I-V (upper panel), K-S (middle panel), and F-T (bottom panel) significance tests to search for a constant period spacing in NGC 1501. The tests are applied to the pulsation periods in Table 12 which are marked with an asterisk. The three tests indicate clear signals of two constant period spacings of  $\sim 11.9$  s and  $\sim 20.1$  s. See text for details.

is shown in Fig. 21. An examination of this figure reveals that both pulsation spectra are markedly different. In particular, Ciardullo & Bond (1996) report several periods longer than the longest period detected with *TESS* ( $\sim 968$  s). As before, we adopt an augmented pulsation spectrum of NGC 2371, composed by the periods measured by *TESS* along with the periods determined by Ciardullo & Bond (1996), specifically, those of their Table 4 which are considered as secure. The extended list of periods to be used in our analysis is presented in Table 13.

In Fig. 22 we show the results of applying the statistical tests to the set of periods of Table 13 marked with an asterisk. The three tests support the existence of a mean period spacing of about 14.5 s which corresponds to our expectations for a dipole ( $\ell = 1$ ) sequence. A linear least-squares fit using the 8 periods marked with asterisk in Table 13 gives a period spacing  $\Delta\Pi = 14.5312 \pm 0.0226$  s. The fit is plotted in the upper panel of Fig. 23, and the residuals are depicted in the lower panel of the same figure. In Sect. 7.5 we obtain an estimate of the stellar mass of NGC 2371 on the basis of the period spacing.

#### 4.6. Period spectrum of K 1–16

K 1–16 was observed from the ground by Grauer & Bond (1984), detecting a complex power spectrum with a dominant periodicity of  $\sim 1700$  s. After the delivery of *TESS* data from sectors 14 and 15, the star showed no variability. Finally, with the release of observations from the sectors 16–17, 19–20, and 22–26, a total of six (or seven) periods were detected. However, the power spectrum is so complex and noisy that the values of the periods are hard to estimate (Table 8). The peak at the frequency  $7752 \mu\text{Hz}$  corresponds to a period of 129 s. This is a very short period as to be excited in GW Vir stars by the  $\kappa - \gamma$  mechanism, therefore, if this period is real, it could correspond to a low-order mode excited by the  $\varepsilon$  mechanism acting at the He-

**Table 12.** Enlarged list of periods of NGC 1501. Column 1 corresponds to the 11 periods of Table 4 of Bond et al. (1996) (BEA96), and column 2 corresponds to the 15 periods detected by *TESS* (Table 6). Columns 3 and 4 (5 and 6) correspond to the fitted periods from the  $\ell = 1$  ( $\ell = 2$ ) period spacing, and column to 7 gives the “observed” harmonic degree.

$\Pi^0$ (s) BEA96	$\Pi^0$ (s) <i>TESS</i>	$\Pi_{\text{fit}}^{\ell=1}$ (s)	$\delta\Pi^{\ell=1}$ (s)	$\Pi_{\text{fit}}^{\ell=2}$ (s)	$\delta\Pi^{\ell=2}$ (s)	$\ell^0$
1154.36**				1155.070	-0.710	2
1168.90*		1168.730	0.170			1
1251.91*		1249.235	2.675			1
	1254.632**			1250.744	3.888	2
	1309.086**			1310.541	-1.455	2
	1310.696*	1309.613	1.083			1
1318.46						?
	1321.095**			1322.500	-1.405	2
	1345.872**			1346.419	-0.547	2
	1349.460*	1349.866	-0.406			1
	1356.680**			1358.042	-1.362	2
	1366.279*	1369.992	-3.713			1
1372.94**				1370.337	2.603	2
	1381.295**			1382.297	-1.002	2
	1392.240*	1390.118	2.122			1
1431.53*		1430.371	1.159			1
1512.66*		1510.875	1.785			1
1760.73				1764.994	-4.264	2
	1768.510*	1772.516	-4.006			1
	1777.290**			1776.954	0.336	2
1892.95*		1893.273	-0.323			1
	1951.490*	1953.652	-2.162			1
1999.16						?
	2032.640*	2034.157	-1.547			1
	2077.000*	2074.409	2.591			1
5234.81*		5234.222	0.588			1

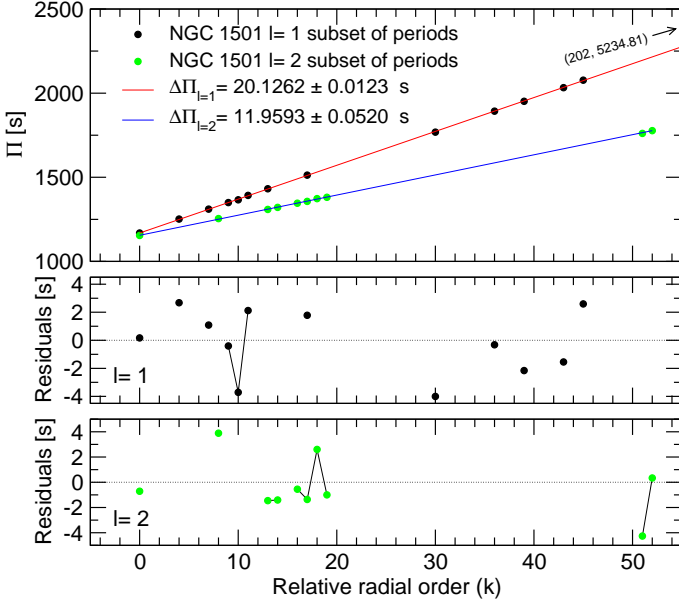


**Fig. 20.** Upper panel: the linear least-squares fits to the 14 dipole periods of NGC 1501 marked with an asterisk and the 9 quadrupole periods marked with two asterisks in Table 6. The derived period spacings from these fits are  $\Delta\Pi_{\ell=1} = 20.1262 \pm 0.0123$  s and  $\Delta\Pi_{\ell=2} = 11.9593 \pm 0.0520$  s, respectively. Middle panel: the residuals of the  $\ell = 1$  period distribution relative to the dipole mean period spacing. Lower panel: residuals of the  $\ell = 2$  period distribution relative to the quadrupole mean period spacing. Modes with consecutive radial order are connected with a thin black line.

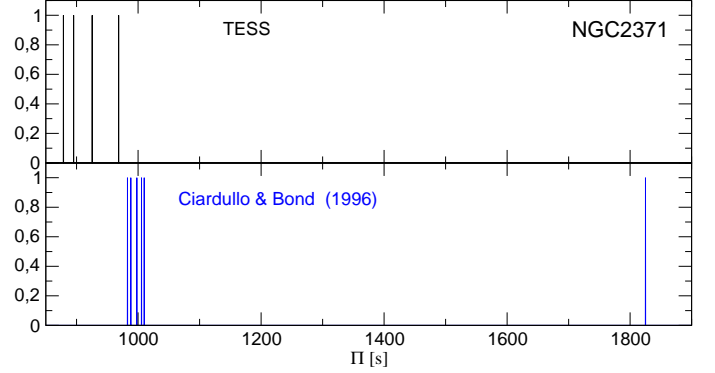


**Fig. 21.** Illustrative distribution of the pulsation periods of NGC 2371 according to *TESS* (black lines, upper panel), and according to Ciardullo & Bond (1996), their Table 4 (blue lines, lower panel). The amplitudes have been arbitrarily set to one for clarity.

burning shell (Córscico et al. 2009b). Bringing together observations from the ground and from space, the star exhibits a total of at least 7 periods which vary in amplitude on weekly time scales. We have not found any clear regularity in the spacing of periods that can give us any clue to its stellar mass, as it was the case with the other targets in this study. Given the complexity and the extremely variable spectrum of periods of K 1–16, and having so few periods available, we are prevented from carrying out an in-depth asteroseismological analysis of this star, either with the period spacing or the individual periods.

**Table 13.** Enlarged list of periods of NGC 2371. Column 1 corresponds to the 6 secure periods of Table 4 of Ciardullo & Bond (1996) (CB96), and column 2 corresponds to the 4 periods detected by *TESS* (Table 7). The periods with an asterisk are the ones used in the linear least-square fit (Fig. 23). Columns 3 to 5 have the same meaning as in Table 9.

$\Pi^O$ (s) CB96	$\Pi^O$ (s) <i>TESS</i>	$\Pi_{\text{fit}}$ (s)	$\delta\Pi$ (s)	$\ell^O$
	878.523*	880.598	-2.075	1
	895.111*	895.129	-0.018	1
	925.465*	924.192	1.273	1
	968.474*	967.785	0.689	1
982.8*		982.316	0.158	1
988.2				?
998.0*		996.848	1.152	1
1005.6				?
1010.0*		1011.379	-1.379	1
1825.0*		1825.126	-0.126	1

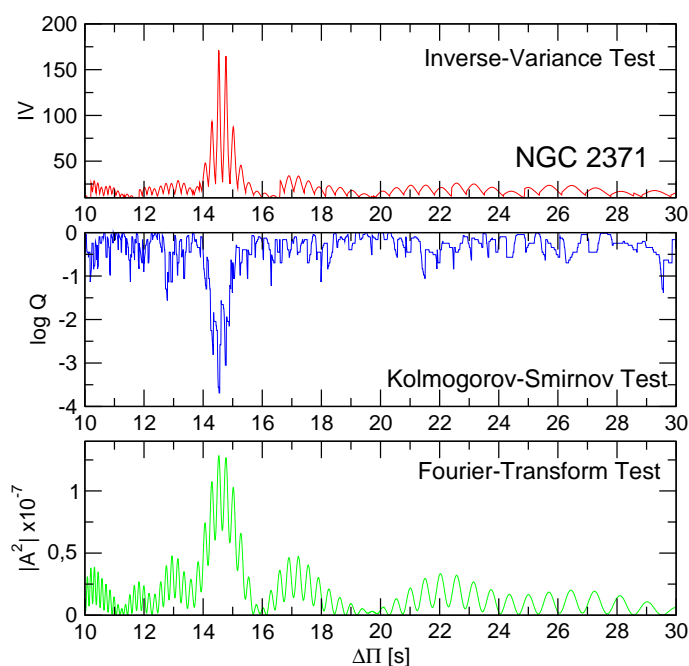


**Fig. 22.** I-V (upper panel), K-S (middle panel), and F-T (bottom panel) significance tests to search for a constant period spacing in NGC 2371. The tests are applied to the pulsation periods in Table 13 which are marked with an asterisk. The three tests indicate clear signals of a constant period spacing of  $\sim 14.5$  s. See text for details.

## 5. Evolutionary models and numerical codes

The asteroseismological analysis presented in this work relies on a set of state-of-the-art stellar models that take into account the complete evolution of the PG 1159 progenitor stars. Specifically, the stellar models were extracted from the evolutionary calculations presented by Althaus et al. (2005) and Miller Bertolami & Althaus (2006), who computed the complete evolution of model star sequences with initial masses on the ZAMS in the range  $1 - 3.75 M_{\odot}$  and assuming a metallicity of  $Z = 0.02$ . All of the post-AGB evolutionary sequences computed with the LPCODE evolutionary code (Althaus et al. 2005) were followed through the very late thermal pulse (VLTP) and the resulting born-again episode that give rise to the H-deficient, He-, C- and O-rich composition characteristic of PG 1159 stars.

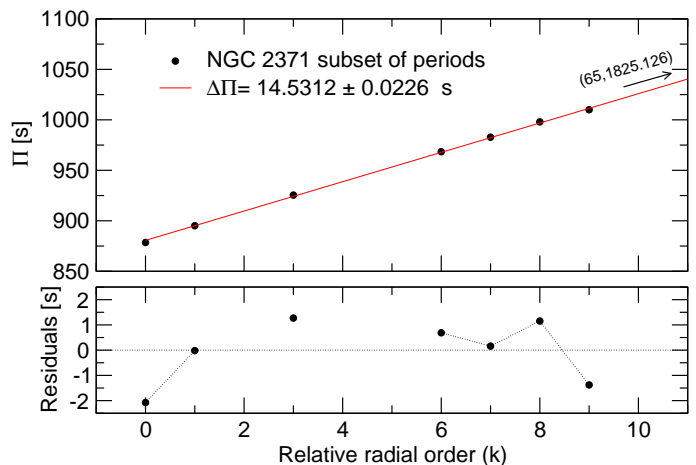


**Fig. 23.** Upper panel: linear least-squares fit to the 8 periods of NGC 2371 marked with asterisk in Table 7. Lower panel: the residuals between the observed and the fitted periods. The derived period spacing from this fit is  $\Delta\Pi = 14.5312 \pm 0.0226$  s.

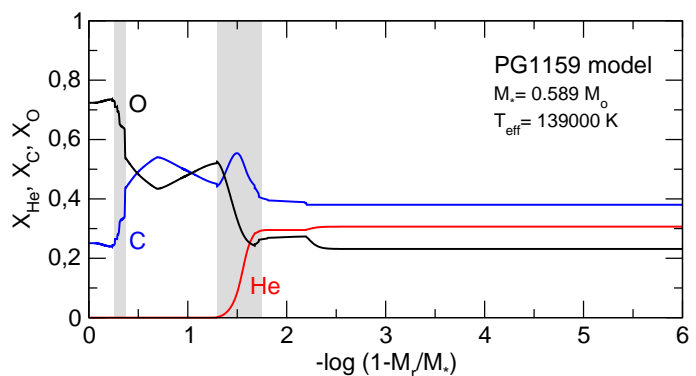


**Fig. 24.** The internal chemical profile of a template PG 1159 model ( $M_{\star} = 0.589 M_{\odot}$ ,  $T_{\text{eff}} = 139\,000$  K) in terms of the outer fractional mass. The locations of the O/C and O/C/He chemical interfaces are indicated with gray regions.

The masses of the resulting remnants are  $0.530, 0.542, 0.565, 0.589, 0.609, 0.664,$  and  $0.741 M_{\odot}$ . In Fig. 1 the evolutionary tracks employed in this work are shown in the  $\log T_{\text{eff}}$  vs.  $\log g$  plane. For details about the input physics and evolutionary code, and the numerical simulations performed to obtain the PG 1159 evolutionary sequences employed here, we refer the interested reader to the works by Althaus et al. (2005) and Miller Bertolami & Althaus (2006, 2007a,b). Here, we give a brief description of the chemical structure of our PG 1159 models. In Fig. 24 we show the fractional abundances of the main chemical species,  ${}^4\text{He}$ ,  ${}^{12}\text{C}$ , and  ${}^{16}\text{O}$ , corresponding to a model with  $M_{\star} = 0.589 M_{\odot}$  and  $T_{\text{eff}} = 139\,000$  K. Clearly visible are the chemical transition regions of O/C and O/C/He. The location, thickness, and steepness of these chemical interfaces define the mode-trapping properties of the models. Generally, the mode-trapping features in the pulsation spectrum of these models for periods shorter than about 700 s are induced mostly by the chemical gradient at the O/C/He interface, with the O/C chemical transition being much less relevant. For longer periods, however, it is the core chemical structure in the O/C interface that mostly fixes the mode trapping properties (see, e.g., Córscico & Althaus 2005, 2006, for details).

As mentioned, the star HS 2324 is a hybrid PG 1159 star, i.e., it has H on its surface. The presence of H is not expected

to substantially modify the evolutionary tracks (Löbbling et al. 2019) nor the pulsation properties of these stars, when compared with the standard case of PG 1159 stars which lack of H. This is due to the fact that, at those evolutionary stages, element diffusion is not operative, and thus vestiges of H left by prior evolution are uniformly distributed throughout the outer layers of the star, instead of forming a pure-H envelope. Therefore, as a valid approximation, this star will be analyzed in this work using PG 1159 evolutionary models that do not have H in their surfaces.

We have computed  $\ell = 1, 2$   $g$ -mode adiabatic pulsation periods in the range 80 – 6000 s with the adiabatic and nonadiabatic versions of the pulsation code LP-PUL (Córscico & Althaus 2006; Córscico et al. 2006) and the same methods we employed in the previous works of La Plata Stellar Evolution and Pulsation Research Group<sup>7</sup>. We analyzed about 4 000 PG 1159 models covering a wide range of effective temperatures ( $5.4 \gtrsim \log T_{\text{eff}} \gtrsim 4.8$ ), luminosities ( $0 \lesssim \log(L_*/L_\odot) \lesssim 4.2$ ), and stellar masses ( $0.530 \leq M_*/M_\odot \leq 0.741$ ).

## 6. Spectroscopic masses

On the basis of the evolutionary tracks presented in Fig. 1 and the published values of the spectroscopic surface gravity and temperature, we derive by interpolation a value of the spectroscopic mass of each of the six analyzed stars. In the case of RX J2117 we get a stellar mass of  $M_* = 0.716 \pm 0.150 M_\odot$ . As for HS 2324, we get a stellar mass of  $M_* = 0.532 \pm 0.150 M_\odot$ , while for NGC 6905 and NGC 1501 we derive  $M_* = 0.590 \pm 0.150 M_\odot$  and  $M_* = 0.565 \pm 0.150 M_\odot$ , respectively. We obtain  $M_* = 0.533 \pm 0.150 M_\odot$  for NGC 2371. Finally, we derive  $M_* = 0.742 \pm 0.150 M_\odot$  for K 1–16. The uncertainties in the stellar mass are estimated from the uncertainties in the  $T_{\text{eff}}$  and  $\log g$  values adopting the extreme values of each parameter when interpolating between the evolutionary tracks of Fig. 1.

## 7. Asteroseismic modelling

The methods we use in this paper to extract information of the stellar mass and the internal structure of RX J2117, HS 2324, NGC 2371, NGC 6905, NGC 1501, NGC 2371, and K 1–16 are the same employed in our previous works (see Córscico et al. 2007a,b, 2008, 2009a; Kepler et al. 2014; Calcaferro et al. 2016). In brief, a way to derive an estimate of the stellar mass of GW Vir stars is by comparing the observed period spacing of a target star ( $\Delta\Pi$ ) with the asymptotic period spacing ( $\overline{\Delta\Pi}_\ell^a$ ) computed with Eq. (1) at the effective temperature of the star (see the pioneer work of Kawaler 1988). GW Vir stars generally do not have all of their pulsation modes in the asymptotic regime, so there is usually no perfect agreement between  $\Delta\Pi$  and  $\overline{\Delta\Pi}_\ell^a$ . Therefore, the derivation of the stellar mass using the asymptotic period spacing may not be entirely reliable in pulsating PG 1159 stars that pulsate with modes characterized by low and intermediate radial orders, but it gives a good estimate of the stellar mass for stars pulsating with  $g$  modes of high radial order (see Althaus et al. 2008). A variation of this approach to infer the stellar mass of GW Vir stars is to compare  $\Delta\Pi$  with the average of the computed period spacings ( $\overline{\Delta\Pi}_k$ ). The average of the computed period spacings is assessed as  $\overline{\Delta\Pi}_k = (N - 1)^{-1} \sum_k \Delta\Pi_k$ , where the "forward" period spacing ( $\Delta\Pi_k$ ) is defined as  $\Delta\Pi_k = \Pi_{k+1} - \Pi_k$  ( $k$  being the radial order)

and  $N$  is the number of computed periods laying in the range of the observed periods. This method is more reliable for the estimation of the stellar mass of GW Vir stars than that described above using  $\overline{\Delta\Pi}_\ell^a$  because, provided that the average of the computed period spacings is evaluated at the appropriate range of periods, the approach is valid for the regimes of short, intermediate and long periods as well. When the average of the computed period spacings is taken over a range of periods characterized by high  $k$  values, then the predictions of the present method become closer to those of the asymptotic period-spacing approach (Althaus et al. 2008). On the other hand, the present method requires of detailed period computations, at variance with the method described above, that does not involve pulsational calculations. Note that both methods for assessing the stellar mass rely on the spectroscopic effective temperature, and the results are unavoidably affected by its associated uncertainty.

Another asteroseismological tool to disentangle the internal structure of GW Vir stars is to seek theoretical models that best match the individual pulsation periods of the target star. To measure the goodness of the match between the theoretical pulsation periods ( $\Pi_{\ell,k}$ ) and the observed individual periods ( $\Pi_i^o$ ), we follow the same procedure as in our previous works:

$$\chi^2(M_*, T_{\text{eff}}) = \frac{1}{N} \sum_{i=1}^N \min[(\Pi_{\ell,k} - \Pi_i^o)^2] \quad (3)$$

where  $N$  is the number of observed periods. The observed periods are shown in Tables 9, 10, 11, 12, and 13. In order to find the stellar model that best replicate the observed periods exhibited by each target star — the "asteroseismological" model —, we evaluate the function  $\chi^2$  for stellar masses  $M_* = 0.530, 0.542, 0.565, 0.589, 0.609, 0.664$ , and  $0.741 M_\odot$ . For the effective temperature we employ a much finer grid ( $\Delta T_{\text{eff}} = 10 - 30$  K). For each target star, the PG 1159 model that shows the lowest value of  $\chi^2$  is adopted as the best-fit asteroseismological model.

Below, we employ the tools described above to extract information of the GW Vir stars considered in this work.

### 7.1. RX J2117

For this star, we have calculated the average of the computed period spacings for  $\ell = 1$ ,  $\overline{\Delta\Pi}_k$ , in terms of the effective temperature for all the masses considered. The results are shown in Fig. 25, where we depict  $\overline{\Delta\Pi}_k$  corresponding to evolutionary stages before the maximum possible effective temperature,  $T_{\text{effMAX}}$  (that depends on the stellar mass) with red dashed lines, and the phases after that  $T_{\text{effMAX}}$  (the WD stage itself) with solid black lines. The location of RX J2117 is indicated by a small red circle with error bars, and corresponds to the effective temperature of the star according to Rauch & Werner (1997) and the period spacing derived in Sect. 3.1. The star has a period-spacing value between the values of the curves of  $0.565 M_\odot$  and  $0.589 M_\odot$  at the maximum temperature positions. We perform a linear interpolation between the maximum values of effective temperature for each sequence and obtain  $M_* = 0.569 \pm 0.015 M_\odot$ . This mass value is in good agreement with that inferred by Vauclair et al. (2002),  $M_* = 0.56^{+0.02}_{-0.04} M_\odot$ , and Córscico et al. (2007a),  $M_* = 0.560^{+0.018}_{-0.013} M_\odot$  that also use the period spacing to infer the stellar mass. Finally, we note that our inferred stellar mass value of  $M_* = 0.569 \pm 0.015 M_\odot$  is in strong disagreement with the spectroscopic mass,  $M_* = 0.716 \pm 0.150 M_\odot$  (see Sect. 5).

<sup>7</sup> <http://fcaglp.fcaglp.unlp.edu.ar/evolgroup/>

**Table 14.** Observed and theoretical periods of the asteroseismological model for RX J2117 [ $M_\star = 0.565M_\odot$ ,  $T_{\text{eff}} = 162\,992$  K,  $\log(L_\star/L_\odot) = 3.373$ ]. Periods are in seconds and rates of period change (theoretical) are in units of  $10^{-12}$  s/s.  $\delta\Pi_i = \Pi_i^O - \Pi_k$  represents the period differences,  $\ell$  the harmonic degree,  $k$  the radial order,  $m$  the azimuthal index. The last column gives information about the pulsational stability/instability nature of the modes.

$\Pi_i^O$ (s)	$\ell^O$	$\Pi_k$ (s)	$\ell$	$k$	$m$	$\delta\Pi_k$ (s)	$\dot{\Pi}_k$ ( $10^{-11}$ s/s)	Unstable
692.267	1	689.975	1	30	0	2.292	-2.561	no
712.975	1	712.003	1	31	0	0.972	-4.775	no
733.948	1	732.780	1	32	0	1.168	-5.217	no
757.354	1	754.864	1	33	0	2.490	-6.022	yes
778.921	1	777.318	1	34	0	1.603	-4.702	yes
799.495	1	798.832	1	35	0	0.663	-2.655	yes
817.375	1	...	1	36	-1	...	...	...
821.105	1	820.614	1	36	0	0.491	-2.508	yes
824.880	1	...	1	36	+1	...	...	...
843.692	1	843.310	1	37	0	0.382	-5.222	yes
885.736	1	887.005	1	39	0	-1.269	-7.721	yes
902.761	?	902.523	2	70	0	0.238	-7.666	yes
907.489	1	907.453	1	40	0	0.036	-7.849	yes
951.750	1	953.041	1	42	0	-1.291	-4.485	yes
966.785	1	...	1	43	-1	...	...	...
972.073	1	974.580	1	43	0	-2.507	-7.938	yes
994.387	1	994.737	1	44	0	-0.350	-10.487	yes
1016.467	1	1016.873	1	45	0	-0.406	-10.678	yes
1031.978	1	...	1	46	-1	...	...	...
1038.120	1	1039.311	1	46	0	-1.191	-11.222	yes
1044.041	1	...	1	46	+1	...	...	...
1058.026	1	1060.183	1	47	0	-2.157	-8.262	yes
1103.292	1	1103.398	1	49	0	-0.106	-12.206	yes
1124.156	1	1125.203	1	50	0	-1.047	-14.094	yes
1131.200	1	...	1	51	+1	...	...	...
1146.346	1	1146.771	1	51	0	-0.425	-11.240	yes
1189.956	1	1188.768	1	53	0	1.188	-8.643	yes
1350.870	?	1345.193	2	105	0	5.677	-9.485	no
1557.010	1	1559.013	1	70	0	-2.003	-13.293	no
1976.060	?	...	1	90	-1	...	...	...
1997.760	?	1998.018	1	90	0	-0.258	-8.917	no

**Table 15.** The main characteristics of the GW Vir star RX J2117. The second column corresponds to spectroscopic results, whereas the third column present results from the asteroseismological model of this work.

Quantity	Spectroscopy Astrometry	Asteroseismology (This work)
$T_{\text{eff}}$ [kK]	$170 \pm 10^{(a)}$	$163.0^{+2.5}_{-3.7}$
$M_\star$ [ $M_\odot$ ]	$0.716 \pm 0.15$	$0.565^{+0.024}_{-0.023}$
$\log g$ [cm/s <sup>2</sup> ]	$6.0^{+0.3(a)}_{-0.2}$	$6.62^{+0.11}_{-0.07}$
$\log(L_\star/L_\odot)$	$3.95 \pm 0.5^{(b)}$	$3.37 \pm 0.04$
$\log(R_\star/R_\odot)$	...	$-1.21^{+0.046}_{-0.025}$
$M_{\text{env}}$ [ $M_\odot$ ]	...	0.02
$(X_{\text{He}}, X_{\text{C}}, X_{\text{O}})_s$	$0.39, 0.55, 0.06^{(a)}$	$0.39, 0.32, 0.22$
$d$ [pc]	$502.186 \pm 12.554^{(c)}$	$480 \pm 20$
$\pi$ [mas]	$1.991 \pm 0.050^{(c)}$	$2.08 \pm 0.09$

References: (a) Werner & Herwig (2006); (b) Motch et al. (1993); (c) *Gaia*; (d) Appleton et al. (1993).

Next, we describe our period-to-period fit procedure. The merit function  $\chi^2(M_\star, T_{\text{eff}})$  (Eq. 3) was evaluated for stellar masses 0.530, 0.542, 0.565, 0.589, 0.609, 0.664, and 0.741  $M_\odot$ , and for a very wide interval of the effective temperatures (de-

pending on the stellar mass) with a very small step. In our analysis of period-to-period fits, we only considered the central component ( $m = 0$ ) in the case of multiplets. Following the results obtained in Sect. 4.1, for RX J2117 we assume that a subset of 21 periods are associated to  $\ell = 1$  modes — those 20 periods marked with an asterisk in Table 9 along with the period at  $\sim 1557$  s — and leave free the assignment as  $\ell = 1$  or  $\ell = 2$  to the remaining 3 periods. Specifically, we set the value  $\ell = 1$  for all the periods except those at  $\sim 902$  s,  $\sim 1351$  s, and  $1998$  s<sup>8</sup>. We display in Fig. 26 our results. We find only one minimum compatible with the effective temperature of RX J2117 and its uncertainties, corresponding to a PG 1159 model characterized by  $M_\star = 0.565 M_\odot$  and  $T_{\text{eff}} = 162\,992$  K (panel c). There are other minima for other stellar masses, but none of them have an effective temperature compatible with the  $T_{\text{eff}}$  of RX J2117, and they must be discarded.

We adopt the model characterized by  $M_\star = 0.565M_\odot$ ,  $T_{\text{eff}} = 162\,992$  K, and  $\log(L_\star/L_\odot) = 3.373$  as the asteroseismologi-

<sup>8</sup> Note that, on the basis of the analysis made in Sect. 3.1 and Sect. 4.1, we consider the modes with periods 817.375 s, 824.880 s, 966.785 s, 1031.978 s, 1044.041 s, 1131.200 s, and 1976.060 s as  $m \neq 0$  components of rotational multiplets, and thus they are ignored in our period-to-period fits.

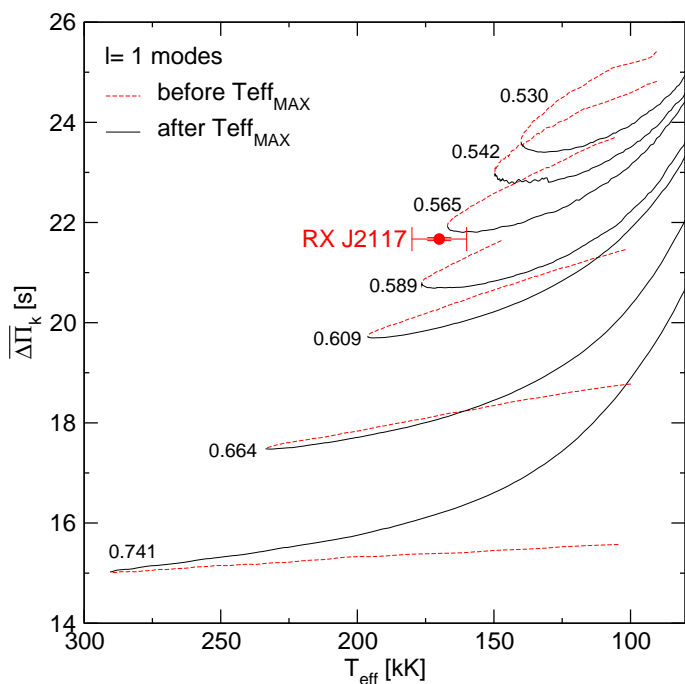


**Fig. 25.** Dipole ( $\ell = 1$ ) average of the computed period spacings,  $\overline{\Delta\Pi}_k$ , assessed in a range of periods that includes the periods observed in RX J2117, shown as solid (dashed) curves corresponding to stages before (after) the maximum  $T_{\text{eff}}$  for different stellar masses. The location of RX J2117 when we use the effective temperature derived by Rauch & Werner (1997),  $T_{\text{eff}} = 170\,000 \pm 10\,000$  K, and the period spacing  $\Delta\Pi = 21.669 \pm 0.030$  s derived in Sect. 4.1 is highlighted with a red circle. We include the error bars associated to the uncertainties in  $\overline{\Delta\Pi}_k$  and  $T_{\text{eff}}$ . The stellar mass derived by interpolation is  $M_{\star} = 0.569 \pm 0.015 M_{\odot}$ .

cal model for RX J2117. Note that this model corresponds to an evolutionary stage just before the star reaches its maximum effective temperature ( $T_{\text{eff,MAX}} = 167\,000$  K). Our results are almost identical to those obtained by the analysis of Córscico et al. (2007a) (asteroseismological model with  $M_{\star} = 0.565 M_{\odot}$  and  $T_{\text{eff}} = 163\,418$  K) which was based on the same PG 1159 stellar models than in the present analysis, but employing the set of periods measured with ground-based observations of Vauclair et al. (2002) alone. In this way, the incorporation of the new periods detected with *TESS* to the analysis seems to strengthen the validity of the results of Córscico et al. (2007a). In Table 14 we show a detailed comparison of the observed periods of RX J2117 and the theoretical  $m = 0$  periods of the asteroseismological model. According to our asteroseismological model, all the  $m = 0$  periods exhibited by RX J2117 correspond to  $\ell = 1$  modes with high radial order  $k$ , except two periods that are associated to  $\ell = 2$  modes. In order to quantitatively assess the quality of our period fit, we compute the average of the absolute period differences,  $\overline{\delta\Pi}_i = (\sum_{i=1}^n |\delta\Pi_i|) / n$ , where  $\delta\Pi_i = (\Pi_{\ell,k} - \Pi_i^o)$  and  $n = 24$ , and the root-mean-square residual,  $\sigma = \sqrt{(\sum_{i=1}^n |\delta\Pi_i|^2) / n} = \sqrt{\chi^2}$ . We obtain  $\overline{\delta\Pi}_i = 1.26$  s and  $\sigma = 1.73$  s. The quality of our fit for RX J2117 is slightly worse than that achieved by Córscico et al. (2007a) ( $\overline{\delta\Pi}_i = 1.08$  s and  $\sigma = 1.34$  s). In order to have a global indicator of the goodness of the period fit that takes into account the number of free parameters, the number of fitted periods, and the proximity between the theoretical and observed periods, we

computed the Bayes Information Criterion (BIC; Koen & Laney 2000):

$$\text{BIC} = n_p \left( \frac{\log N}{N} \right) + \log \sigma^2, \quad (4)$$

where  $n_p$  is the number of free parameters of the models, and  $N$  is the number of observed periods. The smaller the value of BIC, the better the quality of the fit. In our case,  $n_p = 2$  (stellar mass and effective temperature),  $N = 24$ , and  $\sigma = 1.73$  s. We obtain  $\text{BIC} = 0.59$ , which means that our period fit is excellent.

We also include in Table 14 the rates of period change ( $\dot{\Pi} \equiv d\Pi/dt$ ) predicted for each  $g$  mode of RX J2117. Note that all of them are negative ( $\dot{\Pi} < 0$ ), implying that the periods are shortening over time. The rate of change of periods in WDs and pre-WDs is related to  $\dot{T}$  ( $T$  being the temperature at the region of the period formation) and  $\dot{R}_{\star}$  ( $R_{\star}$  being the stellar radius) through the order-of-magnitude expression ( $\dot{\Pi}/\Pi \approx -a(\dot{T}/T) + b(\dot{R}_{\star}/R_{\star})$ ) (Winget et al. 1983). According to our asteroseismological model, the star is heating and contracting before reaching its maximum temperature (evolutionary knee) and entering its cooling stage. As a consequence,  $\dot{T} > 0$  and  $\dot{R}_{\star} < 0$ , and then,  $\dot{\Pi} < 0$ . As shown in Fig. 11 of Sect. 4.1, RX J2117 exhibits irregular variations of periods on different time scales. So, a comparison of our theoretical predictions with the observational trends is not possible at this time.

Table 14 also gives information about the pulsational stability/instability nature of the modes associated with the periods fitted to the observed ones (ninth column). In particular, we examine the sign of the computed linear nonadiabatic growth rates ( $\eta_k$ ). A positive value of  $\eta_k$  means that the mode is linearly unstable. Interestingly, the interval of periods corresponding to unstable modes of our asteroseismological model is almost coincident with the range of excited periods in RX J2117, except in the case of the shortest periods (692.267 s, 712.975 s, and 733.948 s) and the longest periods (1350.870 s, 1557.010 s, and 1997.760 s) exhibited by the star, which are not predicted to be unstable by our theoretical calculations ( $\eta_k < 0$ ). This is because, for  $T_{\text{eff}} = 163\,000$  K, the model sequence of  $M_{\star} = 0.565 M_{\odot}$  has unstable  $\ell = 1$  ( $\ell = 2$ ) periods in the range 777 s – 1181 s (416 s – 938 s) (Córscico et al. 2006).

In Table 15, we list the main characteristics of the asteroseismological model for RX J2117. The seismological stellar mass ( $0.565 M_{\odot}$ ) is in excellent agreement with the value derived from the period spacing ( $0.569 M_{\odot}$ ). The average of the dipole ( $\ell = 1$ ) period spacings of our asteroseismological model is  $\overline{\Delta\Pi} = 22.153$  s and the asymptotic period spacing is  $\Delta\Pi^a = 22.064$  s, in excellent agreement with the  $\ell = 1$  mean period spacing derived for RX J2117 in Sect. 4.1 ( $\Delta\Pi = 21.669 \pm 0.030$  s). The luminosity of the asteroseismological model,  $\log(L_{\star}/L_{\odot}) = 3.37$  is lower than the luminosity inferred by Motch et al. (1993),  $\log(L_{\star}/L_{\odot}) = 3.95$ , based on the evolutionary tracks of Wood & Faulkner (1986).

The asteroseismological distance can be computed as in Córscico et al. (2007a). On the basis of the luminosity of the asteroseismological model ( $\log(L_{\star}/L_{\odot}) = 3.37 \pm 0.04$ ) and the bolometric correction given by a NLTE model atmosphere with  $T_{\text{eff}} = 160$  kK and  $\log g = 6.6$  computed with the Tübingen Model Atmosphere Package ( $BC = -7.954$ ; see Werner et al. 2003; Córscico et al. 2007a, for details), the absolute magnitude can be assessed as  $M_V = M_B - BC$ , where  $M_B = M_{B,\odot} - 2.5 \log(L_{\star}/L_{\odot})$ . We employ the solar bolometric magnitude  $M_{B,\odot} = 4.74$  (Cox 2000). The seismological distance  $d$  is derived from the relation:  $\log d = 15 [m_V - M_V + 5 - A_V(d)]$ ,

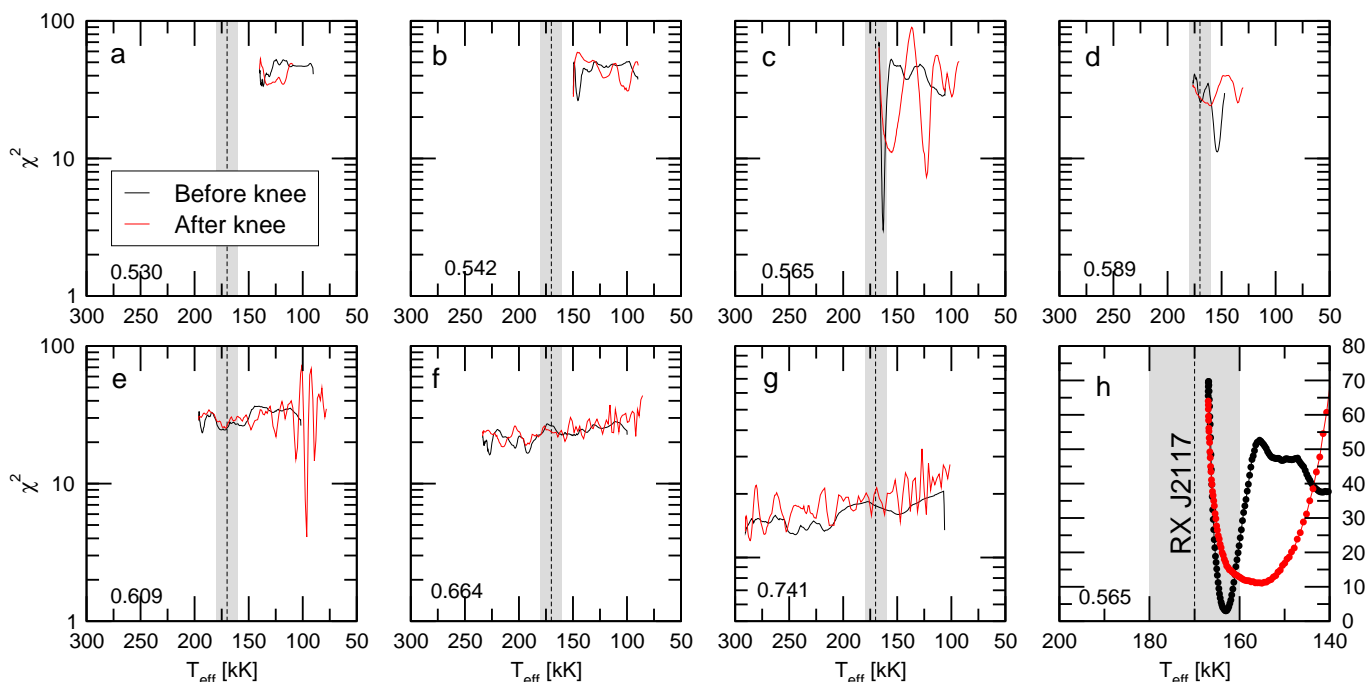


**Fig. 26.** The quality function of the period fit in terms of the effective temperature for the PG 1159 sequences with different stellar masses (in solar units), indicated at the left-bottom corner of each panel. Black (red) lines correspond to stages before (after) the evolutionary knee (see Fig. 1). Only the periods with  $m = 0$  (see Table 9) have been considered. Note the strong minimum in panel c, corresponding to  $M_{\star} = 0.565M_{\odot}$ . Panel h is a zoom of the region with the strong minimum seen in panel c; the y-axis scale is linear in this case. The vertical dashed line is the spectroscopic  $T_{\text{eff}}$  of RX J2117 (170 kK) and the gray zone depicts its uncertainties ( $\pm 10$  kK).

where we employ the interstellar extinction law of Chen et al. (1998). The interstellar absorption  $A_V(d)$  is a nonlinear function of the distance and also depends on the Galactic latitude ( $b$ ). For the equatorial coordinates of RX J2117 (Epoch B2000.00,  $\alpha = 21^{\text{h}}17^{\text{m}}8.^{\text{s}}2$ ,  $\delta = +34^{\circ}12'27.''58$ ) the corresponding Galactic latitude is  $b = -10^{\circ}24'32.''04$ . We use the apparent visual magnitude  $m_V = 13.16 \pm 0.01$  (Motch et al. 1993), and obtain the seismological distance and parallax  $d = 480 \pm 20$  pc and  $\pi = 2.08 \pm 0.09$  mas, respectively, being the extinction coefficient  $A_V = 0.47 \pm 0.02$ . The uncertainty in the seismological distance comes mainly from the uncertainty in the luminosity of the asteroseismological model, which is admittedly very small ( $\Delta \log(L_{\star}/L_{\odot}) = 0.04$ ) because this is solely attributed to internal errors, i.e., uncertainties typical of the period-fit procedure. Realistic estimates of these errors (due to uncertainties in stellar modeling and the pulsation computations) are probably much higher. A very important check for the validation of the asteroseismological model for RX J2117 is the comparison of the seismological distance with the distance derived from astrometry. We have available the estimates from *Gaia*,  $d_G = 502 \pm 12$  pc and  $\pi_G = 1.991 \pm 0.05$  mas. They are in excellent agreement with the asteroseismological derivations in view of the uncertainties in both determinations.

We close this section summarizing our findings for RX J2117. The seismological stellar mass derived from the period spacing is in excellent agreement with the stellar mass of the asteroseismological model — derived through a fit to the individual periods — and in line with what was found by Vauclair et al. (2002) and Córscico et al. (2007a). On the other hand, a seismological mass in the range  $0.560 - 0.569M_{\odot}$  apparently disagrees with the spectroscopic mass, of  $0.716 \pm 0.15M_{\odot}$ , but nevertheless they are still compatible each other, given the uncertainties in both determinations — particularly in the spectroscopic mass. On the other hand, the seismological distance derived from the

asteroseismological model is in excellent agreement with the distance measured by *Gaia*.

## 7.2. HS 2324

In Fig. 27 we show  $\ell = 1 \overline{\Delta \Pi}_k$  as a function of  $T_{\text{eff}}$  for all the masses considered. Note that these curves are slightly different as compared with those of Fig. 25 that correspond to RX J2117. This is because the averages of the computed period spacings are calculated considering different ranges of periods for different stars. The period spacing of HS 2324 is  $\Delta \Pi = 16.407 \pm 0.062$  s, as derived in Sect. 3.2. In this case, we considered two possibilities, that the star is before or after the maximum effective temperature, that is, the “evolutionary knee” (see Fig. 1). This is because we do not know, in principle, the evolutionary stage in which the star is. We find  $M_{\star} = 0.727 \pm 0.017M_{\odot}$  if the star is before the maximum  $T_{\text{eff}}$ , and  $M_{\star} = 0.758 \pm 0.018M_{\odot}$  if the star is after the maximum  $T_{\text{eff}}$ . These values are much larger than the spectroscopic mass derived in Sect. 5, of  $M_{\star} = 0.532 \pm 0.150M_{\odot}$ .

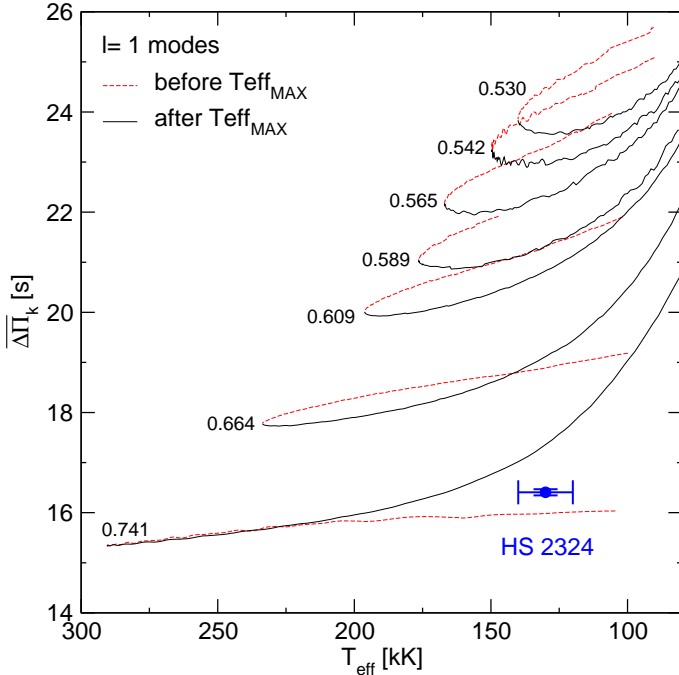
Next, we describe our period-to-period fit analysis for HS 2324. Again, the merit function  $\chi^2(M_{\star}, T_{\text{eff}})$  (Eq. 3) was evaluated for all the stellar masses and effective temperatures covered by our PG 1159 model sequences. We employed the 21 periods of Table 10. We adopted the same approach as for the case of RX J2117, that is, we assumed that there is a subset of 13 periods identified as  $\ell = 1$  according to the period spacing derived in Sect. 4.2 (see Table 10), but the remaining 8 periods are allowed to be identified with modes with dipole or quadrupole modes.

Given the absence of a single global minimum in the quality function when evaluated for all the stellar masses and effective temperatures considered, we were forced to analyze what happens in the range of effective temperatures published for HS 2324, that is  $120\,000 \lesssim T_{\text{eff}} \lesssim 140\,000$  K. We display in



**Table 16.** Observed and theoretical periods of the asteroseismological model for HS 2324 [ $M_\star = 0.664M_\odot$ ,  $T_{\text{eff}} = 138\,572$  K,  $\log(L_\star/L_\odot) = 4.069$ ]. The columns have the same meaning as in Table 14.

$\Pi_i^O$ (s)	$\ell^O$	$\Pi_k$ (s)	$\ell$	$k$	$\delta\Pi_k$ (s)	$\dot{\Pi}_k$ ( $10^{-11}$ s/s)	Unstable
1039.020	?	1038.518	2	101	0.502	-48.352	no
1047.100	1	1051.555	1	59	-4.455	21.631	no
1049.877	?	1048.216	2	102	1.661	-65.542	no
2005.780	?	2006.376	1	113	-0.596	-18.035	yes
2027.520	?	2024.919	2	197	2.601	-43.713	yes
2029.350	1	2022.871	1	114	6.479	-8.498	yes
2047.260	1	2041.419	1	115	5.841	-15.661	yes
2059.970	1	2060.657	1	116	-0.687	-47.391	yes
2076.110	?	2078.013	2	202	-1.903	-84.734	yes
2078.590	1	2078.239	1	117	0.351	-93.688	yes
2095.046	1	2093.885	1	118	1.161	-132.285	yes
2098.670	?	2098.804	2	204	-0.134	-73.882	yes
2110.152	1	2110.330	1	119	-0.178	-137.956	yes
2160.970	1	2164.402	1	122	-3.432	-19.931	yes
2170.490	?	2172.624	2	211	-2.134	-88.824	yes
2175.290	1	2181.536	1	123	-6.246	-20.287	yes
2193.420	1	2199.885	1	124	-6.465	-52.300	yes
2202.990	?	2203.977	2	214	-0.987	-55.166	yes
2553.230	1	2553.519	1	144	-0.289	-128.112	yes
2568.860	1	2571.257	1	145	-2.397	-78.122	yes
2682.050	1	2677.444	1	151	4.606	-134.986	yes


**Fig. 27.** Dipole ( $\ell = 1$ ) average of the computed period spacings,  $\Delta\Pi_k$ , assessed in a range of periods that includes the periods observed in HS 2324, shown as solid (dashed) curves corresponding to stages before (after) the maximum  $T_{\text{eff}}$  for different stellar masses. The location of HS 2324 when we use the effective temperature derived by Dreizler et al. (1996),  $T_{\text{eff}} = 130\,000 \pm 10\,000$  K, and the period spacing  $\Delta\Pi = 16.407 \pm 0.062$  s derived in Sect. 3.2 is highlighted with a blue circle. The stellar mass derived from linear interpolation is  $M_\star = 0.727 \pm 0.017M_\odot$  if the star is before the maximum  $T_{\text{eff}}$ , and by linear extrapolation, it is  $M_\star = 0.758 \pm 0.018M_\odot$  if the star is after the maximum  $T_{\text{eff}}$ .

**Table 17.** The main characteristics of the GW Vir star HS 2324. The second column corresponds to spectroscopic results, whereas the third column present results from the asteroseismological model of this work.

Quantity	Spectroscopy Astrometry	Asteroseismology (This work)
$T_{\text{eff}}$ [kK]	$130 \pm 10^{(a)}$	$138.6^{+3.0}_{-2.8}$
$M_\star$ [ $M_\odot$ ]	$0.532 \pm 0.150$	$0.664^{+0.077}_{-0.055}$
$\log g$ [ $\text{cm/s}^2$ ]	$6.2 \pm 0.2^{(a)}$	$5.72^{+0.13}_{-0.10}$
$\log(L_\star/L_\odot)$	...	$4.07^{+0.18}_{-0.21}$
$\log(R_\star/R_\odot)$	...	$-0.73^{+0.06}_{-0.08}$
$M_{\text{env}}$ [ $M_\odot$ ]	...	0.02
$(X_H, X_{\text{He}}, X_C, X_O)_s$	0.17, 0.35, 0.42, 0.06 <sup>(a)</sup>	0.00, 0.47, 0.33, 0.13
$d$ [pc]	$1448.033 \pm 105.266^{(b)}$	$4379^{+1009}_{-940}$
$\pi$ [mas]	$0.691 \pm 0.0502^{(b)}$	$0.228^{+0.063}_{-0.042}$

 References: (a) Werner & Herwig (2006); (b) *Gaia* DR2.

Fig. 28 our results. We note the existence of a clear minimum for a model with  $M_\star = 0.664M_\odot$  and  $T_{\text{eff}} = 138\,572$  K. It is located at the stages previous to the maximum temperature for this mass. We adopt this model as the asteroseismological model for HS 2324. In Table 16 we show a detailed comparison of the observed periods of HS 2324 and the theoretical periods of the asteroseismological model. For this asteroseismological solution, we have  $\delta\Pi_i = 2.53$  s and  $\sigma = 3.36$  s. The quality of our fit for HS 2324 is worst than that achieved for RX J2117 ( $\delta\Pi_i = 1.26$  s and  $\sigma = 1.73$  s). We also computed the Bayes Information Criterion. In this case,  $N_p = 2$  (stellar mass and effective temperature),  $n = 21$ , and  $\sigma = 3.36$  s. We obtain BIC = 1.18, which means that our fit is not as good as for RX J2117 (BIC = 0.59), but still satisfactory.

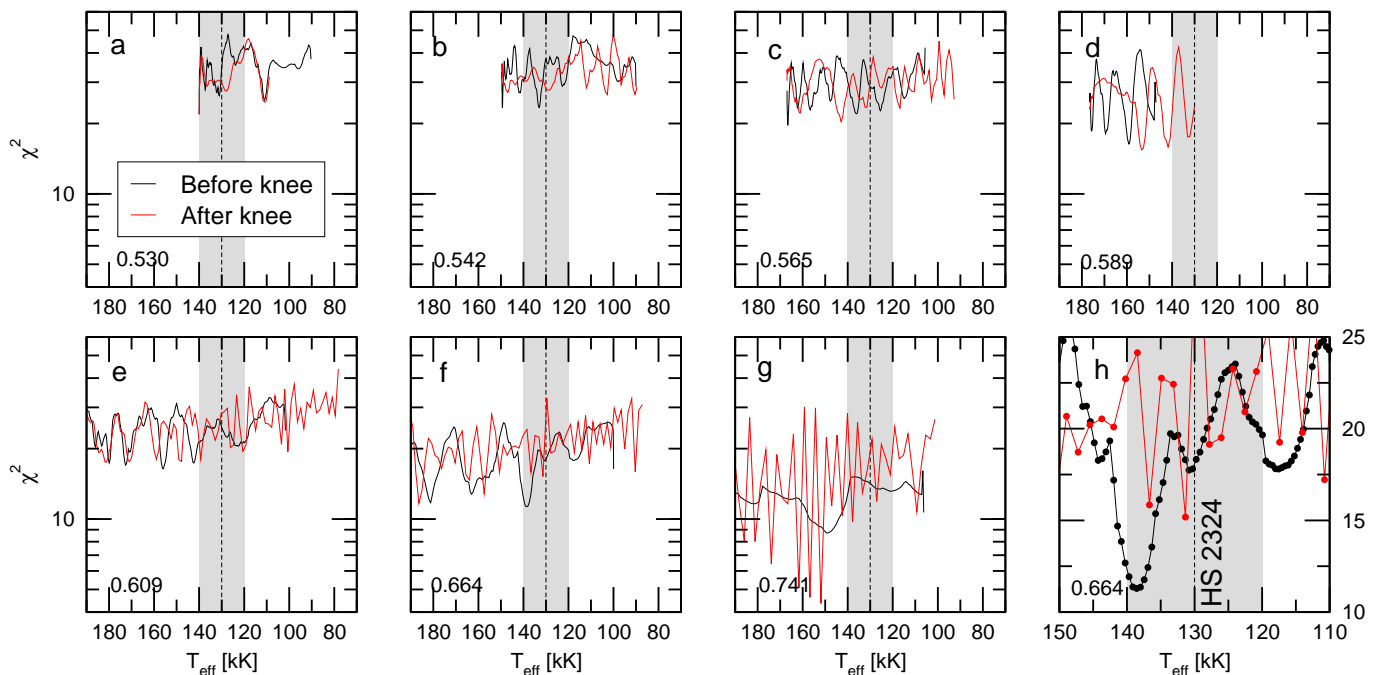


**Fig. 28.** Same as Fig. 26, but for HS 2324. Note the minimum in panel **f** before the evolutionary knee (black curve), corresponding to  $M_{\star} = 0.664M_{\odot}$ . Panel **h** is a zoom of the region with the strong minimum seen in panel **f**; the y-axis scale is linear in this case. The vertical dashed line is the spectroscopic  $T_{\text{eff}}$  of HS 2324 (130 kK) and the gray zone depicts its quoted uncertainty ( $\pm 10$  kK).

According to our seismological model, the values of the rate of period change for the  $g$  modes of HS 2324 (column 7 of Table 16) are  $\sim 10 - 100$  times greater than for the asteroseismological model of RX J2117 (Table 14). This is because the asteroseismological model of HS 2324 ( $M_{\star} = 0.664M_{\odot}$ ) is more massive than the asteroseismological model of RX J2117 ( $M_{\star} = 0.565M_{\odot}$ ), and the evolution through the PG 1159 stage proceeds considerably faster for massive stars (Miller Bertolami & Althaus 2006). In Sect. 4.2 we called the attention of a possible physical change of the period at  $\sim 2193$  s from 1999 to 2020, with a negative derivative and a magnitude of  $\sim 10^{-9}$  s/s. This value is compatible with the theoretical rate of change for this period, of  $-0.523 \times 10^{-9}$  s/s (Table 16).

Column 8 of Table 16 shows that most of the periods of the asteroseismological model that fit the observed periods are predicted to be unstable ( $\eta_k > 0$ ), except for the three periods shorter than  $\sim 2000$  s, for which our nonadiabatic computations indicate pulsational stability. For  $T_{\text{eff}} = 138\,600$  K, the model sequence of  $M_{\star} = 0.664M_{\odot}$  has unstable dipole (quadrupole) periods in the range 2028 s – 465 s (1215 s – 3095 s) (Córscico et al. 2006)<sup>9</sup>.

In Table 17, we list the main characteristics of the asteroseismological model for HS 2324. The stellar mass of the seismological model ( $0.664M_{\odot}$ ) is  $\sim 10\%$  smaller than — although still compatible with — the value derived from the period spacing ( $\sim 0.73M_{\odot}$ ), assuming that the star is before the evolutionary knee. This mass discrepancy is reflected in the fact that dipole ( $\ell = 1$ ) mean period spacing of our asteroseismological model ( $\overline{\Delta\Pi} = 18.81$  s) is  $\sim 14\%$  longer than the  $\ell = 1$  mean period spacing derived for HS 2324 in Sect. 4.2 ( $\Delta\Pi = 16.407 \pm 0.062$  s). Given the error ranges of the spectro-

scopic mass ( $0.532 \pm 0.150 M_{\odot}$ , Sect. 5) and the asteroseismic mass determinations, they are compatible each other.

We can compute the asteroseismological distance of HS 2324, as we did for RX J2117. We employ the luminosity of the asteroseismological model of HS 2324,  $\log(L_{\star}/L_{\odot}) = 4.07^{+0.18}_{-0.21}$ , a bolometric correction of  $BC = -7.24$  (extrapolated from the value corresponding to PG 1159–035 as given by Kawaler & Bradley 1994), and the interstellar extinction law of Chen et al. (1998). For the equatorial coordinates of HS 2324 (Epoch B2000.00,  $\alpha = 23^{\text{h}}27^{\text{m}}15.^{\text{s}}95$ ,  $\delta = +40^{\circ}01'23.''63$ ) the corresponding Galactic latitude is  $b = -20^{\circ}3'0.''86$ . We adopt  $m_V = 15.41$  (Faedi et al. 2011) and obtain a seismological distance, a parallax, and an extinction coefficient of  $d = 4379^{+1009}_{-940}$  pc,  $\pi = 0.228^{+0.063}_{-0.042}$  mas, and  $A_V = 0.398$ , respectively. On the other hand, the values measured by *Gaia* are  $d_G = 1448 \pm 105$  pc and  $\pi_G = 0.691 \pm 0.050$  mas, in line with the distance inferred by Dreizler et al. (1996) (1500 pc). At variance with the case of RX J2117, for HS 2324 there is a serious disagreement between our asteroseismological distance and the distance obtained with *Gaia*. This discrepancy must be largely attributed to the high luminosity of our seismological model. In this sense, the uncertainty of the luminosity of the seismological model ( $\Delta \log(L_{\star}/L_{\odot}) \sim 0.2$ ) is just formal and it is probably underestimated, since it reflects only internal errors of the period-fit processes. Thus, a compatibility between the seismological distance and the astrometric distance from *Gaia* would be achieved if we could employ a more realistic estimate of the uncertainties in the luminosity of the asteroseismological model.

We end this section summarizing our results for HS 2324. The stellar mass inferred from the period separation ( $\sim 0.73M_{\odot}$ ) is in line with the mass of the seismological model ( $\sim 0.66M_{\odot}$ ), and still compatible with the spectroscopic mass, of  $0.532 \pm 0.15M_{\odot}$ , given the large uncertainties in the parameters with which the spectroscopic mass is determined — in particular the  $\log g$  value.

<sup>9</sup> Note that the nonadiabatic pulsation calculations of Córscico et al. (2006) correspond to PG 1159 models without H in the envelopes, which is not strictly the case of a hybrid GW Vir star, which has some H on its surface. However, we do not expect the results of the pulsation analysis to be appreciably modified by the presence of a trace of H.

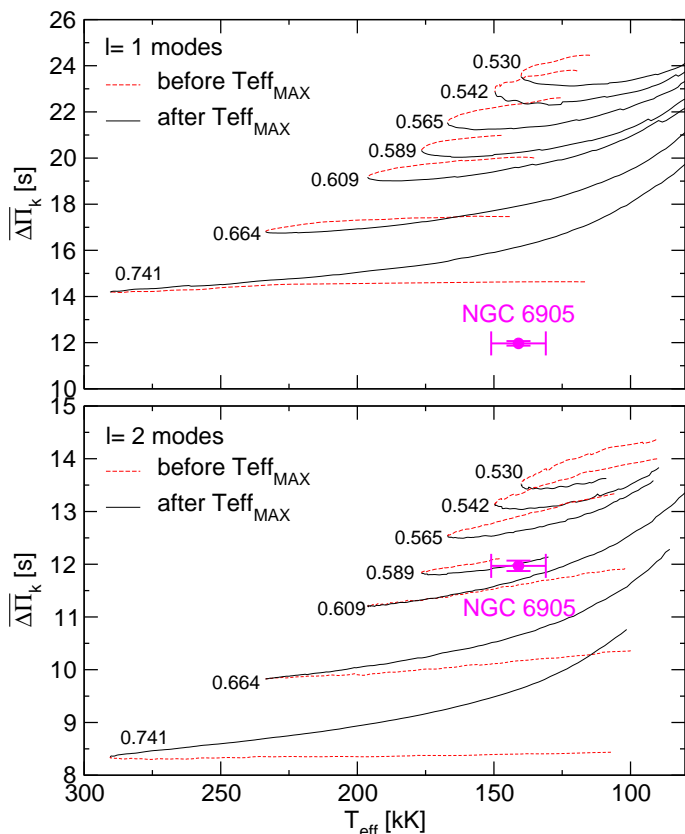


**Fig. 29.** Upper panel: dipole ( $\ell = 1$ ) average of the computed period spacings,  $\overline{\Delta\Pi}_k$ , assessed in a range of periods that includes the periods observed in NGC 6905, shown as solid (dashed) curves corresponding to stages before (after) the maximum  $T_{\text{eff}}$  for different stellar masses. The location of NGC 6905 when we use the effective temperature derived by Ciardullo & Bond (1996),  $T_{\text{eff}} = 141\,000 \pm 10\,000$  K, and the period spacing  $\Delta\Pi = 11.9693 \pm 0.0988$  s derived in Sect. 3.3 and assumed to be associated to  $\ell = 1$  modes, is highlighted with a magenta circle. The stellar mass derived from linear extrapolation is  $M_{\star} \sim 0.818M_{\odot}$  if the star is before the maximum  $T_{\text{eff}}$ , and it is  $M_{\star} \sim 0.861M_{\odot}$  if the star is after the maximum  $T_{\text{eff}}$ . Lower panel: same as in upper panel, but for the case in which the period spacing is assumed to be associated to  $\ell = 2$  modes ( $\Delta\Pi = 11.9693 \pm 0.0988$  s). In this case, the stellar mass is  $M_{\star} = 0.596 \pm 0.09M_{\odot}$  and  $M_{\star} = 0.590 \pm 0.007M_{\odot}$  if the star is before or after the evolutionary knee, respectively.

### 7.3. NGC 6905

In the upper panel of Fig. 29 we display the run of the dipole  $\overline{\Delta\Pi}_k$  in terms of  $T_{\text{eff}}$  for all the masses considered, for the case of NGC 6905. We assume the period spacing  $\Delta\Pi = 11.9693 \pm 0.0988$  s to be associated to  $\ell = 1$  modes. This period spacing results from considering the periods of modes detected with *TESS*, in addition to the periods from Ciardullo & Bond (1996) (Table 11 of Sect. 4.3). As in the case of HS 2324, for NGC 6905 we considered two possibilities: the star is before or after the “evolutionary knee”. We find  $M_{\star} \sim 0.818$  if the star is before the maximum  $T_{\text{eff}}$ , and  $M_{\star} \sim 0.811M_{\odot}$  if the star is after the maximum  $T_{\text{eff}}$ . Note that these values are obtained by extrapolation, because the period spacing of the star, being only about 12 s, is well below the average of the computed spacing curves of our models, even the most massive one ( $M_{\star} = 0.741M_{\odot}$ ). Therefore, our stellar mass values are just *estimates*. The stellar mass of NGC 6905 according to these estimates is much higher than

the spectroscopic mass of this star, of  $M_{\star} = 0.590 \pm 0.150 M_{\odot}$ , as derived in Sect. 5.

We also explored the possible situation in which the period spacing of  $\Delta\Pi = 11.9693 \pm 0.0988$  s correspond to  $\ell = 2$  modes. We then compared this period spacing with the quadrupole  $\overline{\Delta\Pi}_k$  in terms of  $T_{\text{eff}}$  for all the masses considered, as shown in the lower panel of Fig. 29. In this case, the mass value is of  $M_{\star} = 0.596 \pm 0.09M_{\odot}$  and  $M_{\star} = 0.590 \pm 0.007M_{\odot}$  if the star is before or after the evolutionary knee, respectively. These values are in excellent agreement with the spectroscopic mass value ( $M_{\star} = 0.59M_{\odot}$ ).

We attempted a period-to-period fit for NGC 6905 using the individual periods of Table 11. We adopted the same approach as for the case of RX J2117 and HS 2324, i.e., we assumed that there is a subset of periods identified as  $\ell = 1$  according to the period spacing derived in Sect. 4.3 (see Table 11), but the remaining periods are allowed to be associated with dipole or quadrupole modes as well. Note that there are two possibilities with respect to the period  $\sim 816$  s. Although unlikely, one possibility would be to consider that it is a component  $\ell = 1$ ,  $m = \pm 1$  of a rotational triplet, in which case, we can ignore this period in our period-fit process and there are 10 observed periods available. The other possibility would be to consider it as a  $\ell = 2$ ,  $m = 0$  mode, and therefore incorporate it into the analysis. In this case the period-to-period fit is carried out on a set of 11 periods. The results of our procedure with 10 and with 11 periods are very similar, and do not indicate a very clear asteroseismological model regarding the uniqueness of the solutions. Specifically, there are several possible solutions in terms of period match within the effective-temperature range of interest (131 000 – 151 000 K) for NGC 6905. However, most of the possible solutions (minima in the quality function) correspond to stages after the evolutionary knee. If we accept that NGC 6905 is evolving towards the blue, before reaching its maximum effective temperature — as indicated by its position in the  $\log T_{\text{eff}} - \log g$  diagram; see Fig. 1 — then we do not find any clear minima in the quality function, making virtually impossible to isolate a clear and unambiguous seismological solution<sup>10</sup>. Thus, for NGC 6905 we are unable to find an asteroseismological model. The harmonic degree of the mode with period  $\sim 816$  s remains undetermined, although according to our calculations, the period fits slightly improve when we consider that this corresponds to  $\ell = 2$ .

We also considered the possibility that the period spacing derived in Sect. 4.3 corresponds to modes  $\ell = 2$ . In this case, in Table 11 the modes identified as  $\ell = 1$  are now identified as  $\ell = 2$ . In total, we have available 7 quadrupole modes and 4 modes that can be alternatively dipole or quadrupole. We assume that the mode with period  $\sim 816$  s can correspond to a  $\ell = 1$  mode or a  $\ell = 2$  mode as well. We have repeated the period-fit procedure with this identification of modes, but unfortunately we have not found a satisfactory seismological solution. In particular, it is very difficult to fit the observed periods at 816.3 s, 851.4 s, 874.8 s, 884 s with  $\ell = 1$  or  $\ell = 2$  theoretical periods, if we assume that the rest of the observed periods correspond to  $\ell = 2$  modes.

<sup>10</sup> We still could pick out a possible seismological solution consisting of a pre-WD model with a stellar mass  $M_{\star} = 0.664M_{\odot}$  and an effective temperature  $T_{\text{eff}} = 145\,400$  K. However, the match between the theoretical and observed periods is very poor, with differences of up to  $\sim 10$  s, something that is reflected by the high value of the local minimum in the quality function for that model ( $\chi^2 = 16.05$  s<sup>2</sup>).

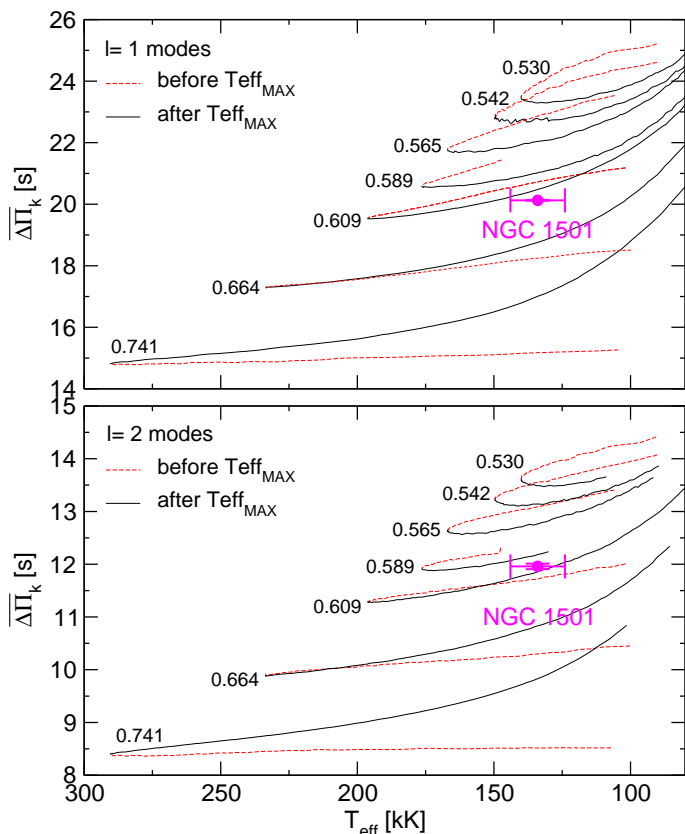


**Fig. 30.** Upper panel: dipole ( $\ell = 1$ ) average of the computed period spacings,  $\overline{\Delta\Pi}_k$ , assessed in a range of periods that includes the periods observed in NGC 1501, shown as solid (dashed) curves corresponding to stages before (after) the maximum  $T_{\text{eff}}$  for different stellar masses. The location of NGC 1501 when we use the effective temperature derived by Werner & Herwig (2006),  $T_{\text{eff}} = 134\,000 \pm 10\,000$  K, and the dipole period spacing,  $\overline{\Delta\Pi}_{\ell=1} = 20.1262 \pm 0.0123$  s (derived in Sect. 3.4), is highlighted with a magenta circle. The stellar mass derived from linear interpolation is  $M_{\star} = 0.621 \pm 0.015 M_{\odot}$  if the star is before the maximum  $T_{\text{eff}}$ , and it is  $M_{\star} = 0.624 \pm 0.015 M_{\odot}$  if the star is after the maximum  $T_{\text{eff}}$ . Lower panel: same as in upper panel, but for the case of  $\ell = 2$  modes ( $\overline{\Delta\Pi}_{\ell=2} = 11.9593 \pm 0.0520$  s). In this case, the stellar mass is  $M_{\star} = 0.601 \pm 0.015 M_{\odot}$  and  $M_{\star} = 0.606 \pm 0.015 M_{\odot}$ , according to the star is before or after the maximum  $T_{\text{eff}}$ .

#### 7.4. NGC 1501

We calculated the  $\ell = 1$  and  $\ell = 2$  averages of the computed period spacings for the case of NGC 1501. The curves of  $\overline{\Delta\Pi}_k$  in terms of  $T_{\text{eff}}$  for all the masses considered are shown in the upper ( $\ell = 1$ ) and lower ( $\ell = 2$ ) panels of Fig. 30. According to the analysis of Sect. 4.4, the dipole period spacing of NGC 1501 is  $\overline{\Delta\Pi}_{\ell=1} = 20.1262 \pm 0.0123$  s, and the quadrupole period spacing is  $\overline{\Delta\Pi}_{\ell=2} = 11.9593 \pm 0.0520$  s. As in the case of HS 2324 and NGC 6905, for NGC 1501 we considered the two possibilities, i.e., that the object is before or after the “evolutionary knee”. From the  $\ell = 1$  periods, we find  $M_{\star} = 0.621 \pm 0.015 M_{\odot}$  if the star is before the evolutionary knee, and  $M_{\star} = 0.624 \pm 0.015 M_{\odot}$  if the star is after the evolutionary knee. On the other hand, from the  $\ell = 2$  periods we derive  $M_{\star} = 0.601 \pm 0.015 M_{\odot}$  and  $M_{\star} = 0.606 \pm 0.015 M_{\odot}$  depending on the star being before or after the evolutionary knee. These mass values of NGC 1501, which are in the range  $\sim 0.60 - 0.62 M_{\odot}$ , are  $\sim 5 - 10\%$  larger than — but still compatible with — the spectroscopic mass of this star ( $M_{\star} = 0.565 \pm 0.150 M_{\odot}$ ; see Sect. 5).

As for the other target stars analyzed in this study, we have performed a period-to-period fit for NGC 1501. We employed the periods of Table 12, except the periods 1318.46 s and 1999.16 s which do not fit neither the  $\ell = 1$  nor the  $\ell = 2$  series of periods with constant period spacings. We assumed that there is a subset of 14 periods corresponding to  $\ell = 1$  modes, and 10 periods identified with  $\ell = 2$  modes, according to the period spacings derived in Sect. 4.4 (see Table 12). We display in Fig. 31 our results for this analysis. We note the existence of a clear minimum for the model with  $M_{\star} = 0.609 M_{\odot}$  and  $T_{\text{eff}} = 140\,051$  K. It is located at the stages previous to the maximum temperature for this mass. The value of the quality function for this solution is  $\chi^2 = 10.76$  s<sup>2</sup>. We adopt this model as the asteroseismological model for NGC 1501. In Table 18 we show a detailed comparison of the observed periods of NGC 1501 and the theoretical periods of the asteroseismological model. For this asteroseismological solution, we have  $\overline{\delta\Pi}_i = 2.81$  s and  $\sigma = 3.28$  s. The quality of our fit for NGC 1501 is worse than that achieved for RX J2117 ( $\overline{\delta\Pi}_i = 1.26$  s and  $\sigma = 1.73$  s), but comparable to that obtained for HS 2324 ( $\overline{\delta\Pi}_i = 2.53$  s and  $\sigma = 3.36$  s). We also computed the Bayes Information Criterion. In this case,  $N_p = 2$  (stellar mass and effective temperature),  $n = 24$ , and  $\sigma = 3.28$  s. We obtain BIC = 1.15, which means that our fit is not so good as for RX J2117 (BIC = 0.59), but very similar to that of HS 2324 (BIC = 1.18), and still satisfactory. We have redone the analysis by fixing the harmonic degree of the 14 periods labeled as  $\ell = 1$  at the outset, but allowing the other 10 periods to be associated with  $\ell = 1$  or  $\ell = 2$  modes. Also, we repeated the above analysis by incorporating the two periods excluded into the period fit (1318.46 s and 1999.16 s), allowing them to be associated to  $\ell = 1$  or  $\ell = 2$  modes. In both realizations, we obtained the same asteroseismological solution than before ( $M_{\star} = 0.609 M_{\odot}$  and  $T_{\text{eff}} = 140\,051$  K), and with similar values of the quality function. The fact that we arrive at the same seismological solution for NGC 1501 implies that the period-fit process automatically assigns the observed periods that we had originally assumed to be associated with quadrupole modes (following the strong constraint imposed by the period spacing; see Table 12) to theoretical modes with  $\ell = 2$ . This adds robustness to the identification of the harmonic degree of modes made in Sect. 4.4.

The secular rates of period change for NGC 1501, as predicted by our seismological model, are shown in column 7 of Table 18. All the values are negative, reflecting the fact that the star would be evolving towards high temperatures and rapidly contracting, which shortens the periods of  $g$  modes with time. The rates of period change are in the range  $(10 - 160) \times 10^{-11}$  s/s, being similar to those of the asteroseismological model of HS 2324 (Table 16), and two orders of magnitude higher than those of the asteroseismological model of RX J2117 (Table 14).

We include in the column 8 of Table 18 the information about the stability/instability of the modes of the asteroseismological model. Strikingly, all quadrupole modes are predicted to be unstable ( $\eta_k > 0$ ), while most dipole modes are predicted to be stable ( $\eta_k < 0$ ). This is because the model sequence of  $M_{\star} = 0.609 M_{\odot}$  has unstable dipole (quadrupole) periods in the range 1817 s – 4228 s (1077 s – 3041 s) (Córscico et al. 2006). Therefore, unlike the previous targets, the stability calculations of the modes with  $\ell = 1$  do not favor the validity of the seismological model for NGC 1501. However, we mention that stability properties of the  $g$  modes in these stars strongly depend on the envelope composition (Quirion et al. 2007), which is affected by the treatment of convective boundary mixing during the born again episode. Thus, with a readjustment of the abundances of O,

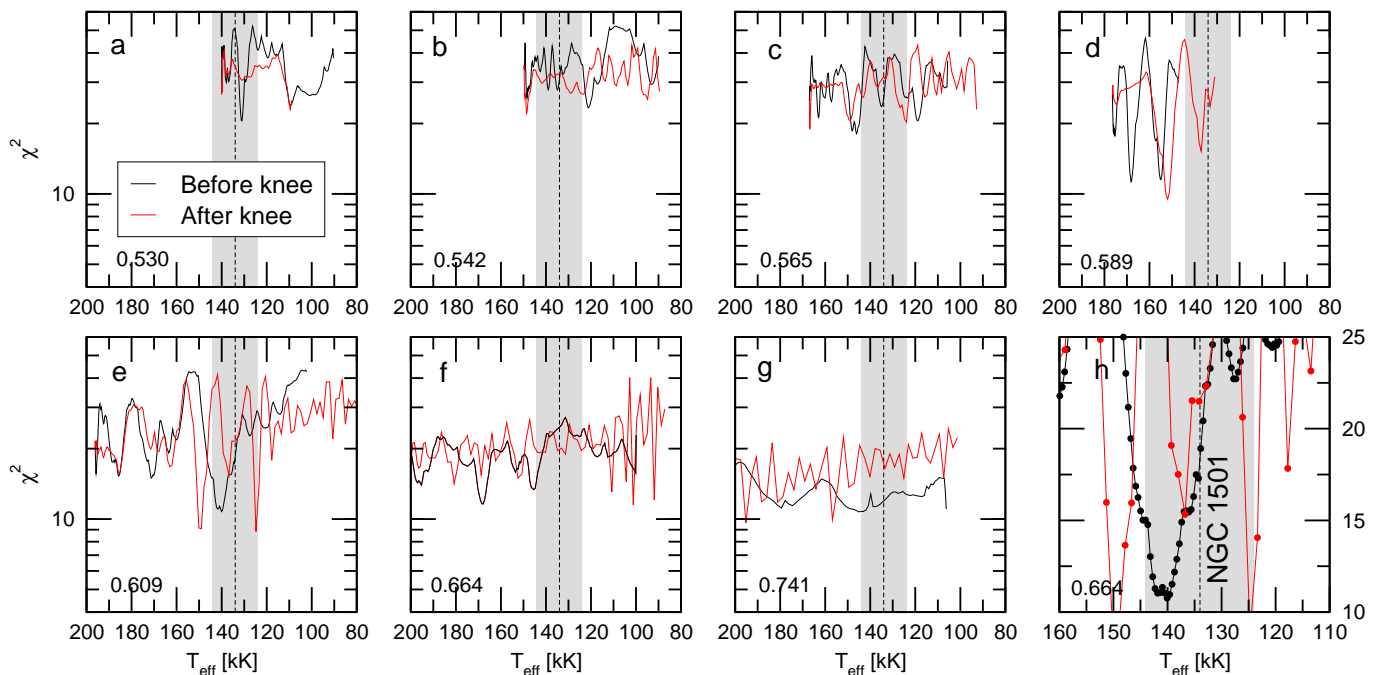


**Fig. 31.** Same as Fig. 26, but for NGC 1501. Note the minimum in panel **e** before the evolutionary knee (black curve), corresponding to  $M_{\star} = 0.609M_{\odot}$ . Panel **h** is a zoom of the region with the strong minimum seen in panel **e**; the y-axis scale is linear in this case. The vertical dashed line is the spectroscopic  $T_{\text{eff}}$  of NGC 1501 (134 kK) and the gray zone depicts its uncertainties ( $\pm 10$  kK).

C and He we do not rule out that an agreement could be found between the observed  $\ell = 1$  periods and the range of unstable  $\ell = 1$  periods of our models, thus alleviating this discrepancy. However, a fine tuning of the surface chemical composition of our models to fit the range of observed periods is beyond the scope of this paper. This kind of "nonadiabatic asteroseismology" of GW Vir stars has been attempted by Quirion et al. (2009).

We show the main characteristics of the asteroseismological model for NGC 1501 in Table 19. The stellar mass of the seismological model ( $0.609M_{\odot}$ ) is in excellent agreement with the mass derived from the period spacing ( $\sim 0.60 - 0.62M_{\odot}$ ), assuming that the star is before the evolutionary knee. This agreement in the stellar mass is reflected in the fact that dipole and quadrupole mean period spacings of our asteroseismological model,  $\overline{\Delta\Pi}_{\ell=1} = 20.610$  s and  $\overline{\Delta\Pi}_{\ell=2} = 11.683$  s, are in excellent agreement with the  $\ell = 1$  and  $\ell = 2$  mean period spacings derived for NGC 1501 in Sect. 4.4,  $\Delta\Pi_{\ell=1} = 20.1262 \pm 0.0123$  s and  $\Delta\Pi_{\ell=2} = 11.9593 \pm 0.0520$  s, respectively. Both the stellar mass of the seismological model and the mass value derived from the period spacings are somewhat larger than the spectroscopic mass,  $0.565 \pm 0.150 M_{\odot}$  (Sect. 5). The luminosity of the asteroseismological model,  $\log(L_{\star}/L_{\odot}) = 3.85$ , is somewhat larger than that derived by Ercolano et al. (2004) [ $\log(L_{\star}/L_{\odot}) = 3.70$ ] in order to provide an ionizing spectrum that could reproduce the ionization structure implied by the observed nebular spectrum.

We derive the asteroseismological distance for NGC 1501 as we did for RX J2117 and HS 2324. We employ the luminosity of the asteroseismological model of NGC 1501,  $\log(L_{\star}/L_{\odot}) = 3.85 \pm 0.02$ , a bolometric correction of  $BC = -7.46$  (extrapolated from the value corresponding to PG 1159–035 as given by Kawaler & Bradley 1994), and the interstellar extinction law of Chen et al. (1998). For the equatorial coordinates of NGC 1501 (Epoch B2000.00,  $\alpha = 4^{\text{h}}6^{\text{m}}59^{\text{s}}.40$ ,  $\delta = +60^{\circ}55'14.''20$ ) the corresponding Galactic latitude is  $b = 6^{\circ}33'4.''06$ . If we adopt  $m_V = 13.0$  (Montreal White Dwarf Database; Dufour et al. 2017), we obtain a seismological distance, a parallax, and an

extinction coefficient of  $d = 824 \pm 15$  pc,  $\pi = 1.22^{+0.02}_{-0.03}$  mas, and  $A_V = 0.85$ , respectively. On the other hand, the values from *Gaia* are  $d_G = 1763 \pm 79$  pc and  $\pi_G = 0.567 \pm 0.025$  mas. The seismological distance is  $\sim 50\%$  shorter than that measured by *Gaia*. The origin of this discrepancy may reside in the uncertainties related to our seismological model. Again, as in the case of HS 2314, a better estimate of the uncertainties of the luminosity of the asteroseismological model probably could contribute to bringing the asteroseismological distance and parallax values closer to those derived by *Gaia*.

We bring this section to a close by summarizing our results for NGC 1501. The stellar mass inferred from the period separations ( $\sim 0.60 - 0.62M_{\odot}$ ) is in line with the mass of the seismological model ( $\sim 0.61M_{\odot}$ ). These values are somewhat larger than—but still in agreement with—the spectroscopic mass, of  $\sim 0.57M_{\odot}$ .

## 7.5. NGC 2371

In Fig. 32 we display the curves of  $\overline{\Delta\Pi}_k$  as function of  $T_{\text{eff}}$  for all the masses considered. The period spacing of NGC 2371 is  $\Delta\Pi = 14.5312 \pm 0.0226$ , as derived in the analysis of Sect. 4.5. As in the case of HS 2324, NGC 6905, and NGC 1501, for NGC 2371 we considered the possibility that the object is before or after the "evolutionary knee". We find  $M_{\star} = 0.760M_{\odot}$  if the star is before the evolutionary knee, and  $M_{\star} = 0.856M_{\odot}$  if the star is after the evolutionary knee. As in the case of NGC 6905, these values are assessed by extrapolation, because the period spacing of the star, being only about 14.5 s, is well below the average of the  $\ell = 1$  computed period-spacing curves of our models, even the most massive one. Therefore, our stellar mass values are just estimates. These estimates for the stellar mass of NGC 2371 are much larger ( $\sim 60\%$ ) than the spectroscopic mass of this star, of  $M_{\star} = 0.533 \pm 0.150 M_{\odot}$  (Sect. 5).

Below, we describe our period-to-period fit analysis for NGC 2371. Again, the merit function  $\chi^2(M_{\star}, T_{\text{eff}})$  (Eq. 3) was

**Table 18.** Observed and theoretical periods of the asteroseismological model for NGC 1501 [ $M_\star = 0.609M_\odot$ ,  $T_{\text{eff}} = 140\,051$  K,  $\log(L_\star/L_\odot) = 3.853$ ]. The columns have the same meaning as in Table 14.

$\Pi_i^O$ (s)	$\ell^O$	$\Pi_k$ (s)	$\ell$	$k$	$\delta\Pi_k$ (s)	$\dot{\Pi}_k$ ( $10^{-11}$ s/s)	Unstable
1154.360	2	1154.379	2	98	-0.019	-15.441	yes
1168.900	1	1167.137	1	57	1.713	-10.788	no
1251.910	1	1248.916	1	61	2.994	-21.429	no
1254.632	2	1257.656	2	107	-3.024	-15.823	yes
1309.086	2	1304.233	2	111	4.853	-42.157	yes
1310.696	1	1307.716	1	64	2.980	-26.766	no
1321.095	2	1315.744	2	112	5.351	-47.478	yes
1345.872	2	1350.158	2	115	-4.286	-22.660	yes
1349.460	1	1348.889	1	66	0.571	-16.437	no
1356.680	2	1362.511	2	116	-5.831	-18.491	yes
1366.279	1	1367.932	1	67	-1.653	-15.860	no
1372.940	2	1375.144	2	117	-2.204	-18.814	yes
1381.295	2	1386.419	2	118	-5.124	-22.368	yes
1392.240	1	1388.738	1	68	3.502	-14.155	no
1431.530	1	1431.050	1	70	0.480	-13.742	no
1512.660	1	1511.332	1	74	1.328	-35.180	no
1760.730	2	1759.810	2	150	0.920	-47.015	yes
1768.510	1	1772.096	1	87	-3.586	-25.077	no
1777.290	2	1771.373	2	151	5.917	-41.060	yes
1892.950	1	1895.295	1	93	-2.345	-55.804	yes
1951.490	1	1953.783	1	96	-2.293	-38.265	yes
2032.640	1	2035.792	1	100	-3.152	-40.133	yes
2077.000	1	2075.030	1	102	1.970	-64.074	yes
5234.810	1	5236.174	1	255	-1.364	-156.804	no

**Table 19.** The main characteristics of the GW Vir star NGC 1501. The second column corresponds to spectroscopic results, whereas the third column present results from the asteroseismological model of this work.

Quantity	Spectroscopy Astrometry	Asteroseismology (This work)
$T_{\text{eff}}$ [kK]	$134 \pm 10^{(a)}$	$140 \pm 6.5$
$M_\star$ [ $M_\odot$ ]	$0.565 \pm 0.150$	$0.609^{+0.055}_{-0.020}$
$\log g$ [ $\text{cm/s}^2$ ]	$6.0 \pm 0.2^{(a)}$	$5.90^{+0.14}_{-0.11}$
$\log(L_\star/L_\odot)$	$3.70^{(b)}$	$3.85 \pm 0.02$
$\log(R_\star/R_\odot)$	...	$-0.84 \pm 0.05$
$M_{\text{env}}$ [ $M_\odot$ ]	...	0.01
$(X_H, X_{\text{He}}, X_C)_s$	$0.50, 0.35, 0.15^{(a)}$	$0.50, 0.35, 0.10$
$d$ [pc]	$1762.801 \pm 78.566^{(c)}$	$824 \pm 15$
$\pi$ [mas]	$0.567 \pm 0.025^{(c)}$	$1.22^{+0.02}_{-0.03}$

References: (a) Koesterke & Hamann (1997), Werner & Herwig (2006); (b) Ercolano et al. (2004); (c) *Gaia*.

evaluated for all the stellar masses and effective temperatures covered by our PG 1159 model sequences. We employed the 10 periods of Table 13. We adopted the same approach as for the case of the previous target stars, that is, we assumed that there is a subset of 8 periods identified as  $\ell = 1$  according to the period spacing derived in Sect. 4.5 (see Table 13), but the remaining 2 periods are allowed to be identified with modes with  $\ell = 1$  or  $\ell = 2$  modes.

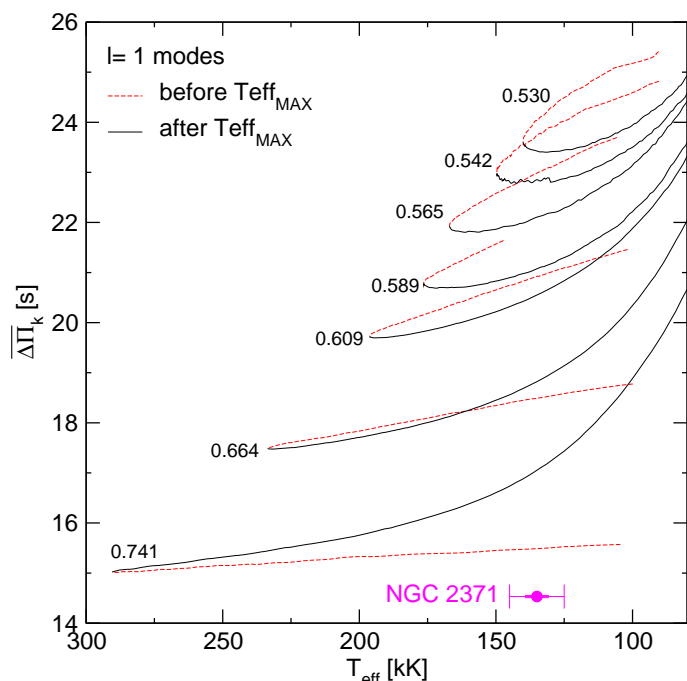
As in the previous cases, given the absence of a single global minimum in the quality function, we focused on the range of effective temperatures compatible with NGC 2371, that is  $125\,000 \lesssim T_{\text{eff}} \lesssim 135\,000$  K. We display in Fig. 33 our results. We note the existence of a clear minimum for a model with

$M_\star = 0.664M_\odot$  and  $T_{\text{eff}} = 140\,265$  K. It is located at the stages previous to the maximum temperature for this mass. We adopt this model as the asteroseismological model for NGC 2371. In Table 20 we show a detailed comparison of the observed periods of NGC 2371 and the theoretical periods of the asteroseismological model. For this asteroseismological solution, we have  $\overline{\delta\Pi_i} = 2.79$  s and  $\sigma = 3.15$  s. The quality of our fit for NGC 2371 is poorer than that achieved for RX J2117 ( $\overline{\delta\Pi_i} = 1.26$  s and  $\sigma = 1.73$  s), although comparable to those of HS 2324 ( $\overline{\delta\Pi_i} = 2.53$  s and  $\sigma = 3.36$  s) and NGC 1501 ( $\overline{\delta\Pi_i} = 2.81$  s and  $\sigma = 3.28$  s). We also computed the Bayes Information Criterion. In this case,  $N_p = 2$  (stellar mass and effective temperature),  $n = 10$ , and  $\sigma = 3.15$  s. We obtain  $\text{BIC} = 1.20$ , which means that our fit is not so good as for RX J2117 ( $\text{BIC} = 0.59$ ), although comparable with those of HS 2324 ( $\text{BIC} = 1.18$ ) and NGC 1501 ( $\text{BIC} = 1.15$ ).

Most of the rates of period change for NGC 2371 (column 7 of Table 20) are negative, in concordance with the fact that the asteroseismological model for this star is evolving towards higher effective temperatures and contracting. The magnitudes of  $\dot{\Pi}$  are comparable, in average, to those of HS 2324 and NGC 1501. Regarding the pulsational stability/instability nature of the modes with periods that fit the periods observed in NGC 2371 (column 9 of Table 20), the nonadiabatic calculations predict that all the periods (dipole and quadrupole) are stable, because at  $T_{\text{eff}} = 138\,600$  K, the model sequence of  $M_\star = 0.664M_\odot$  has unstable  $\ell = 1$  ( $\ell = 2$ ) periods in the range  $1962$  s –  $4480$  s ( $1190$  s –  $3045$  s) (Córscico et al. 2006). Then, our nonadiabatic pulsation results are in conflict with the observational evidence, similar to the case of NGC 1501. Again, we mention that the intervals of unstable periods are highly de-

**Table 20.** Observed and theoretical periods of the asteroseismological model for NGC 2371 [ $M_\star = 0.664M_\odot$ ,  $T_{\text{eff}} = 140\,265$  K,  $\log(L_\star/L_\odot) = 4.066$ ]. The columns have the same meaning as in Table 14.

$\Pi_i^O$ (s)	$\ell^O$	$\Pi_k$ (s)	$\ell$	$k$	$\delta\Pi_k$ (s)	$\dot{\Pi}_k$ ( $10^{-11}$ s/s)	Unstable
878.523	1	875.320	1	49	3.203	1.981	no
895.111	1	893.367	1	50	1.744	6.166	no
925.465	1	929.693	1	52	-4.228	-5.008	no
968.474	1	964.815	1	54	3.659	-47.723	no
982.800	1	980.871	1	55	1.929	-52.214	no
988.200	?	986.704	2	96	1.496	-1.264	no
998.000	1	997.767	1	56	0.233	-52.153	no
1005.600	?	1007.777	2	98	-2.177	-10.730	no
1010.000	1	1015.513	1	57	-5.513	-19.545	no
1825.000	1	1828.713	1	103	-3.713	-37.306	no


**Fig. 32.** Dipole ( $\ell = 1$ ) average of the computed period spacings,  $\overline{\Delta\Pi_k}$ , assessed in a range of periods that includes the periods observed in NGC 2371, shown as solid (dashed) curves corresponding to stages before (after) the maximum  $T_{\text{eff}}$  for different stellar masses. The location of NGC 2371 when we use the effective temperature derived by Ciardullo & Bond (1996),  $T_{\text{eff}} = 135\,000 \pm 10\,000$  K, and the period spacing  $\Delta\Pi = 14.5312 \pm 0.0226$  s derived in Sect. 3.5, is highlighted with a magenta circle. The stellar mass derived from linear extrapolation is  $M_\star \sim 0.760M_\odot$  if the star is before the maximum  $T_{\text{eff}}$ , and it is  $M_\star \sim 0.856M_\odot$  if the star is after the maximum  $T_{\text{eff}}$ .

pendent on the chemical composition of the outer part of the PG 1159 stars, which is affected by uncertainties in the treatment of convective boundary mixing during the born again episode.

In Table 21, we list the main characteristics of the asteroseismological model for NGC 2371. The luminosity and radius of the asteroseismological model ( $\log(L_\star/L_\odot) = 4.07$ ,  $\log(R_\star/R_\odot) = -0.74$ ) are substantially larger than the values derived by Gómez-González et al. (2020) ( $\log(L_\star/L_\odot) = 3.45$ ,  $\log(R_\star/R_\odot) = -0.98$ ) from stellar atmosphere models. The stellar mass of the seismological model ( $0.664M_\odot$ ) is  $\sim 14\%$  lower than the mass inferred from the period spacing ( $\sim 0.76M_\odot$ ), assuming that the star is before the evolutionary knee. This mass

**Table 21.** The main characteristics of the GW Vir star NGC 2371. The second column corresponds to spectroscopic results, whereas the third column present results from the asteroseismological model of this work.

Quantity	Spectroscopy Astrometry	Asteroseismology (This work)
$T_{\text{eff}}$ [kK]	$135 \pm 10^{(a)}$	$140.3^{+10.6}_{-5.3}$
$M_\star$ [ $M_\odot$ ]	$0.533 \pm 0.150$	$0.664^{+0.077}_{-0.055}$
$\log g$ [ $\text{cm/s}^2$ ]	$6.3 \pm 0.2^{(a)}$	$5.74^{+0.19}_{-0.12}$
$\log(L_\star/L_\odot)$	$3.45^{(b)}$	$4.07^{+0.01}_{-0.02}$
$\log(R_\star/R_\odot)$	$-0.98^{(b)}$	$-0.74^{+0.04}_{-0.07}$
$M_{\text{env}}$ [ $M_\odot$ ]	...	0.02
$(X_{\text{He}}, X_{\text{C}}, X_{\text{O}})_s$	$0.54, 0.37, 0.08^{(a)}$	$0.47, 0.33, 0.13$
$d$ [pc]	$1879.138 \pm 232.467^{(c)}$	$1816^{+11}_{-51}$
$\pi$ [mas]	$0.532 \pm 0.066^{(c)}$	$0.554^{+0.013}_{-0.007}$

References: (a) Herald & Bianchi (2004); (b) Gómez-González et al. (2020); (c) *Gaia*.

discrepancy is reflected in the fact that dipole ( $\ell = 1$ ) mean period spacing of our asteroseismological model ( $\overline{\Delta\Pi} = 18.45$  s) is markedly longer than the  $\ell = 1$  mean period spacing for NGC 2371 derived in Sect. 4.5 ( $\Delta\Pi = 14.5312 \pm 0.0226$  s). Both the stellar mass of the seismological model and the value derived from the period spacing are in disagreement with the spectroscopic mass,  $0.533 \pm 0.150 M_\odot$  (Sect. 5). This discrepancy between the spectroscopic mass (based on measured  $T_{\text{eff}}$  and  $\log g$  values) and seismological masses (based on period spacing and individual periods compared to theoretical expectations) is similar to that found for HS 2324.

We employ the luminosity of the asteroseismological model of NGC 2371,  $\log(L_\star/L_\odot) = 4.066^{+0.01}_{-0.02}$ , a bolometric correction of  $BC = -7.24$  (the same value used for the assessment of the distance to HS 2314) and the interstellar extinction law of Chen et al. (1998), to estimate the asteroseismological distance. For the equatorial coordinates of NGC 2371 (Epoch B2000.00,  $\alpha = 7^{\text{h}}25^{\text{m}}34.^{\text{s}}69$ ,  $\delta = +29^\circ29'26.''32$ ) the corresponding Galactic latitude is  $b = 19^\circ50'35.''52$ . By adopting an apparent magnitude of  $m_V = 13.50$  (Montreal White Dwarf Database; Dufour et al. 2017), we derive  $d = 1816^{+11}_{-51}$  pc,  $\pi = 0.554^{+0.013}_{-0.007}$  mas, and  $A_V = 0.402$ . On the other hand, the values from *Gaia* are  $d_G = 1879 \pm 232$  pc and  $\pi_G = 0.532 \pm 0.066$  mas. There is a good agreement between the seismological distance and parallax and their counterparts measured by *Gaia*, given the uncertainties in both sets of magnitudes.

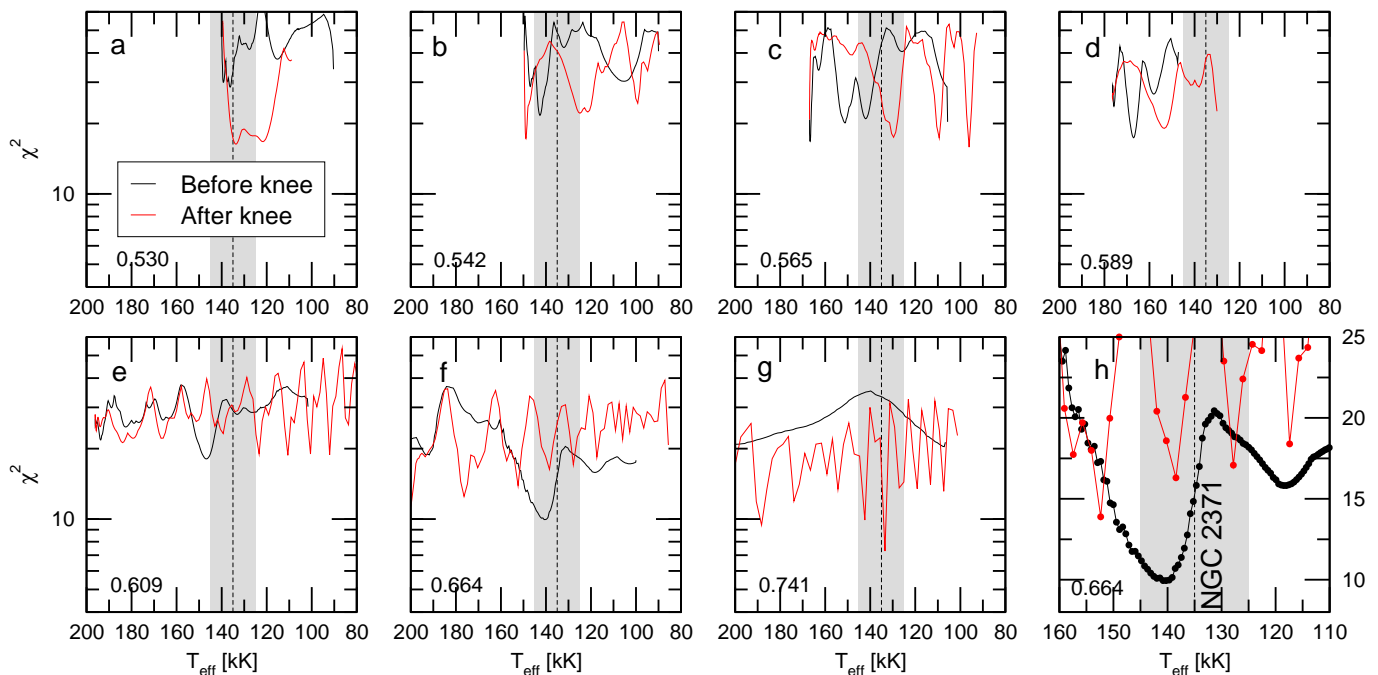


**Fig. 33.** Same as Fig. 26, but for NGC 2371. Note the minimum in panel **f** before the evolutionary knee (black curve), corresponding to  $M_{\star} = 0.664M_{\odot}$ . Panel **h** is a zoom of the region with the strong minimum seen in panel **f**; the y-axis scale is linear in this case. The vertical dashed line is the spectroscopic  $T_{\text{eff}}$  of NGC 2371 (135 kK) and the gray zone depicts its uncertainties ( $\pm 10$  kK).

We end this section with a summary of our results for NGC 2371. The stellar mass inferred from the period separation is larger than the mass of the seismological model, but they are still in agreement. However, these values are at variance with the spectroscopic mass, which is markedly lower. The seismological distance, on the other hand, is in good concordance with that measured by *Gaia*. This suggests that the parameters of the seismological model are correct, and that the discrepancy in mass between the seismological inference and the spectroscopic derivation can come from very uncertain values in the spectroscopic  $T_{\text{eff}}$  and  $\log g$ .

## 8. Summary and conclusions

In this work, we have performed a detailed asteroseismological analysis of the formerly known GW Vir stars RX J2117, HS 2324, NGC 6905, NGC 1501, NGC 2371, and K 1–16 on the basis of the new *TESS* observations of these stars. *TESS* primary mission is to search for exoplanets around bright targets, although the high-precision photometry capabilities of the mission are also allowing us to study low-amplitude stellar variability, including WD pulsations (Bell et al. 2019; Bognár et al. 2020). We studied the pulsation spectrum of these stars, and, in one case (RX J2117), we estimated the rotation period on the basis of frequency-splitting multiplets. We also determined their stellar mass and other structural and evolutionary properties on the basis of the detailed PG 1159 evolutionary models of Althaus et al. (2005) and Miller Bertolami & Althaus (2006). We have considered adiabatic and nonadiabatic  $g$ -mode pulsation periods on PG 1159 evolutionary models with stellar masses ranging from 0.530 to 0.741  $M_{\odot}$ . These models take into account the complete evolution of progenitor stars through the thermally pulsing AGB phase and born-again episode.

We estimated a mean period spacing for five of the six studied stars. To do this, we considered an augmented period spectrum for each star, combining the periods detected in previous

works with ground-based observations with the more precise periods detected with *TESS*. In this way, we expanded, when possible, the number of observed periods, allowing us to arrive at a regime where asteroseismological methods start to be robust. The benefit of the derivation of an underlying period spacing in the observed period spectrum of GW Vir stars is twofold. On the one hand, it allows to put strong constraints on the stellar mass. On the other hand, it allows assigning the harmonic degree  $\ell$  to a large number of observed periods, which simplifies and constrains the subsequent process of fitting the individual periods and the derivation of asteroseismological models. For five of the objects studied, we constrained the stellar mass by comparing the observed period spacing with the average of the computed period spacings. We considered the cases where the star is before or after the maximum possible effective temperature, although the  $\log g$  and  $T_{\text{eff}}$  spectroscopic values — and their comparison with evolutionary tracks of PG 1159 stars — strongly suggests that all the target stars are evolving before the evolutionary knee in the  $T_{\text{eff}} - \log g$  diagram (Fig. 1). When possible, we also employed the individual observed periods to search for a representative seismological model for each star. Finally, we derived seismological distances whenever this was possible, and compared these estimates with the robust astrometric distances measured by *Gaia*.

We present the main results for each analyzed star below:

- RX J2117: The number of secure periods found with the *TESS* observations for this star is 15 (see Table 3). From two complete rotational triplets and three triplets with one lacking component in the *TESS* frequency spectrum of this star, we derived a rotation period of  $P_{\text{rot}} \sim 1.04$  days, in agreement with previous works (Vauclair et al. 2002; Córscico et al. 2007a). On the basis of a subset of 20 periods of the extended period spectrum (ground-based plus *TESS* observations; Table 9), we inferred a  $\ell = 1$  constant period spacing of  $\Delta\Pi = 21.669 \pm 0.030$  s. This allowed a safe iden-



tification of 27 periods as dipole modes, with the remainder 4 periods without a secure assignation of the value of  $\ell$ . The comparison of this period spacing with the average of the theoretical period spacings allowed us to derive a stellar mass of  $M_\star = 0.569 \pm 0.015 M_\odot$ , in perfect agreement with the estimates from Vauclair et al. (2002) ( $M_\star = 0.56 M_\odot$ ), and Córscico et al. (2007a) ( $M_\star = 0.560 M_\odot$ ) also using the period spacing to derive the stellar mass. We next derived an asteroseismological model for this star by means of a period-to-period fit procedure. The magnitude of the rates of period change for the asteroseismological model ranges from  $\sim 2.5 \times 10^{-11}$  to  $\sim 14.1 \times 10^{-11}$  s/s and all the values are negative, in concordance with the fact that the model is fast evolving towards high effective temperatures ( $T_{\text{eff}} > 0$ ) and contracting ( $\dot{R}_\star < 0$ ), a little before reaching the maximum possible temperature. Most of the  $g$  modes of the asteroseismological model are predicted to be linearly unstable, in concordance with the observations. Two of the periods that could not be identified with  $\ell = 1$  modes using the constant period spacing are identified with  $\ell = 2$  modes and the remaining two periods with  $\ell = 1$  modes, according to the asteroseismological model (Table 14). The stellar mass of the asteroseismological model ( $M_\star = 0.565 \pm 0.024 M_\odot$ ) is in excellent agreement with the mass derived from the period spacing. Finally, we derived a seismological distance ( $d = 480$  pc) in complete consensus with the *Gaia* distance ( $d_G = 502$  pc), giving robustness to the asteroseismological model. On the other hand, the asteroseismological masses apparently disagree with the spectroscopic mass ( $M_\star = 0.716 M_\odot$ ), but, given the large uncertainties of this last estimate, we conclude that the asteroseismological and spectroscopic determinations agree with each other.

- HS 2324: We detected 12 periods from the *TESS* data for this star (Table 4). At variance with Silvotti et al. (1999), we found no rotational multiplets with a much better frequency resolution of  $0.35 \mu\text{Hz}$ . This prevented us from deriving a rotational period. Using a subset of 9 periods of the augmented period spectrum (ground based and *TESS* data; see Table 10), we inferred the existence of a  $\ell = 1$  constant period spacing of  $\Delta\Pi = 16.407 \pm 0.062$  s, which enabled a robust identification of 13 periods as  $\ell = 1$  modes. The periods from ground-based observations we used in this paper are slightly different from those in Table 2 of Silvotti et al. (1999). By comparing the derived dipole period spacing with the average of the theoretical period spacings, we estimated a stellar mass of  $M_\star = 0.727 \pm 0.017 M_\odot$  if the star is before the evolutionary knee. We obtained an asteroseismological model for HS 2324 by comparing the individual observed and theoretical periods. Most of the rates of period change for the asteroseismological model are negative, and their magnitudes are in the interval  $(\sim 8.5 - 138.0) \times 10^{-11}$  s/s, which implies that this star must be evolving much faster than RX J2117. Our stability analysis predicts most of the modes of the asteroseismological model to be unstable, in line with observations. Most of the observed periods that could not be identified with  $\ell = 1$  modes on the basis of the constant period spacing are identified with modes  $\ell = 2$  according to the asteroseismological model (Table 16). The stellar mass of the asteroseismological model,  $M_\star = 0.664^{+0.077}_{-0.055} M_\odot$ , is  $\sim 10\%$  lower than the mass estimated from the period spacing, but still compatible with it. Finally, the seismological distance ( $d = 4379 \pm 1000$  pc)

is 3 times larger than the *Gaia* distance ( $d_G = 1448$  pc), but if we could take into account realistic uncertainties that affect seismological distance, probably the disagreement would not be so great. The asteroseismological masses, on the other hand, are higher than the spectroscopic mass ( $M_\star = 0.532 M_\odot$ ). However, because the large uncertainties in the spectroscopic mass, both spectroscopic and asteroseismological determinations are compatible each other. Additional future observations of HS 2324 will be of great importance in detecting new periods and investigating possible signals of stellar rotation through frequency multiples.

- NGC 6905: *TESS* photometry indicates the presence of only 4 periods in the pulsation spectrum of this star, as shown in Table 5. We employed a subset of 7 periods of the enlarged list of periods (see Table 11), to uncover the existence of a constant period spacing of  $\Delta\Pi = 11.9693 \pm 0.0988$  s, which we can attribute, in principle, to  $\ell = 1$  modes. This period spacing enabled us to do a secure identification of 7 periods as dipole modes. By comparing the inferred  $\ell = 1$  period spacing with the average of the theoretical period spacings we obtained a stellar mass estimate of  $M_\star \sim 0.818 M_\odot$  if the star is before the maximum  $T_{\text{eff}}$ . This estimate of the stellar mass is in strong disagreement with the spectroscopic mass of this star, of  $M_\star = 0.590 M_\odot$ . We also explored the possible situation in which the period spacing of  $\Delta\Pi = 11.9693 \pm 0.0988$  s correspond to  $\ell = 2$  modes. In this case, the mass of the star should be  $M_\star = 0.596 \pm 0.009 M_\odot$  and  $M_\star = 0.590 \pm 0.007 M_\odot$  if the star is before or after the evolutionary knee, respectively, in very good agreement with the spectroscopic mass value. Both in the cases where the period spacing corresponds to  $\ell = 1$  or corresponds to  $\ell = 2$  instead, the results of our period-to-period fit procedure did not indicate a clear and unique asteroseismological solution. Thus, for NGC 6905, we are unable to find an asteroseismological model, which deprives us of the possibility of estimating the seismic distance for this star.
- NGC 1501: We measured 16 periods for this star on the basis of *TESS* observations (Table 6). We considered a subset of 23 periods of the enlarged list of periods (i.e., from ground-based plus *TESS* observations; see Table 12), and we found a  $\ell = 1$  constant period spacing of  $\Delta\Pi = 20.1262 \pm 0.0123$  s and a  $\ell = 2$  constant period spacing of  $\Delta\Pi = 11.9593 \pm 0.0520$  s. This enabled us to identify 14 periods as  $\ell = 1$  modes and 10 periods as  $\ell = 2$  modes, with the remainder 2 periods without a secure assignation of the  $\ell$  value. The comparison of these observed period spacings with the average of the theoretical period spacings for  $\ell = 1$  and  $\ell = 2$  allowed us to infer a stellar mass of  $M_\star = 0.621 \pm 0.015 M_\odot$  and  $M_\star = 0.601 \pm 0.015 M_\odot$ , respectively, if the star is before the maximum  $T_{\text{eff}}$ . These values are in close agreement each other. We derived an asteroseismological model for this star on the basis of our usual period-to-period fit procedure (Table 14). The magnitude of the rates of period change for the asteroseismological model ranges from  $\sim 10 \times 10^{-11}$  to  $\sim 160 \times 10^{-11}$  s/s and all the values are negative, as expected on the grounds that the model is heating up and quickly contracting. Noticeably, all the  $\ell = 2$  modes are predicted to be unstable by our nonadiabatic calculations, while most  $\ell = 1$  modes are predicted to be stable. The stellar mass of the asteroseismological model ( $M_\star = 0.609^{+0.06}_{-0.02} M_\odot$ ) is in perfect concordance with the mass inferred from the period

separations, and in agreement with the spectroscopic mass, given its uncertainty. Finally, we derived a seismological distance ( $d = 824$  pc) which is  $\sim 50\%$  shorter than the *Gaia* distance ( $d_G = 1763$  pc). The agreement between these sets of values could improve if we could employ more realistic values for the uncertainties in the luminosity of the asteroseismological model.

- NGC 2371: We detected 5 periods from the *TESS* data for this star (Table 7). Considering a subset of 8 periods of the enlarged period set (i.e., those from ground-based observations along with *TESS* data; see Table 13), we found a  $\ell = 1$  constant period spacing of  $\Delta\Pi = 14.5312 \pm 0.0226$  s, allowing us to safely identify 8 periods with  $\ell = 1$  modes, leaving unidentified the remaining 2 periods. The comparison of the derived dipole period spacing with the average of the model period spacings results in an estimate of the stellar mass of  $M_\star \sim 0.760M_\odot$  if the star is before the evolutionary knee. We obtained an asteroseismological model for NGC 2371 from a period-to-period fit, with most of the rates of period change being negative, and with magnitudes in the range  $(\sim 2 - 52) \times 10^{-11}$  s/s. Our stability analysis predicts *all* of the modes of the asteroseismological model to be stable, in conflict with observations. The two observed periods that could not be identified with  $\ell = 1$  modes on the basis of the constant period spacing are identified with  $\ell = 2$  modes according to the asteroseismological model (Table 20). The stellar mass of the asteroseismological model,  $M_\star = 0.664^{+0.077}_{-0.055}M_\odot$ , is  $\sim 14\%$  smaller than the mass inferred from the period spacing, assuming that the star is before the evolutionary knee. The asteroseismological distance is  $d = 1816$  pc, in very good agreement with the distance measured with *Gaia*, of  $d_G = 1880 \pm 232$  pc. This agreement reinforces the validity of the asteroseismological model. Both the stellar mass of the seismological model and the mass value derived from the period spacing are in disagreement with the spectroscopic mass, of  $M_\star = 0.533 \pm 0.150M_\odot$ . This mass discrepancy is probably due to the large uncertainty in the spectroscopic  $\log g$  value. We conclude that, in a similar way than for RX J2117 and HS 2324, these spectroscopic parameters need to be redetermined for NGC 2371.
- K 1–16: For this star, we have been able to detect only 5 (or 6) periods (Table 8). The amplitudes and frequencies change significantly in such a way that if we look individually the sectors of *TESS*, some modes have zero amplitudes, but they have finite amplitudes in other sectors. Due to the complexity and changing nature of the period spectrum of this star, along with the high noise level of its power spectrum, we were forced to crudely estimating the period values, and then added a single period detected from the ground. Considering a composite list of periods, we only have 6 periods available, for which we found no evidence of any pattern of constant period spacing. Due to all these reasons, our asteroseismological analysis was limited, but it revealed the dramatic changes that the pulsations experience in this star, as depicted in Fig. 7.

The results of this paper demonstrate that the high-quality observations of *TESS*, considered in conjunction with ground-based observations (which are usually more uncertain), are able to provide a very important input to the asteroseismology of GW Vir stars, in line with recent reports for other classes of pulsat-

ing WDs, such as the case of a DBV star (Bell et al. 2019), pre-ELMV stars (Wang et al. 2020), warm DA WDs (Althaus et al. 2020), and DAV stars (Bognár et al. 2020).

The *TESS* space mission is demonstrating that it can greatly contribute to the asteroseismology of WDs and pre-WDs, becoming a worthy successor of the *Kepler* mission, which has had an excellent performance at studying pulsating WDs (Córscico 2020). The *TESS* mission, in conjunction with other ongoing space missions such as *Cheops* (Moya et al. 2018) and future space missions like *PLATO* (Piotto 2018), along with new surveys and telescopes such as the Legacy Survey for Space and Time (LSST Science Collaboration et al. 2009), which will be operational in the coming years (Fantin et al. 2020), will probably make stunning progress in WD asteroseismology.

*Acknowledgements.* We wish to acknowledge the suggestions and comments of an anonymous referee that strongly improved the original version of this work. This paper includes data collected with the *TESS* mission, obtained from the MAST data archive at the Space Telescope Science Institute (STScI). Funding for the *TESS* mission is provided by the NASA Explorer Program. STScI is operated by the Association of Universities for Research in Astronomy, Inc., under NASA contract NAS 5–26555. Part of this work was supported by AGENCIA through the Programa de Modernización Tecnológica BID 1728/OC-AR, and by the PIP 112-200801-00940 grant from CONICET. M.U. acknowledges financial support from CONICYT Doctorado Nacional in the form of grant number No: 21190886. SOK is supported by CNPq-Brazil, CAPES-Brazil and FAPERGS-Brazil. KJB is supported by the National Science Foundation under Award No. AST-1903828. This research has made use of NASA’s Astrophysics Data System. Financial support from the National Science Centre under projects No. UMO-2017/26/E/ST9/00703 and UMO-2017/25/B/ST9/02218 is appreciated.

## References

- Althaus, L. G., Córscico, A. H., Isern, J., & García-Berro, E. 2010, *A&A Rev.*, 18, 471
- Althaus, L. G., Córscico, A. H., Kepler, S. O., & Miller Bertolami, M. M. 2008, *A&A*, 478, 175
- Althaus, L. G., Córscico, A. H., Uzundag, M., et al. 2020, *A&A*, 633, A20
- Althaus, L. G., Serenelli, A. M., Panei, J. A., et al. 2005, *A&A*, 435, 631
- Appleton, P. N., Kawaler, S. D., & Eitter, J. J. 1993, *AJ*, 106, 1973
- Baran, A. S., Telting, J. H., Németh, P., Bachulski, S., & Krzesiński, J. 2015, *A&A*, 573, A52
- Bell, K. J. 2017, PhD thesis, University of Texas
- Bell, K. J., Córscico, A. H., Bischoff-Kim, A., et al. 2019, *A&A*, 632, A42
- Bell, K. J., Hermes, J. J., Vanderbosch, Z., et al. 2017, *ApJ*, 851, 24
- Blöcker, T. 2001, *Ap&SS*, 275, 1
- Bognár, Z., Kawaler, S. D., Bell, K. J., et al. 2020, *A&A*, 638, A82
- Bognár, Z. & Sodor, A. 2016, *Information Bulletin on Variable Stars*, 6184
- Bond, H. E., Kawaler, S. D., Ciardullo, R., et al. 1996, *AJ*, 112, 2699
- Borucki, W. J., Koch, D., Basri, G., et al. 2010, *Science*, 327, 977
- Bradley, P. A., Winget, D. E., & Wood, M. A. 1993, *ApJ*, 406, 661
- Brassard, P., Fontaine, G., Wesemael, F., & Hansen, C. J. 1992, *ApJS*, 80, 369
- Calcaferro, L. M., Córscico, A. H., & Althaus, L. G. 2016, *A&A*, 589, A40
- Chang, H. K., Shih, I. C., Liu, C. Y., et al. 2013, *A&A*, 558, A63
- Chen, B., Vergely, J. L., Valette, B., & Carraro, G. 1998, *A&A*, 336, 137
- Ciardullo, R. & Bond, H. E. 1996, *AJ*, 111, 2332
- Córscico, A. H. 2020, *Frontiers in Astronomy and Space Sciences*, 7, 47
- Córscico, A. H. & Althaus, L. G. 2005, *A&A*, 439, L31
- . 2006, *A&A*, 454, 863
- Córscico, A. H., Althaus, L. G., Benvenuto, O. G., & Serenelli, A. M. 2002, *A&A*, 387, 531
- Córscico, A. H., Althaus, L. G., Kepler, S. O., Costa, J. E. S., & Miller Bertolami, M. M. 2008, *A&A*, 478, 869
- Córscico, A. H., Althaus, L. G., & Miller Bertolami, M. M. 2006, *A&A*, 458, 259
- Córscico, A. H., Althaus, L. G., Miller Bertolami, M. M., & García-Berro, E. 2009a, *A&A*, 499, 257
- Córscico, A. H., Althaus, L. G., Miller Bertolami, M. M., González Pérez, J. M., & Kepler, S. O. 2009b, *ApJ*, 701, 1008
- Córscico, A. H., Althaus, L. G., Miller Bertolami, M. M., & Kepler, S. O. 2019, *A&A Rev.*, 27, 7
- Córscico, A. H., Althaus, L. G., Miller Bertolami, M. M., & Werner, K. 2007a, *A&A*, 461, 1095

- Córscico, A. H., Miller Bertolami, M. M., Althaus, L. G., Vauclair, G., & Werner, K. 2007b, *A&A*, 475, 619
- Costa, J. E. S., Kepler, S. O., Winget, D. E., et al. 2008, *A&A*, 477, 627
- Cox, A. N. 2000, *Allen's astrophysical quantities*
- Dreizler, S., Werner, K., Heber, U., & Engels, D. 1996, *A&A*, 309, 820
- Dufour, P., Blouin, S., Coutu, S., et al. 2017, in *Astronomical Society of the Pacific Conference Series*, Vol. 509, 20th European White Dwarf Workshop, ed. P. E. Tremblay, B. Gaensicke, & T. Marsh, 3
- Dziembowski, W. 1977, *Acta Astron.*, 27, 203
- Eastman, J., Siverd, R., & Gaudi, B. S. 2010, *PASP*, 122, 935
- Ercolano, B., Wesson, R., Zhang, Y., et al. 2004, *MNRAS*, 354, 558
- Faedi, F., West, R. G., Burleigh, M. R., Goad, M. R., & Hebb, L. 2011, *MNRAS*, 410, 899
- Fantini, N. J., Côté, P., & McConnachie, A. W. 2020, *ApJ*, 900, 139
- Feibelman, W. A., Kaler, J. B., Bond, H. E., & Grauer, A. D. 1995, *PASP*, 107, 914
- Fontaine, G. & Brassard, P. 2008, *PASP*, 120, 1043
- Gautschi, A., Althaus, L. G., & Saio, H. 2005, *A&A*, 438, 1013
- Gómez-González, V. M. A., Toalá, J. A., Guerrero, M. A., et al. 2020, *MNRAS*, 496, 959
- Grauer, A. D. & Bond, H. E. 1984, *ApJ*, 277, 211
- Handler, G., Kanaan, A., & Montgomery, M. H. 1997a, *A&A*, 326, 692
- Handler, G., Pikall, H., O'Donoghue, D., et al. 1997b, *MNRAS*, 286, 303
- Herald, J. E. & Bianchi, L. 2004, *ApJ*, 609, 378
- Hermes, J. J., Gänsicke, B. T., Kawaler, S. D., et al. 2017a, *ApJS*, 232, 23
- Hermes, J. J., Kawaler, S. D., Bischoff-Kim, A., et al. 2017b, *ApJ*, 835, 277
- Herwig, F. 2001, *ApJ*, 554, L71
- Howell, S. B., Sobeck, C., Haas, M., et al. 2014, *PASP*, 126, 398
- Jenkins, J. M., Twicken, J. D., McCauliff, S., et al. 2016, in *Proc. SPIE*, Vol. 9913, *Software and Cyberinfrastructure for Astronomy IV*, 99133E
- Kawaler, S. D. 1988, in *IAU Symposium*, Vol. 123, *Advances in Helio- and Asteroseismology*, ed. J. Christensen-Dalsgaard & S. Frandsen, 329
- Kawaler, S. D. & Bradley, P. A. 1994, *ApJ*, 427, 415
- Kepler, S. O. 1993, *Baltic Astronomy*, 2, 515
- Kepler, S. O., Fraga, L., Winget, D. E., et al. 2014, *MNRAS*, 442, 2278
- Koen, C. & Laney, D. 2000, *MNRAS*, 311, 636
- Koesterke, L. 2001, *Ap&SS*, 275, 41
- Koesterke, L. & Hamann, W. R. 1997, in *IAU Symposium*, Vol. 180, *Planetary Nebulae*, ed. H. J. Habing & H. J. G. L. M. Lamers, 114
- Ledoux, P. & Walraven, T. 1958, *Handbuch der Physik*, 51, 353
- Löbbling, L., Rauch, T., Miller Bertolami, M. M., et al. 2019, *MNRAS*, 489, 1054
- LSST Science Collaboration, Abell, P. A., Allison, J., et al. 2009, *arXiv e-prints*, arXiv:0912.0201
- Miller Bertolami, M. M. & Althaus, L. G. 2006, *A&A*, 454, 845
- . 2007a, *A&A*, 470, 675
- . 2007b, *MNRAS*, 380, 763
- Miller Bertolami, M. M., Althaus, L. G., Serenelli, A. M., & Panei, J. A. 2006, *A&A*, 449, 313
- Motch, C., Werner, K., & Pakull, M. W. 1993, *A&A*, 268, 561
- Moya, A., Barceló Forzeza, S., Bonfanti, A., et al. 2018, *A&A*, 620, A203
- Murphy, S. J. 2015, *MNRAS*, 453, 2569
- Napiwotzki, R. & Schoenberner, D. 1991, *A&A*, 249, L16
- Nather, R. E., Winget, D. E., Clemens, J. C., Hansen, C. J., & Hine, B. P. 1990, *ApJ*, 361, 309
- O'Donoghue, D. 1994, *MNRAS*, 270, 222
- Østensen, R. H., Bloemen, S., Vučković, M., et al. 2011, *ApJ*, 736, L39
- Piotto, G. 2018, in *European Planetary Science Congress*, EPSC2018-969
- Provencal, J. L., Montgomery, M. H., Kanaan, A., et al. 2009, *ApJ*, 693, 564
- Quirion, P. O., Fontaine, G., & Brassard, P. 2007, *ApJS*, 171, 219
- Quirion, P. O., Fontaine, G., & Brassard, P. 2009, in *Journal of Physics Conference Series*, Vol. 172, *Journal of Physics Conference Series*, 012077
- Rauch, T. & Werner, K. 1997, in *The Third Conference on Faint Blue Stars*, ed. A. G. D. Philip, J. Liebert, R. Saffer, & D. S. Hayes, 217
- Ricker, G. R., Winn, J. N., Vanderspek, R., et al. 2015, *Journal of Astronomical Telescopes, Instruments, and Systems*, 1, 014003
- Ricker, G. R., Winn, J. N., Vanderspek, R., et al. 2014, in *Proc. SPIE*, Vol. 9143, *Space Telescopes and Instrumentation 2014: Optical, Infrared, and Millimeter Wave*, 914320
- Silvotti, R. 1996, *A&A*, 309, L23
- Silvotti, R., Dreizler, S., Handler, G., & Jiang, X. J. 1999, *A&A*, 342, 745
- Stanghellini, L., Cox, A. N., & Starrfield, S. 1991, *ApJ*, 383, 766
- Starrfield, S., Cox, A. N., Kidman, R. B., & Pesnell, W. D. 1984, *ApJ*, 281, 800
- Starrfield, S. G., Cox, A. N., Hodson, S. W., & Pesnell, W. D. 1983, *ApJ*, 268, L27
- Tassoul, M., Fontaine, G., & Winget, D. E. 1990, *ApJs*, 72, 335
- Vauclair, G., Belmonte, J. A., Pfeiffer, B., et al. 1993, *A&A*, 267, L35
- Vauclair, G., Moskalik, P., Pfeiffer, B., et al. 2002, *A&A*, 381, 122
- Wang, K., Zhang, X., & Dai, M. 2020, *ApJ*, 888, 49
- Watson, T. K. & Werner, K. 1992, *IAU Circ.*, 5603, 1
- Werner, K., Deetjen, J. L., Dreizler, S., et al. 2003, in *Astronomical Society of the Pacific Conference Series*, Vol. 288, *Stellar Atmosphere Modeling*, ed. I. Hubeny, D. Mihalas, & K. Werner, 31
- Werner, K. & Herwig, F. 2006, *PASP*, 118, 183
- Werner, K., Rauch, T., & Kruk, J. W. 2007, *A&A*, 474, 591
- . 2010, *ApJ*, 719, L32
- Winget, D. E., Hansen, C. J., & van Horn, H. M. 1983, *Nature*, 303, 781
- Winget, D. E. & Kepler, S. O. 2008, *ARA&A*, 46, 157
- Winget, D. E., Nather, R. E., Clemens, J. C., et al. 1991, *ApJ*, 378, 326
- Wood, P. R. & Faulkner, D. J. 1986, *ApJ*, 307, 659
- York, D. G., Adelman, J., Anderson, Jr., J. E., et al. 2000, *AJ*, 120, 1579
- Zong, W., Charpinet, S., Fu, J.-N., et al. 2018, *ApJ*, 853, 98